

A THEORETICAL STUDY ON ESR DATING OF GEOLOGICAL FAULTS
IN SOUTHERN CALIFORNIA

A THEORETICAL STUDY ON ESR DATING OF GEOLOGICAL FAULTS
IN SOUTHERN CALIFORNIA

by

WILLIAM M. BUHAY, B.Sc.

A Thesis

Submitted to the School of Graduate Studies

in Partial Fulfillment of the Requirements

for the Degree

Master of Science

McMaster University

December 1987

MASTER OF SCIENCE (1987)
(Geology)

McMASTER UNIVERSITY
Hamilton, Ontario

TITLE: A THEORETICAL STUDY ON ESR DATING OF GEOLOGICAL FAULTS
IN SOUTHERN CALIFORNIA

AUTHOR: William M. Buhay, B.Sc. (McMaster University, Hamilton
Ontario)

SUPERVISOR: Professor Henry P. Schwarcz

NUMBER OF PAGES: xiv, 136

Abstract

The recent urban sprawl in the tectonically active region of California has prompted palaeoseismologists, to find ways of forecasting potentially hazardous earthquakes on existing faults. Electron spin resonance (ESR) can be used to date fault gouge from different regions in a fault zone thereby providing a history of fault movements in a particular region. Therefore, an earthquake frequency pattern can be established and the faults can be rated as to their potential danger.

ESR dating of fault gouge is based on the premise that the ESR signals of quartz grains in the gouge have been completely reset by movements on the fault. The elapsed time since faulting is recorded by a gradual charge build up in the quartz corresponding to radioactive decay of radionuclides in the fault gouge matrix. The mechanism of zeroing of the ESR signals in quartz during fault activity is not well understood. In order to better comprehend the zeroing process, the variation of ESR signals, AD and age, with respect to quartz grains size were studied. These parameters are affected by induced stress to a greater extent in the smaller grain sizes. Therefore, with sufficient stress, the smallest grain sizes (smaller than a critical size) will be totally reset and define a "plateau" of equal age. This plateau criteria is used to define total resetting in a fault gouge sample and

only these portions of the samples are used for dating. The establishment of an equal age plateau is confirmed for one of the fault samples collected from Southern California.

Acknowledgements

I would first of all like to thank Dr. Henry P. Schwarcz for supervising this research project and for providing help and encouragement throughout the course of the thesis. Henry you also enabled me to partake in an international conference, an experience that I will not soon forget, and for this I am greatly appreciative. Dr. Rainer Grün also deserves alot of thanks for providing guidance and criticism (all constructive !) and setting me back on track when I strayed from ESR reality (sorry Rainer this is all I can write; I have to go eat now). I am also greatly indebted to Dr. Paul M. Clifford who was always there for advice, not only during this thesis but throughout my undergraduate years. I would also like to thank Steve Zymela for his many suggestions concerning ESR (some I believed), and for ending the curse on my computer. Thanks must also go to Dave "Rock and Roll" and Pam "Main Sail" Collins for just being them, and Craig and Annboat Rice for just being whatever, and for making the years bearable. Thanks also to John "Jackknife" Ferguson and Paula "I only come in Tuesdays Wednesdays and Thursdays" MacKinnon, the worlds greatest office mates.

Thanks are also in order for: Tom Rockwell (SDSU), Dave Schwartz (USGS), and R. Biegel (USC) who kindly provided the samples of gouge; Ian Thompson for technical advice on ESR

spectrometry, Chris Lopresti for irradiation of the samples, Ota Mudroch for help with XRF, Jack Whorwood for his outstanding photographs, Len Zwicker for his stupendous thin sections and to all of my friends here at Mac, old and new.

I would like to thank my family, particularly my parents, my Baba and Grandmother who's guidance and support has permitted me to further my education, but more importantly has enabled me to become a better person through their example. None of this would have been possible without you. Last, but certainly not least I thank Ruth and her mother Monica, two crazy Lithuanians who I have come to know and love over the past two years.

Table of Contents

	Page
CHAPTER 1: INTRODUCTION.....	1
1.1 General Introduction.....	1
1.2 Introduction to ESR.....	4
1.3 Objective.....	5
CHAPTER 2: PRINCIPLES OF ESR DATING.....	7
2.1 Physical Principles.....	7
2.2 Determination of AD.....	9
2.3 Determination of DR.....	12
2.4 Attenuation of Radioactive Particles.....	15
CHAPTER 3: THE ESR SPECTROMETER.....	17
CHAPTER 4: ESR SPECTRA.....	22
4.1 General.....	22
4.2 ESR Centers in Quartz.....	25
4.2.1 Impurity Defect Centers.....	25
4.2.1.1 The Aluminum Center.....	25
4.2.1.2 The Germanium Center.....	29
4.2.1.3 The Titanium Center.....	31
4.2.2 Vacancy Defect Centers.....	32
4.2.2.1 The E_1' Center.....	32
4.2.2.2 The Oxygen Hole Center.....	35
4.3 Thermal Stability of Paramagnetic Centers.....	36
CHAPTER 5: FAULTING.....	39
5.1 The Development of Faults.....	39
5.2 Faulting.....	40

	Page
CHAPTER 6: ESR DATING OF FAULTS.....	44
6.1 A Review of Previous Work.....	44
6.2 Theory of ESR Dating of Fault Gouge.....	50
6.2.1 General Concept.....	50
6.2.2 The Plateau Method for Dating of Fault Gouge....	52
6.3 Experimental Goal.....	54
CHAPTER 7: EXPERIMENTAL METHODS.....	57
7.1 Sample Preparation.....	57
7.2 Irradiation.....	58
7.3 Measurement of ESR Spectra.....	59
7.4 Fault Simulation Experiment.....	64
7.5 Bleaching Experiment.....	67
CHAPTER 8: RESULTS OF EXPERIMENTAL STUDIES.....	69
8.1 Effect of Grain Size on ESR Intensity and Dose.....	69
8.2 Results of the Compression Experiment.....	71
8.3 Results of the Bleaching Experiment.....	75
CHAPTER 9: AD MEASUREMENT ON NATURAL FAULT GOUGE.....	77
9.1 Geological Settings of Samples.....	77
9.1.1 The San Jacinto Fault, Anza.....	77
9.1.2 The San Andreas Fault, Palmdale.....	78
9.1.3 The San Gabriel Fault, at Big Tujunga Canyon....	79
9.2 Age of Fault Movement for Natural Faults.....	83
9.2.1 Assumptions for the Age Calculation.....	83
9.2.1.1 Determination of U, Th, and K Dose Rates....	83

	Page
9.2.1.2 Attenuation.....	83
9.2.1.3 Alpha Dose.....	84
9.2.1.4 Beta Dose.....	84
9.2.1.5 Gamma and Cosmic Ray Correction.....	86
9.2.1.6 Correction for Water in the Matrix.....	87
9.2.1.7 k Value (Alpha Efficiency).....	87
9.3 Sample Age Calculation.....	88
9.4 Disequilibrium.....	90
9.4.1 Uranium Disequilibrium.....	90
9.4.2 Determination of DR Assuming ^{234}U Leaching.....	94
9.4.3 Radon Loss.....	94
9.4.4 Determination of DR Assuming 50% Radon Loss and 10% ^{234}U Leaching.....	96
9.5 Error Determination.....	96
9.6 Calculated Ages.....	97
9.6.1 The Results of AD Determinations on Real Faults.....	97
9.6.2 Table 9.1.....	99
9.6.3 Age vs. Grain Size.....	99
CHAPTER 10: DISCUSSION.....	105
10.1 Variation of AD and Age with Particle size.....	105
10.2 Mechanism of Zeroing of the ESR Signal during Faulting.....	108
10.2.1 Heating.....	108
10.2.2 Elastic and Non-Elastic Deformation.....	109

	Page
10.3 The Preferential Zeroing of Centers.....	115
10.4 Bleaching.....	117
10.5 The Plateau Criterion for Estimating Total Zeroing.....	118
10.6 Age Calculations.....	119
CHAPTER 11: CONCLUSIONS.....	120
REFERENCES.....	122
APPENDIX A.....	131
A.1 The Physical Basis of ESR Spectroscopy.....	131

List of Figures

Figure	Page
2.1 Illustration of the trapping process.....	8
2.2 Determination of AD by the additive dose method.....	10
2.3 The effect of saturation where intensity approaches I_{\max}	10
2.4 Comparison of the logarithmic and saturation growth curves for the San Andreas OH center.....	11
2.5a. Growth curve radiation effect for low irradiated samples.....	13
2.5b. Growth curve radiation effect correction.....	13
3.1 A block diagram of an ESR spectrometer.....	18
3.2a. An ESR absorption line.....	19
3.2b. The first derivative of the absorption line.....	19
3.3 Dependence of ESR intensity on the spectrometer stabilization.....	21
4.1a. An ESR line in cubic symmetry placed in an external magnetic field.....	23
4.1b. ESR fine splitting for a non-cubic field.....	23
4.1c ESR hyperfine splitting for a non-cubic field.....	23
4.2 Spectra of the principal centers in quartz.....	26
4.3a. Molecular model of the Al center.....	33
4.3b. Molecular model of the Ge center.....	33
4.3c. Molecular model of the Ti center.....	33
4.3d. Molecular model of the E'_1 center.....	37

Figure	Page
4.3e. Molecular model of the OH center.....	37
4.4a. Determination of mean-life by isothermal annealing experiments.....	38
4.4b. Arrhenius plot of mean-life obtained by isothermal annealing experiments.....	38
5.1 Chronological fault development.....	41
6.1a. A theoretical representation of ESR age vs. grain size for pre-faulted gouge.....	55
6.1b. A theoretical representation of ESR age vs. grain size for gouge at $t=0$	55
6.1c. A theoretical representation of ESR age vs. grain size for gouge at $t > 0$	55
6.2 A theoretical representation of age convergence for centers with different stress sensitivities.....	56
7.1 The procedure for ESR intensity measurement.....	62
7.2a. AD vs. ESR line number for the Al spectrum.....	63
7.2b. AD vs. ESR line number for the Ti spectrum.....	63
7.3 Hydraulic press diagram.....	65
8.1 ESR intensity vs. grain size.....	70
8.2 AD determination for a totally annealed bulk sample irradiated with 500 Gy.....	70
8.3a. Cumulative weight % vs. grain size for a sample artificially crushed at 29 MPa.....	72
8.3b. Cumulative weight % vs. grain size for a sample artificially crushed at 60 MPa.....	72

Figure	Page
8.4 AD resetting of the centers by pressure.....	73
8.5 Chi-square determined trends for the compression experiment.....	74
8.6 Bleaching of ESR intensity.....	76
9.1a. California index map.....	80
9.1b. A geological sketch map of the San Jacinto Fault near Anza.....	81
9.1c. A geological sketch map of the San Andreas Fault near Palmdale.....	81
9.1d. A geological sketch map of the San Gabriel Fault near the Big Tujunga Canyon.....	81
9.2a. AD vs. grain size for the OH, Al, and Ti centers for the San Jacinto Fault.....	102
9.2b. Age vs. grain size for the OH, Al, and Ti centers for the San Jacinto Fault.....	102
9.3a. AD vs. grain size for the OH, and Al centers for the San Andreas Fault.....	103
9.3b. Age vs. grain size for the OH, and Al centers for the San Andreas Fault.....	103
9.4a. AD vs. grain size for the OH, Al and E' centers for the San Gabriel Fault.....	104
9.4b. Age vs. grain size for the OH, Al and E' centers for the San Gabriel Fault.....	104
10.1 A crystal lattice dislocation diagram.....	112

Figure		Page
A1	Orientations of an electron in an external magnetic field.....	133
A2	Zeeman splitting into two energy levels E_+ and E_-	133

List of Tables

Table		Page
9.1	Data used in the determination of natural fault ages.....	101

Chapter 1: Introduction

1.1 General Introduction

The cost in damage and human losses resulting from devastating earthquakes is a factor that throughout history, human beings have accepted and learned to live with. However, in the last century, with an eruption of urban centers near tectonically active areas such as the San Andreas fault zone in California, the geological profession is being called upon to make evaluations of potential hazards associated with structures such as power dams, nuclear power stations, and residential buildings. While the recognition of faults is relatively easy, through structural and lithological discontinuity and fault zone deformation, predicting when and how often a particular fault will move is an elusive goal that geologists are currently trying to overcome.

Assuming that there are relatively constant stresses acting on the fault, then depending on various factors associated with the fault (lithology of the rocks in contact, depth of the fault, water circulation) a rough time dependent pattern of fault activity may be determined. Once this pattern has been established, recommendations can be given as to the safety of any structure that is to be built in the fault area, or the possible hazards that existing structures face.

This is a task that palaeoseismologists are presented with currently. In order to establish a temporal pattern for a fault zone, various dating methods have been employed that directly or indirectly date the time of previous fault activity. Some of the methods used are described below: methods of dating fault movements include using surface textures and weathering rinds of quartz grains in fault gouge (see page 42) as indicators of the relative age (Kanaori et al., 1980; 1985, and Colman 1987). K-Ar and Rb-Sr isotopes can be used to date the clay mineralization newly formed in the fault zone after movement has taken place (Kralik et al., 1987; Lyons and Snellenburg, 1974). Fission track dating of epidotes formed along the fault plane has been performed (Bar et al., 1974). The method of dendrochronology can record palaeofault movements through evidence recorded in environmental changes and broken parts of the tree (Jacoby 1987). Radiocarbon dating of plant material incorporated into the fault zone during fault movement may give an estimate of the time of last fault movement (Damon 1987). Thermoluminescent dating of colluvial wedge deposits that accumulate as a result of some fault movements has been suggested by Forman (1987). TL centers in the material are totally bleached by sunlight and upon burial (shielded from the sun) these traps repopulate and a time dependant accumulated dose builds up in the sample. Verosub (1987)

suggested using magnetostratigraphy in sediments cut by faults. Actual ages of the minerals (zircons) in the sediments can be determined by correlating the polarity of the samples with the Magnetic Polarity Time Scale. If this can be done for several stratigraphic units associated with the fault (transected or not), then a rough age of faulting can be established.

The method used for this study, electron spin resonance (ESR) spectroscopy on quartz grains from fault gouge was suggested by Ikeya (1982) in order to establish a history of movement for particular faults. This method is based on the premise that paramagnetic centers are totally annealed by high stress and temperature that occur on the shearing plane of the fault at the time of displacement. The effect of compressive stress on the ESR signal was tested by Miki and Ikeya (1982) and Fukuchi et al. (1986). They found a decrease in ESR intensity of the E'_1 , OH, Ge, and Al centers in quartz as a function of increasing pressure. Ariyama (1985) showed that pressures of at least 2 MPa and displacements of 50 cm are needed for the complete zeroing of the E'_1 and Ge centers. After this zeroing process has reset the ESR clock the lattice defects begin to trap quasi free electrons generated by high energy particles from radioactive impurities in the surrounding matrix. The measured ESR intensity is proportional

to the number of trapped electrons and therefore, the ESR signal of a sample should represent the time since the last fault movement.

1.2 Introduction to ESR

It was suggested by Zeller et al. (1967) that electron spin resonance (ESR) spectroscopy could be used as a method to date geological and archaeological samples. Materials on which ESR dating has been performed thus far are: speleothems, (Ikeya 1975, 1977; Hennig et al., 1981; Grün, 1985), corals (Radtke, 1987; Radtke and Grün, 1987; Radtke et al., 1987), mollusc shells (Katzenberger and Grün, 1985; Katzenberger and Willems, 1987; Ivanovich et al., 1983; Ikeya et al., 1981; Linke et al., 1985), teeth (Grün et al., 1987; Zymela et al., 1987), as well as samples from geological processes such as volcanic eruptions, (Imai et al., 1985; Imai and Shimokawa, 1985; Shimokawa et al., 1987; Shimokawa et al., 1984), and fault movements (Ikeya et al., 1982;1983; Miki and Ikeya, 1982; Fukuchi et al., 1986).

In the following I will discuss only the procedure and effects as they are related to ESR dating of quartz from fault gouge. For reviews of the dating technique see Ikeya (1978), Hennig and Grün (1983), Nambi (1985), and Grün (1987).

1.3 Objective

This study is based on the zeroing of ESR signals in quartz which requires that trapped unpaired electrons or holes be released and allowed to recombine. There are two processes by which trapped charges in quartz might be released during fault movement:

1) frictional heating on the fault surface provides the necessary activation energy (see Figure 2.1) for the electron or hole to escape the trap.

2) lattice breakage, induced by cataclasis of the grain causes destruction of the defects and, subsequently, the trapped electrons or holes are released.

Although both heating and deformation contribute to the overall zeroing of fault gouge during fault movements, it is the endeavour of the study to show the relative importance of cataclasis of grains over frictional heating, resulting in the complete or partial zeroing of ESR signals. This process results in depletion of ESR signal intensity in quartz, and therefore it would be possible to determine the time of last fault movement, if we could measure the accumulated dose (AD) in a quartz sample which was known to have been fully zeroed at the time of last movement. It is the objective of this thesis to establish criteria through which such material can be recognized.

The effect of pressure on the ESR signals in different grain sizes of quartz was investigated with the hypothesis in mind that larger grains might not have been as thoroughly zeroed as smaller ones. This is partly because shear displacements would tend to occur in the finer-grained matrix between the larger grains, and also because many of the smallest grains would represent particles that had broken off of irregular projections on the opposing rock-masses ("asperities"), and would have experienced maximal shear stress.

Chapter 2: Principles of ESR Dating

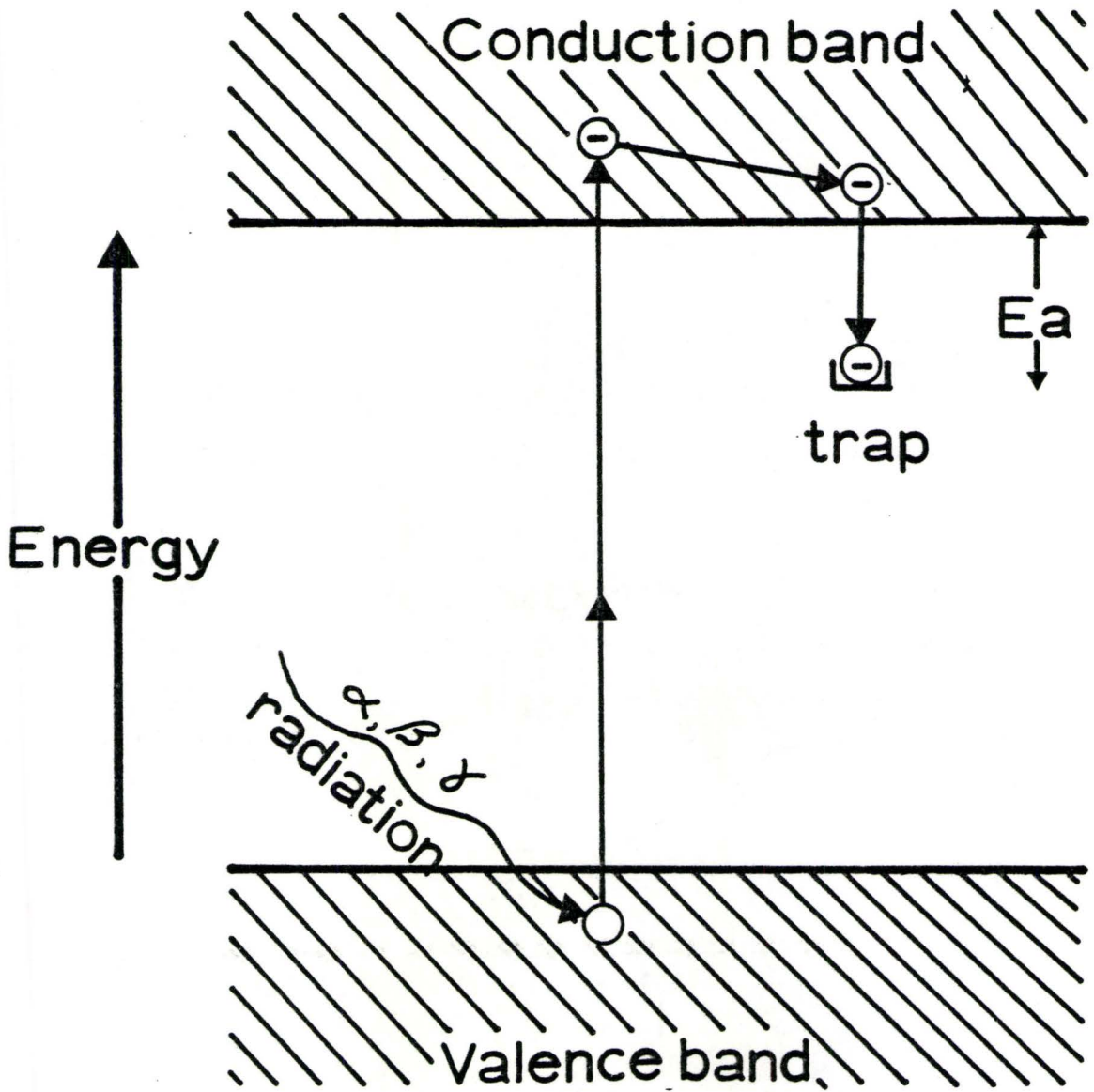
2.1 Physical Principles

Paramagnetic centers in a mineral arise from trapping unpaired electrons (e^-) or holes (e^+) at charge defects incorporated into the crystal lattice upon formation (Zeller et al., 1967). A defect is any position in the crystal structure representing a violation of the symmetry described by the symmetry space group of the crystal. In particular, charge defects are sites at which the effective charge is less than that required by the symmetric structure.

Radioactive impurities (U, Th, K, Rb, ^{14}C) incorporated into the sample itself and the surrounding matrix emit high energy particles (α -, β -, and γ - radiation) when they decay. Energy can be transferred from these high energy particles to electrons which are elevated from the valence to the conduction band. After a short time of diffusion the electrons recombine with holes near the valence band. The same electrons may however, be trapped at a defect site and form a paramagnetic center (Figure 2.1).

The number of trapped electrons which is proportional to the ESR signal, is a function of the radiation dose rate and the time (=age) the sample was exposed to this radiation field

Figure 2.1. Illustration of the trapping scheme of electrons in minerals.



An age can be deduced from the following equation:

$$AD = \int_0^t DR(t) dt$$

where AD is the radioactive dose the sample has accumulated over time and DR is the rate at which the dose has collected in the sample.

The accumulated dose (AD) is determined by the "additive dose method" where the ESR intensity of the natural sample is measured along with the ESR intensities of aliquots which were all γ -irradiated at different levels. Back extrapolation to zero ESR intensity gives the AD of the sample (Figure 2.2), which is measured in Grays (Gy).

2.2 Determination of AD

Linear back extrapolation, however, is normally not satisfactory for AD determination because the number of traps in a given sample is finite and the probability of an electron being trapped decreases as more are trapped. Saturation will eventually be reached when all traps are filled and the ESR intensity obtains a maximum value (I_{\max}) (Figure 2.3). This is accounted for by Apers et al. (1981) by plotting $-\ln(1 - (I/I_{\max}))$ against artificial γ -dose. The validity of the log-extrapolation curves can be tested by plotting the growth curves of samples that have been completely annealed. If the saturation curve matches the mathematically determined curve then the AD determined can be considered accurate (Figure 2.4)

Figure 2.2. Determination of AD by the additive dose method; back extrapolation to zero-ESR signal intensity gives the AD value.

Figure 2.3. The effect of saturation where the ESR intensity approaches I_{\max} .

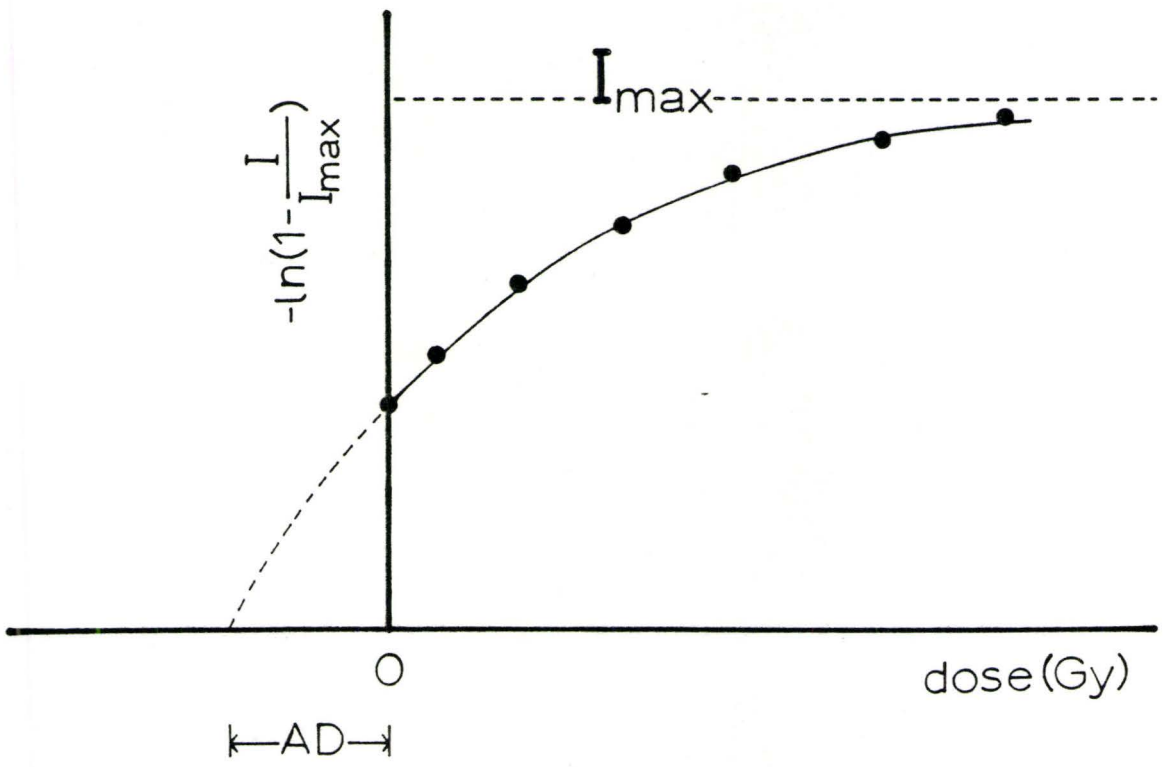
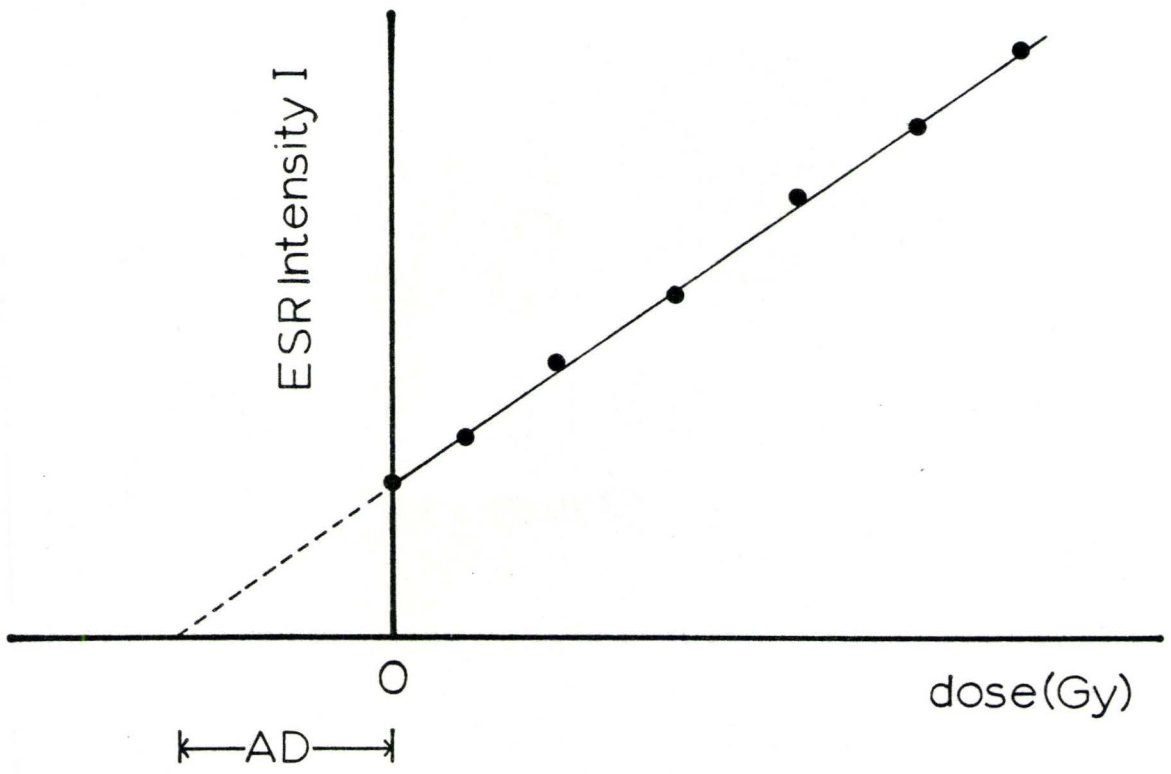
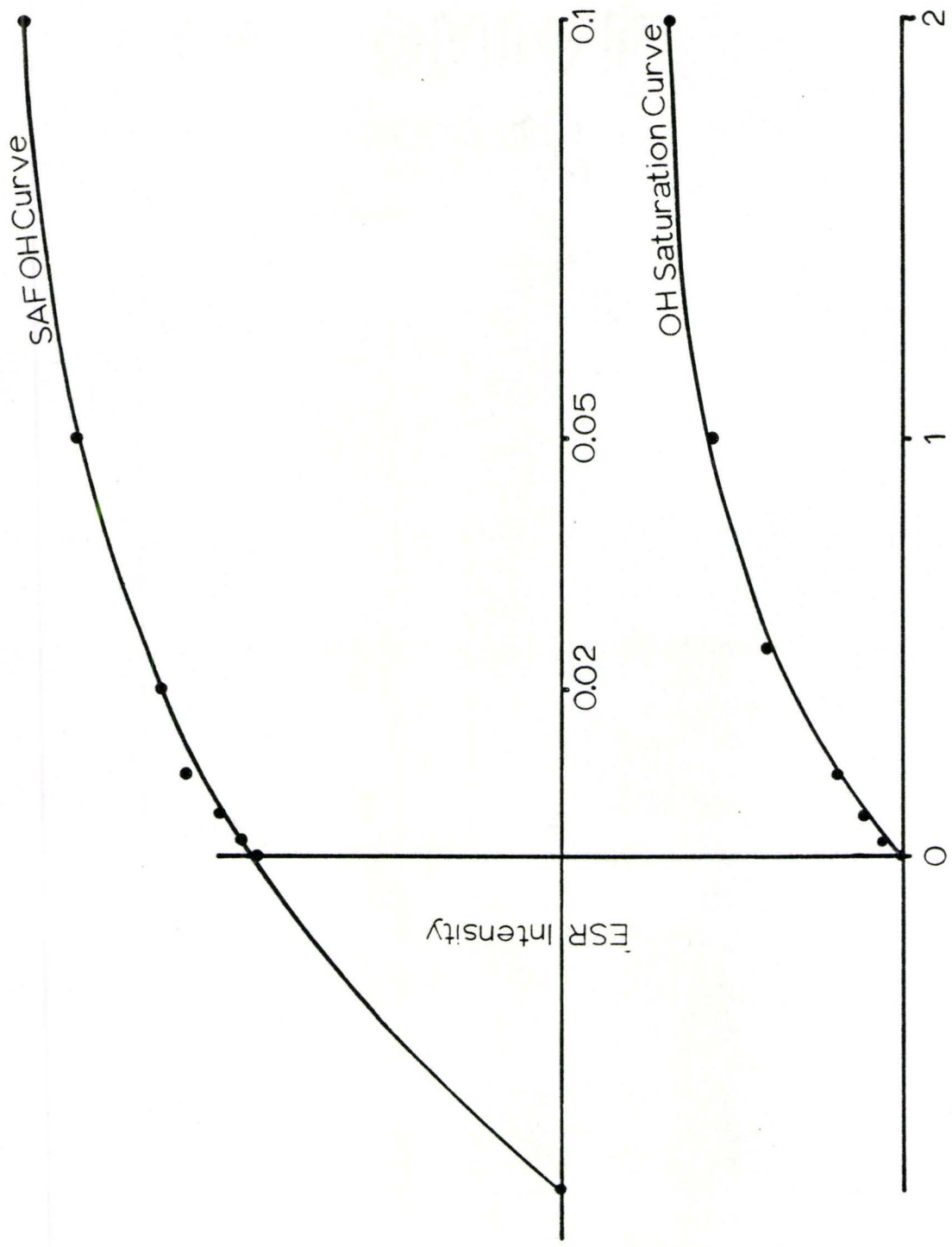


Figure 2.4. The logarithmic fit determined for the San Andreas OH center using the method from Apers et al., (1981), approximates the saturation curve for the completely annealed OH center on the same sample.



dose ($\text{Gy} \cdot 10^4$)

Some growth curves are complicated by a radiation effect where aliquots given a low irradiation dose lose some of their initial charge and end up with a lower ESR signal intensity than the natural, unirradiated sample (Figure 2.5). This may be explained by low irradiation levels predominantly emptying unstable traps instead of creating new centers, thus, lowering the ESR intensity. At higher irradiation levels the formation of paramagnetic centers will outweigh unstable trap deletion and the intensity increases. This effect will therefore introduce error into the additive dose method of AD determination (a low AD) which must be corrected for by a correction factor " δ " added to the AD (see Figure 2.5). It may also be corrected for directly by annealing the sample (after irradiation) for a time period (a few weeks to a couple of months) at a low temperature (50-100°C)(Figure 2.5b) (Levy, pers. comm.).

2.3 Determination of DR

To determine the dose rate, precise information about the amount of radiation that the sample is receiving from internal and external radioactive impurities is needed. External γ - and cosmic radiation can be obtained by inserting a portable dosimeter unit directly into or near the sample site for a period of time. This gives an accurate measure of dose rates being received by the sample at the time of its removal.

Figure 2.5a. A growth curve for a sample of quartz shows a radiation effect for low irradiated specimens which must be accounted for by the correction factor " δ ".

Figure 2.5b. The growth curve for the same sample as plotted in Figure 2.5a after 2 weeks of continuous heating between 75-100°C.

The determination of U, Th (through neutron activation) and K (XRF) in the matrix surrounding the sample, and within the sample itself gives the α - and β - external and internal dose rates respectively. The measured concentration of radioactive elements can be converted into dose rates by published tables (e.g. Nambi and Aitken, 1986). If external γ - and cosmic dose rates are not measured in situ then the γ -dose rate can be calculated from chemical analysis; the cosmic dose rate is dependent on altitude, latitude and attenuation by overlying sediment and can be estimated by graphs published by Prescott and Stephan (1982); (below 7m the cosmic dose rate is negligible).

For quartz there are trace amounts of U and Th within the crystal structure and therefore an internal as well as an environmental dose rate may be determined. Mejdahl (1987) shows that U and Th content in quartz is on average below 0.5 ppm and 0.4 ppm respectively.

The external dose rate, however, may not have been constant over the entire geological history of the sample due to variation of the radioactive impurities around the sample and due to the presence of water. Attenuation of radioactive particles is higher in water than in dry soil and therefore the dose rate may have varied in the past. These are all

uncertainties incorporated into calculation of the age of the sample, and will be discussed in detail later.

2.4 Attenuation of Radioactive Particles

The additive dose method determines the AD of the sample for aliquots irradiated with γ -rays only, using a ^{60}Co source. In nature, however, the sample is bombarded by not only γ -rays, but with α -, and β -rays also. Alpha particles have a penetration range of 5- 40 μm in a medium with a density of 2.5 g/cm^3 . This low range of penetration means that α -rays from the environment only induce electron trapping at the outer surfaces of the sample. Beta particles are energetic electrons (β^-) with a penetration range of about 2mm (in 2.5 g/cm^3). They tend to diffuse rather than follow straight paths and produce backscattering effects at the surface of the sample. Gamma particles are photons (emitted when a nucleus goes from a higher to lower energy level) with an average penetration depth of about 30cm ($\rho=2.5 \text{ g}/\text{cm}^3$). Therefore, they are not significantly attenuated in the samples used here.

For age assessment, attenuation factors of α -, and β -particles must be incorporated into the age calculation. Nambi and Aitken (1986) calculated the dose rates per concentration unit of radioactive elements. These are used in conjunction with attenuation factors for α -, and β - particles in quartz (Bell, 1980; Mejdahl, 1979) in the age equation for quartz

given by Grün (1987), shown below: (the internal dose in quartz grains is assumed negligible here)

$$\begin{aligned}
 DR = & C_U(SED) (k W_\alpha(SED) G_{U-\alpha} D_\alpha + W_\beta(SED) G_{U-\beta} D_\beta + W_\gamma(SED) D_\gamma) \\
 & + C_{Th}(SED) (k W_\alpha(SED) G_{Th-\alpha} D_\alpha + W_\beta(SED) G_{Th-\beta} D_\beta + W_\gamma(SED) D_\gamma) \\
 & + C_K(SED) (W_\beta(SED) G_{K-\beta} D_\beta + W_\gamma(SED) D_\gamma) + G_{cos} D_{cos} \quad (2.1)
 \end{aligned}$$

Where $G_{\alpha, \beta, \gamma, cos}$ = attenuation factors for α, β, γ , and cosmic rays

$W_{\alpha, \beta, \gamma}$ = water correction factors for α, β , and γ rays (incorporated into the equation if the % of water in the matrix is known)

D = dose rate per unit concentration

D_{cos} = cosmic dose rate

k = α efficiency

$C_{U, Th, K}$ = concentration of radioactive elements present

- if the external γ - and cosmic dose rates are measured by a portable dosimeter the above formula is simplified to:

$$\begin{aligned}
 DR = & C_U(SED) (k W_\alpha(SED) G_{U-\alpha} D_\alpha + W_\beta(SED) G_{U-\beta} D_\beta) \\
 & + C_{Th}(SED) (k W_\alpha(SED) G_{Th-\alpha} D_\alpha + W_\beta(SED) G_{Th-\beta} D_\beta) \quad (2.2) \\
 & + C_K(SED) (W_\beta(SED) G_{K-\beta} D_\beta) + MD_\gamma + MD_{cos}
 \end{aligned}$$

where $MD_{\gamma, cos}$ = measured dose rate of γ , and cosmic rays

Chapter 3: The ESR Spectrometer

An ESR spectrometer is capable of measuring paramagnetic centers and radicals. These are produced in a crystal by trapping an electron at charge deficit sites. An ESR signal results from an interaction of the magnetic moment of an electron in an external magnetic field with induced electromagnetic energy. For a general introduction into the physical basis of ESR spectroscopy see Appendix A or the reader is referred to Abragam and Bleaney (1986), and Marfunin (1979).

An ESR spectrometer consists of three components: an electromagnet, a klystron with wave guides for generating microwaves, and an electrical signal detection and recording unit (Figure 3.1).

The electromagnet produces a magnetic field which is absolutely homogeneous in the region of the cavity. Microwave energy is generated by the klystron and conducted to the resonant cavity by a waveguide. To record a signal of a free electron (g -value = 2.0023) a microwave frequency in the range of 9.5GHz (X-band) is used at a magnetic field strength of $H \approx 3500$ Gauss. The geometry of the waveguide and the cavity

Figure 3.1. A block diagram of an ESR Spectrometer.

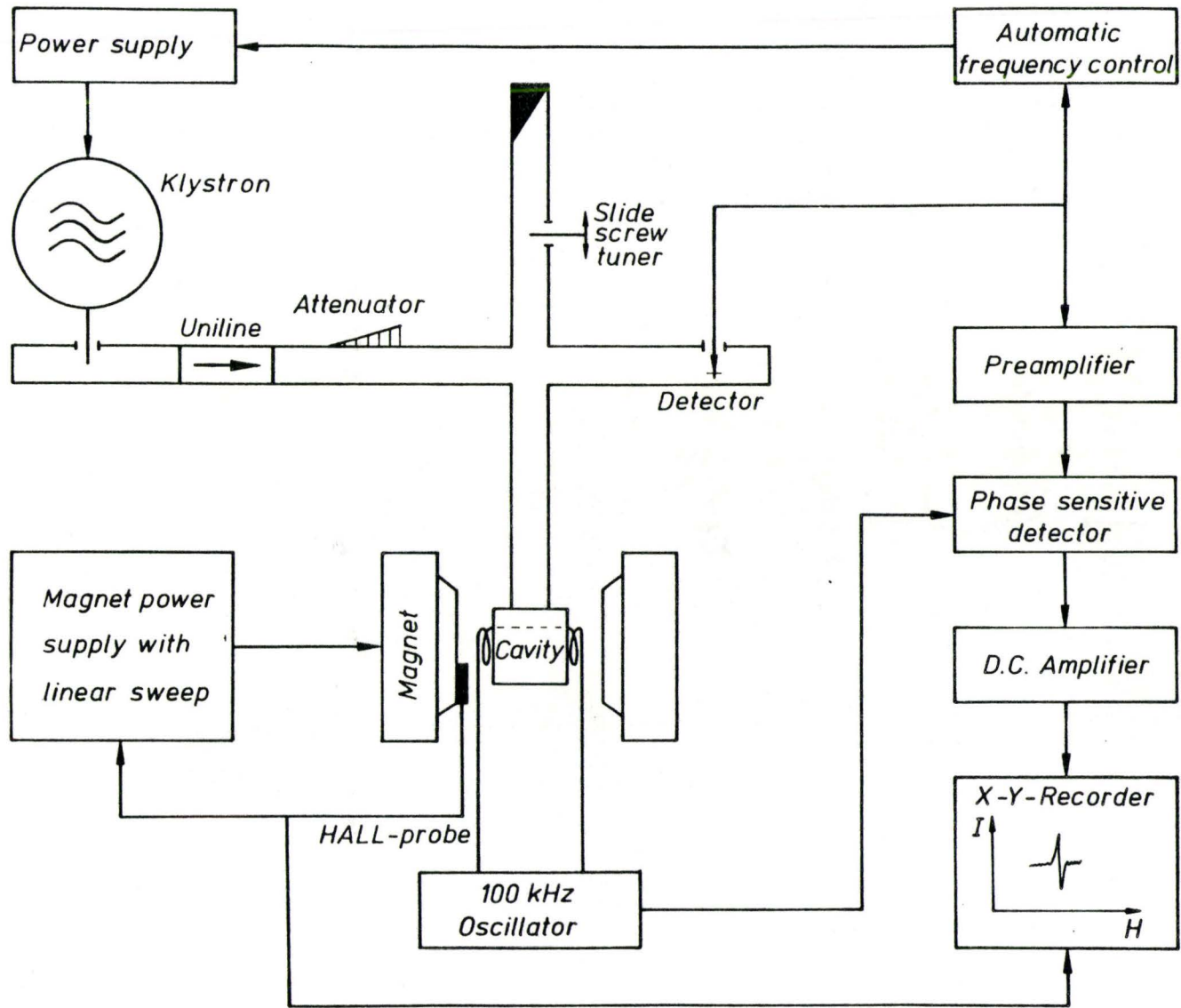
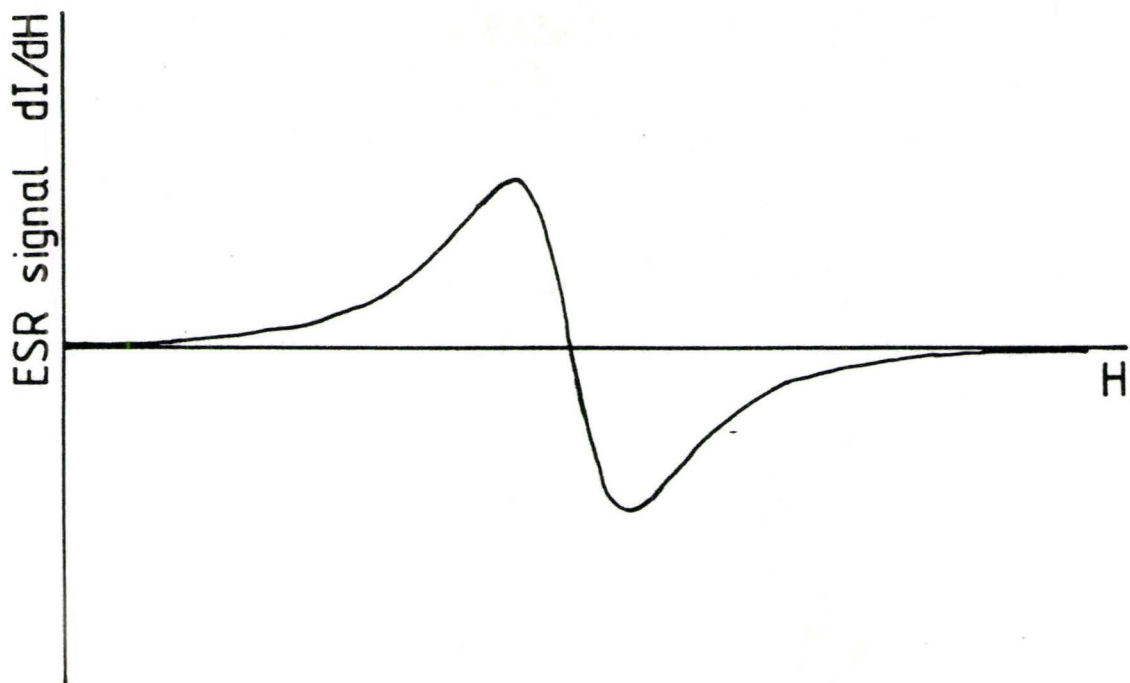
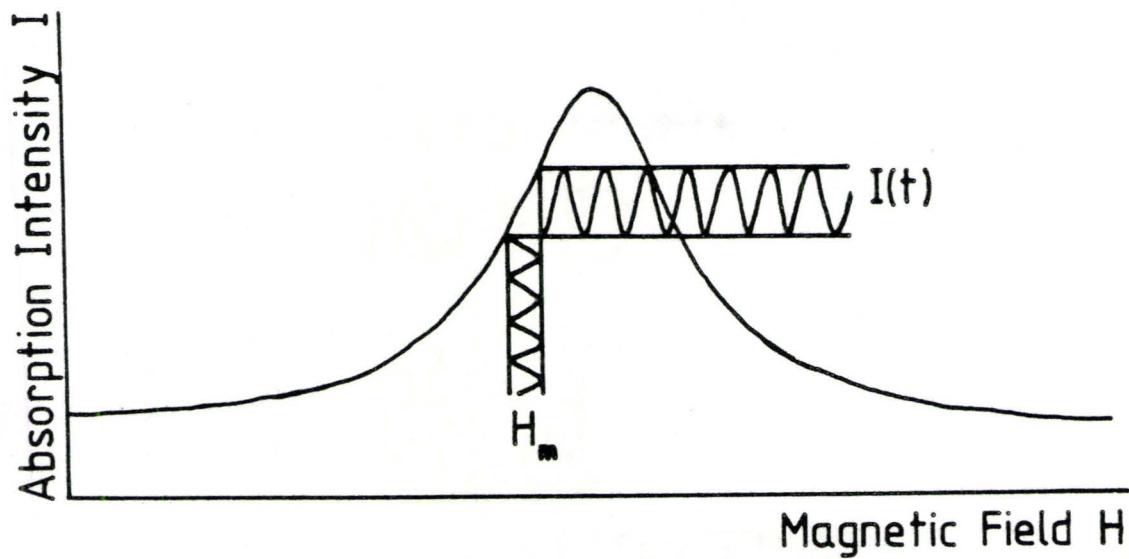


Figure 3.2a. An ESR absorption line

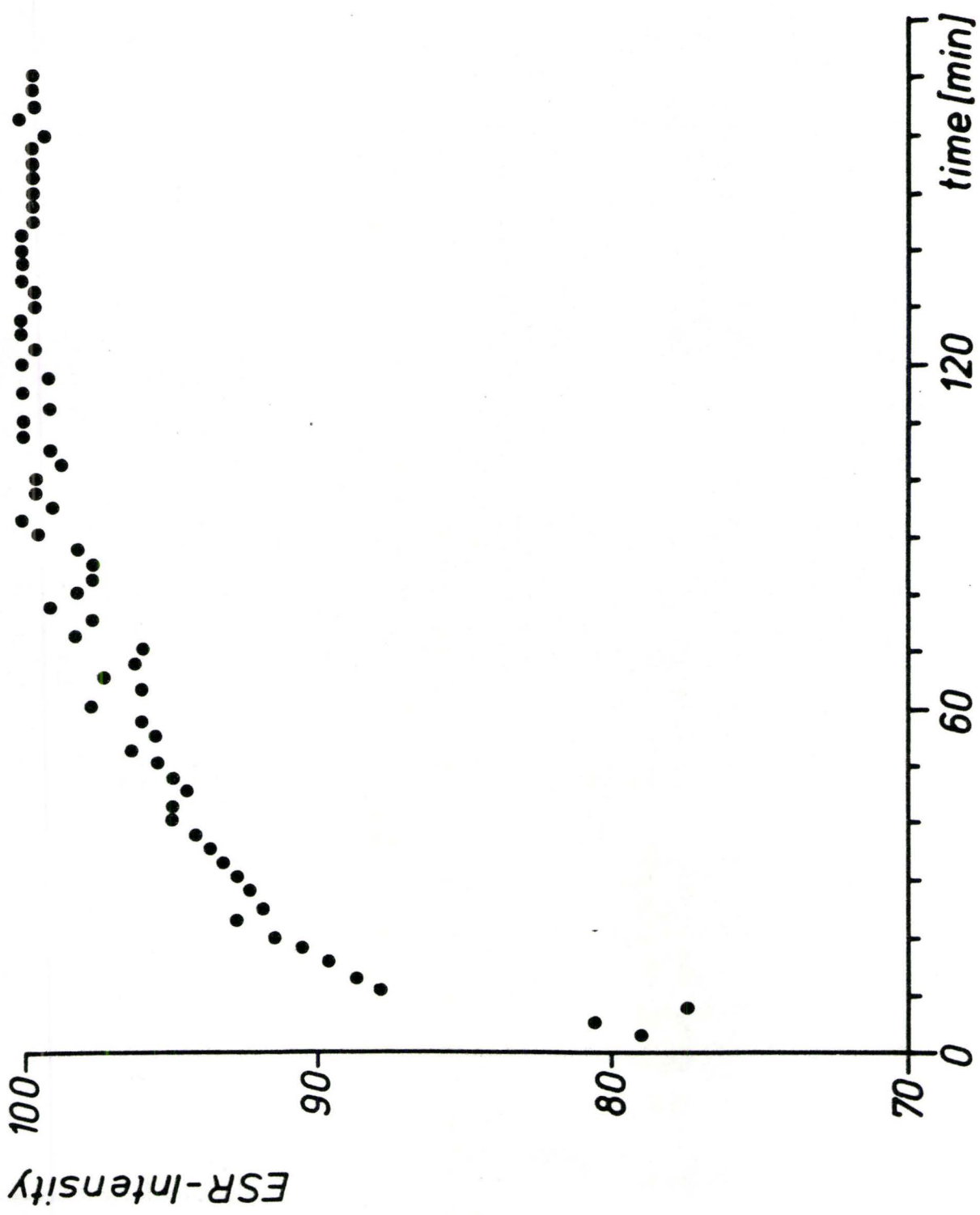
Figure 3.2b. The first derivative of the absorption line, the ESR signal, is shown.



defines the microwave frequency used and is therefore not variable. Instead, the strength of the magnetic field is varied until an absorption signal is detected (Figure 3.2a). The signal is then amplified and processed by a phase sensitive detector and transferred to an X-Y recorder, which plots the derivative of the absorption signal (ESR intensity I) against the magnetic field strength (Figure 3.2b). The ESR intensity is proportional to the total number of trapped electrons or holes. (see Grün, 1987 and Ikeya, 1985).

Before starting ESR measurements, the spectrometer should have reached thermal stability. Before thermal equilibrium, the ESR signal heights are unsettled, which can lead to a false AD determination. The ESR spectrometer at McMaster has a 3 hour stabilization period in the operate mode (Figure 3.3).

Figure 3.3. ESR signal intensity change after switching the ESR spectrometer on (from Grün, 1987).



Chapter 4: ESR Spectra

4.1 General

ESR signals are very often separated into multiple lines where each line is associated with a different paramagnetic center or may arise due to fine (fs), hyperfine (hfs), and superhyperfine (shfs) splittings of the original spectra.

Spectra, broadened by splittings, are generally associated with strong interaction of electron spin with the crystal lattice (short spin-relaxation-time), while narrow spectra have a weak interaction (long spin-relaxation-time).

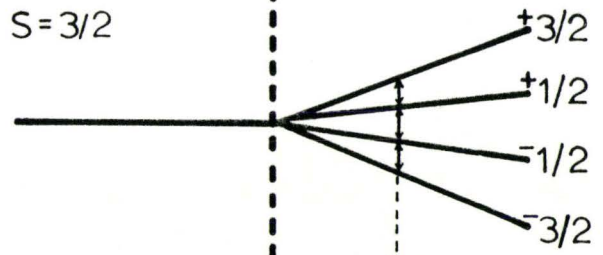
Fine structure results from a magnetic interaction between the orbital magnetic moment and the intrinsic moment of electrons with the same energies. The trapped electron may have the same energy as an indigenous electron, in which case a spin coupling occurs. The interaction of the external magnetic field with the crystalline magnetic field (generated by all minerals), causes fine splitting. An external field interacting with a cubic crystalline field will produce a single line (Figure 4.1a), while interaction with a non-cubic field causes fine splitting of the spin levels (Figure 4.1b).

- Figure 4.1. a). A single ESR line is observed for a cubic crystalline field placed in an external magnetic field.
- b). ESR fine splitting for non-cubic crystalline field for spin $S=3/2$.
- c). ESR hyperfine splitting for ions with spin $S=1/2$ and nuclear spin $I=3/2$.

a

cubic crystal field

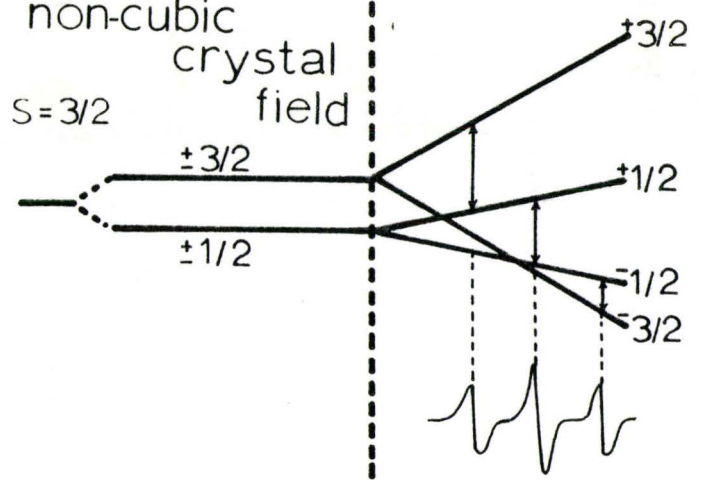
$S=3/2$



b

non-cubic crystal field

$S=3/2$



c

crystal field

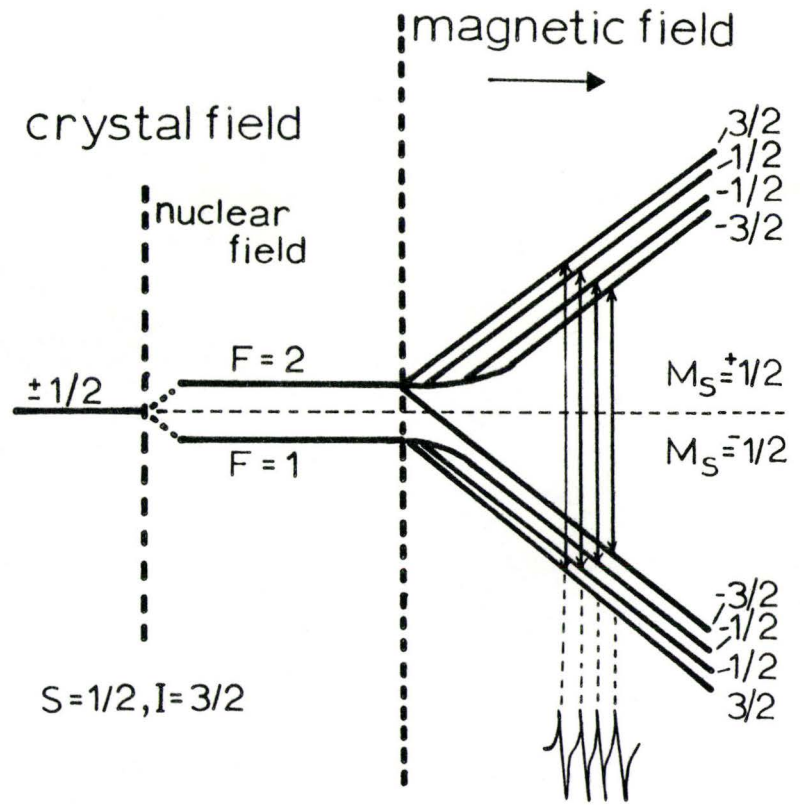
$\pm 1/2$

$F=2$
 $F=1$

$S=1/2, I=3/2$

nuclear field

magnetic field →



Hyperfine splitting is caused by the interaction of the magnetic moment of an electron with the nuclear magnetic moment (M_I) of the atomic nucleus. The motion of the electron around the nucleus is controlled by nuclear mass, and therefore isotopes of the same element with the same nuclear charge but different masses will give different spectra lines, and thus a splitting occurs. The volume of one isotope over the other will also effect the type of hyperfine splitting of the spectra (Figure 4.1c).

Superhyperfine splitting of the spectra is a result of magnetic interaction of the electron with the nucleus of surrounding atoms (interstitial atoms or neighboring lattice cations).

Therefore the total spectrum of a particular paramagnetic center in an external magnetic field is described by a spin-Hamiltonian operator, H_S .

$$H_S = \text{fs structure} + \text{splitting by external H (g } \mu_B \text{ H)} + \text{hfs structure} + \text{shfs structure.}$$

4.2 ESR Centers in Quartz

Two defect types can be found in quartz:

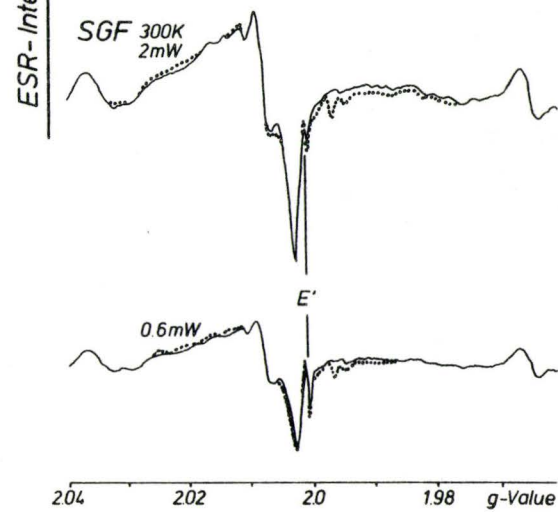
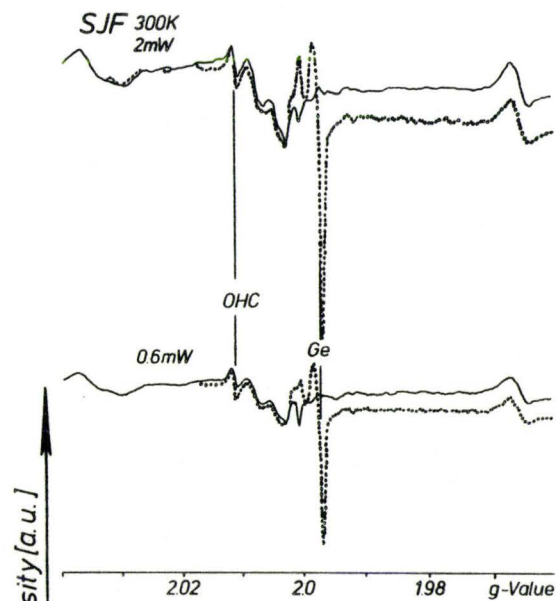
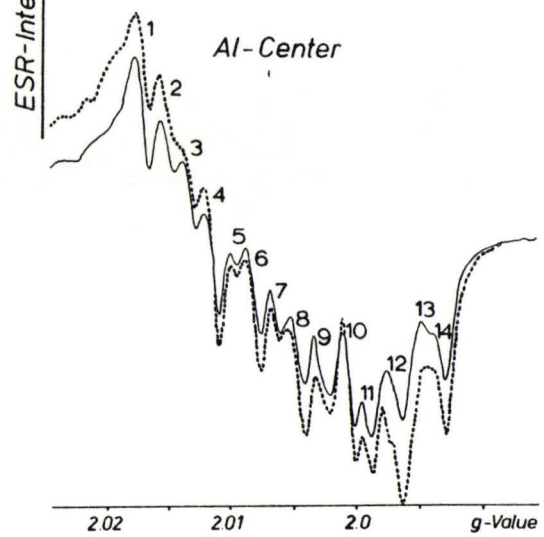
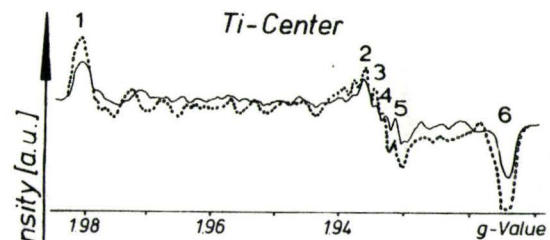
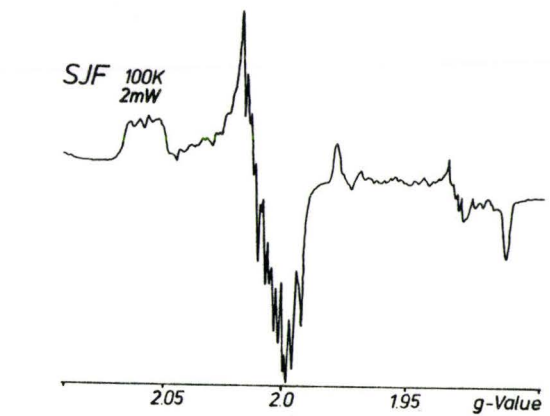
- 1) impurity ions (isomorphous or interstitial),
- 2) anion or cation vacancies define five paramagnetic centers (Al, Ge, Ti, E'_1 , and OH) that are radiation sensitive. Other ESR peaks found at g-values 2.0071, 2.0037, and 2.0024 (at 300K) do not increase with artificial irradiation (Figure 4.2).

4.2.1 Impurity Defect Centers

4.2.1.1 The Aluminum Center

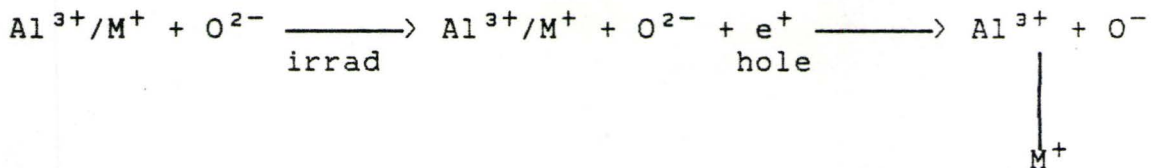
The aluminum center is a hole trapping center that occurs as a result of an Al^{3+} ion replacing a Si^{4+} ion in tetrahedral coordination. Hyperfine structure results from interaction of the hole with the ^{27}Al nucleus ($I=5/2$, 100%) and gives a distinctive six-line ESR spectrum. The Al center consists of a hole trapped in a nonbonding 2p orbital of an oxygen bridging between the substitutional Al^{3+} ion and neighboring Si^{4+} ion, with the orbital of the unpaired spin being perpendicular to the plane defined by the Si-O-Al bond (Griscom, 1978), (Figure 4.3a). According to the model proposed by O'Brien (1955), an Al atom and a monovalent atom (e.g. H^+ , Li^+ , Na^+) enter the lattice together during crystallization in place of a Si^{4+} ion. The Al^{3+} ion forms covalent bonds with four O^{2-} anions,

Figure 4.2. Spectra of the principal centers used in ESR dating of quartz. Left: spectra at 100K. Top: total spectrum of San Jacinto fault gouge; middle: detail of Ti center; dashed line: irradiated sample (100 Gy); bottom: detail of Al peak, showing hyperfine splitting of peak. Right: spectra at 300K; top: OH and Ge centers in San Jacinto fault gouge; bottom: E_1' center in San Gabriel fault gouge, showing effect of varying microwave power.



using the valence electron of the monovalent atom to supply the one it lacks. This monovalent ion takes up an interstitial location, held by the negative charge on the Al site. Initially all electrons are paired (diamagnetic) so that no ESR signal can be recorded.

The electron from the monovalent atom used by the Al atom to bond an oxygen is superfluous. Irradiation removes this superfluous electron and thus one of the oxygen anions becomes an atom with a hole in its valence shell. The monovalent ion would then migrate from the interstitial site since there is no charge holding it. This is schematically shown below:



The migration of the monovalent alkali ion out of the center is consistent with the lack of alkali (documented by shfs) in the Al spectrum. Evidence of this migration was provided by MacKey (1963) who found that alkali ion shfs were still present in Al spectra in samples γ -irradiated at 77 K. The alkali ion does not have sufficient thermal energy to diffuse away even though it is no longer needed as a charge compensator. As temperature was increased, the alkali ions were found to transfer to the Ge center which Cohen and Smith (1958) established as an electron trap complementary to the Al

center. After this transfer the Ge-ESR spectra shows shfs (see the Ge center section).

The Al signal is not observed at temperatures above 200 K in crystalline quartz due to line broadening (Schnadt and Rauber, 1971). This effect arises from a thermally activated hopping of the hole among different oxygen ligands around the aluminum impurity. This explanation was suggested by Taylor and Farnell (1964) after the ESR spectra of crystalline quartz and silica glass, where the Al-ESR spectra observed at room temperature, were compared. The stoichiometric arrangement of ligand ions (O^{2-}) around the Al cation determines whether thermal hopping of the hole can occur. In crystalline quartz there are at least two equivalent ground-state oxygens on each AlO_4 tetrahedron between which a hole can make thermally excited transitions. For silica glass however, local statistical distortions make all of the ligand ions non-equivalent and therefore, after irradiation only one of the ligand oxygens is able to capture a hole. Thermally activated hopping of the hole is not allowed between non-equivalent oxygens and therefore, no relaxation and no line broadening of the Al spectra in silica glass is observed. Therefore, the ESR spectra of the Al hole center in crystalline quartz must be studied at low temperatures ($\leq 100K$) due to relaxation broadening effects.

The Al center is thermally the most unstable center in quartz. Decay is first noticed at 150°C, proceeding to 80% at 200°C. Total thermal decay occurs between 250-300°C (Shimokawa et al. 1987).

4.2.1.2 The Germanium Center

There appear to be two families of defects associated with silicon substituted by germanium in quartz. The first family is characterized by the spin density of the trapped electron being largely concentrated on the Ge ion (Figure 4.3b). The two classes of this family of Ge centers are reported by Anderson and Weil (1959) and Weil (1984) to be bare Ge centers $[\text{Ge e}^-]$, which are unstable at room temperature, and alkali compensated Ge centers $[\text{Ge e}^-/\text{M}^+]$, which are stable but slowly decay when exposed to light (see Figure 8.5). The alkali compensated center $[\text{Ge e}^-/\text{M}^+]$, was observed by MacKey (1963) who suggested the model of an interstitial M^+ ion initially acting as a charge compensator for a pre-hole trapping Al center subsequently being released and finding its way to a $[\text{Ge e}^-]$ site where it charge compensates and stabilizes a trapped electron. The $[\text{Ge e}^-/\text{M}^+]$ spectra shows superhyperfine structure which occurs, through interaction of the electron with the nuclei of the compensator ions.

A second family of Ge centers was reported by Feigl and Anderson (1970), as having 90% spin density localized in a germanium hybrid orbital projecting along the Si-O bond direction. This localization along the Si-O direction may define a Ge related E' center $[\text{Ge}(111,1\text{V})\text{e}^-]$ with an oxygen vacancy. Weil (1971), however, argued that this type of Ge center is not due to structural defects but rather this is a Ge^{2+} precursor site compensated by two M^+ ions (usually Li^+). Upon radiation (from external sources) this site captures a hydrogen atom which upon entering the site accepts an electron from the germanium ion forming Ge^{3+} . It has not been established which type of this family of Ge centers predominates in natural quartz samples and it may be that both are present.

According to Rakov et al. (1986) the $[\text{Ge e}^-/\text{M}^+]$ form accounts for 70-80% of the Ge center concentration. Feigl and Anderson (1970) found that the absorption spectrum of the $[\text{Ge e}^-/\text{M}^+]$ center is of sufficient intensity to mask the absorption lines of the $[\text{Ge}(111,1\text{V})\text{e}^-]$ center. In order to observe the $[\text{Ge}(111,1\text{V})\text{e}^-]$ spectrum, the $[\text{Ge e}^-/\text{M}^+]$ spectrum must firstly be suppressed. Feigl and Anderson (1970) describe a process in which controlled heating steps suppress the $[\text{Ge e}^-/\text{M}^+]$ spectrum while at the same time enhancing the $[\text{Ge}(111,1\text{V})\text{e}^-]$ spectrum.

The $[\text{Ge e}^-/\text{M}^+]$ center was not observed in the quartz samples used for this study. This is because care was not taken to shield the sample from light during sampling and sample preparation and, therefore, the Ge signal had faded. With proper safeguards, the Ge center can be used for ESR dating. Tanaka et al. (1985) showed that the Ge center can be used to date near shore Terrace sands that were zeroed by sunlight at the time they were deposited (see bleaching experiment results page 74).

The $[\text{Ge e}^-/\text{M}^+]$ center is not observed at lower temperatures (<200 K) due to an increased spin-relaxation-time (see appendix A). The Ge center starts to decay due to heating at approximately 300°C , and becomes totally annealed at 400°C .

4.2.1.3 The Titanium Center

The Ti center $[\text{Ti}^{4+} + \text{e}^- \longrightarrow \text{Ti}^{3+}]$ as described by Rinneberg and Weil (1972) results from an impurity Ti^{4+} ion substituting for a Si^{4+} ion. Experimental irradiation at low temperatures on rose quartz (high concentration of titanium), by Isoya and Weil (1979) provided evidence of a diamagnetic Ti species $[\text{TiO}_4]^0$ capturing an electron to form the paramagnetic Ti center $[\text{TiO}_4]^-$, which promptly decays at temperatures above 20 K. Irradiation at warmer temperatures was shown to facilitate the diffusion of compensator ions

(e.g. H^+ , Li^+ , Na^+) into interstitial lattice sites producing an stable paramagnetic (electron trapping center). The Ti center is therefore analogous to the $[Ge e^-/M^+]$.

Hyperfine structure from two titanium isotopes is observed; ^{47}Ti ($I=5/2$, 7.75%) and ^{49}Ti ($I=7/2$, 5.51%). Superhyperfine structure results from interaction of the trapped electron with compensator ions in interstitial sites (Figure 4.3c).

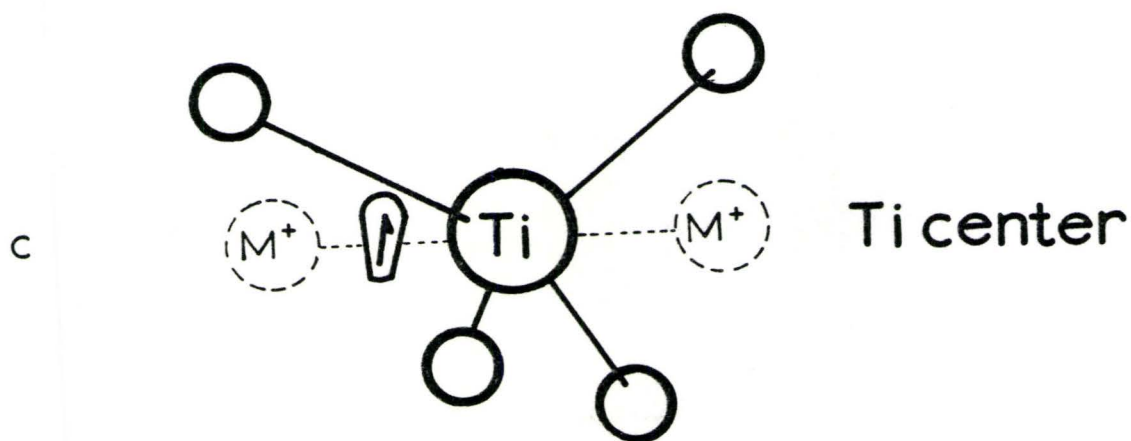
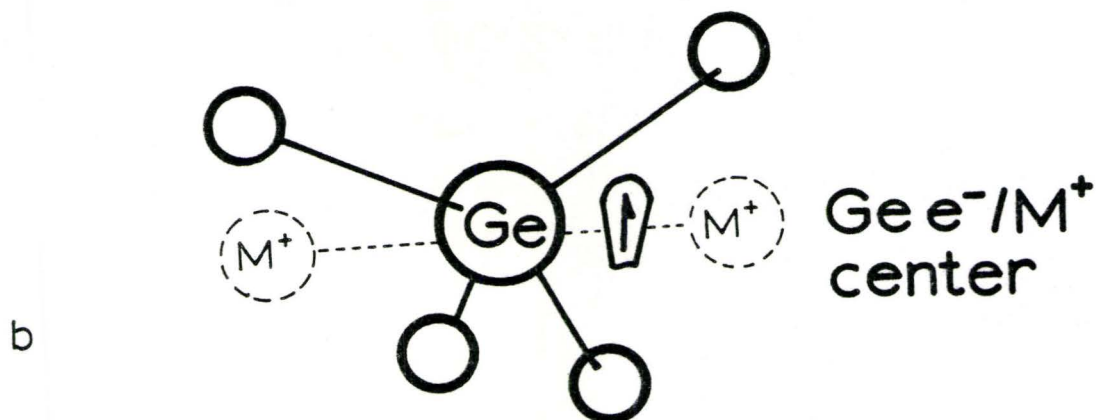
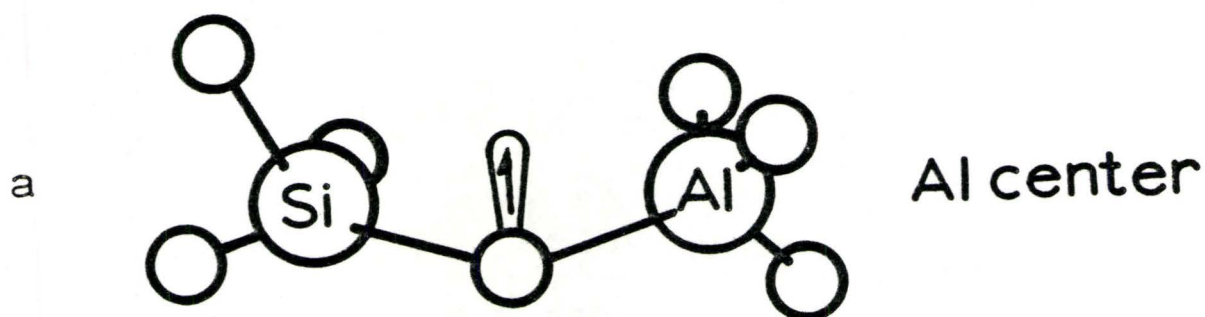
Like the Al center, the Ti center is not observed at room temperature due to line broadening.

4.2.2 Vacancy Defect Centers

4.2.2.1 The E'_1 Center

The E'_1 center $[O_3Si:SiO_3]$ is a defect center with a vacancy left by a O^- ion missing from a normal bridging oxygen location with consequent relaxation (Yip and Fowler, 1975; Isoya et al., 1981) of the silicon neighbours. In crystalline quartz the short bonded Si ion that is the one relaxed most towards the O^- vacancy bears most of the trapped electron spin density. The other Si ion is relaxed away (long bonded), from the vacancy (Figure 4.3d). This non-symmetric distribution of electron density over both Si atoms represents an initially diamagnetic precursor E center that will trap an unpaired electron liberated by irradiation (Feigl and Anderson, 1970).

Figure 4.3. Molecular models of the a) Al (after Griscom 1978), b) Ge, and c) Ti centers. The location of the trapped hole or electron is indicated by the arrow.



The unpaired electron of the E_1' center is localized in a non-bonding sp hybrid orbital on the short bonded Si cation facing an oxygen vacancy. Interaction of this unpaired electron with the ^{29}Si isotope ($I=1/2$, 4.7%) produces a slight hyperfine structure in the ESR spectra (Weeks and Nelson, 1960).

The E_1' center, although present, was not used for AD determination for the quartz fault gouge. Upon artificial irradiation, the ESR intensity of the E_1' center decreased, which indicates total saturation within the sample. Moiseyev and Rakov (1976) found that natural quartz is practically devoid of empty pre-centers. This was the case for most of the quartz samples used, which precluded the use of the E_1' center for dating, but this does not eliminate use of this center for dating of other samples. Thermal decay of the E_1' center occurs between 300-460°C, beyond which (460-500°C) an interstitial oxygen occupies the vacancy and decay becomes irreversible resulting in the disappearance of the E_1' altogether.

The E_1' is not observed at lower temperatures ($<200\text{K}$) due to an increased spin-relaxation-time (see Appendix A).

4.2.2.2 The Oxygen Hole Center

The OH center [$O^{2-} + O^- \longrightarrow O_2^{3-}$] has a cation deficit (Si^{+4} missing). With the Si^{+4} ion vacancy, two oxygen ions attract and occupy a structural site of their own, not an O_2 molecule (Figure 4.3e).

An unpaired electron occurs in the σ orbital (molecular orbital consisting of p_z orbitals of two oxygens) directly along the O-O bond (Bershov et al., 1978). With the loss of a cation, the structure becomes negatively charged and represents a trap for positive holes. In this case, one of the electrons in the O^{2-} anions becomes superfluous due to non-symmetrical distribution of electron density between the two oxygens. Irradiation will remove the superfluous electron and thus one of the anions becomes an atom with a hole in its outer shell.

Hyperfine structure may occasionally be seen in the OH ESR spectra due to the interaction of the hole (e^+) with ^{29}Si of neighboring tetrahedra and from protons (H^+) located in interstitial channels (Marfunin, 1979). The OH center is stable up to 250-300°C, beyond this signal intensity decreases rapidly until the spectrum totally disappears at $\approx 400^\circ C$.

The OH center is not observed at lower temperatures (<200K) due to an increased spin-relaxation-time (see appendix A).

4.3 Thermal Stability of Paramagnetic Centers

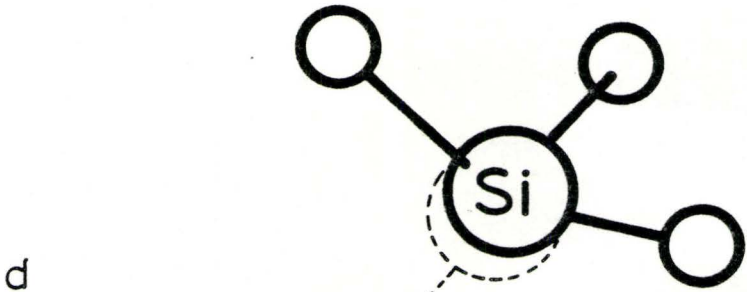
Centers used in ESR dating are of no use if they do not retain charge for long periods of time compared to the age of the sample. The mean-life of trapping centers at ambient temperatures can be estimated by an Arrhenius plot: mean-lives of the center determined at high temperatures by isothermal annealing experiments are extrapolated to ambient temperatures (Figure 4.4).

The mean-life at 25°C of the five centers in quartz used for this study are given below with their respective references:

<u>Center</u>	<u>Mean-life</u>	<u>Reference</u>
Al	$2.4 \cdot 10^6$ a	Shimokawa and Imai (1987)
Ge	$3.1 \cdot 10^9$ a	Shimokawa and Imai (1987)
Ti	N/A*	
E ₁	10^8 a	Moiseyev and Rakov (1976)
OH	$3.4 \cdot 10^9$ a	Shimokawa and Imai (1987)

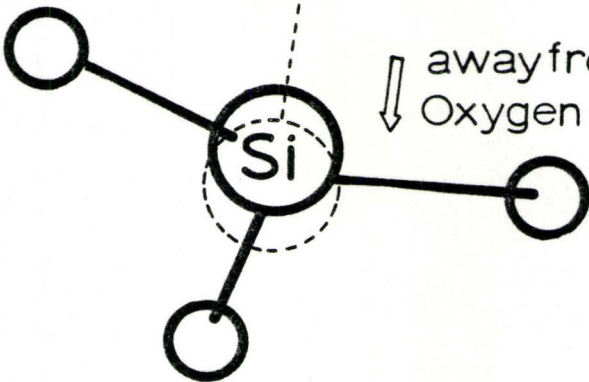
*not available

Figure 4.3. Molecular models of the d) E_1' (after Feigl et al. 1974), and e) OH centers. The location of the trapped hole or electron is indicated by the arrow.



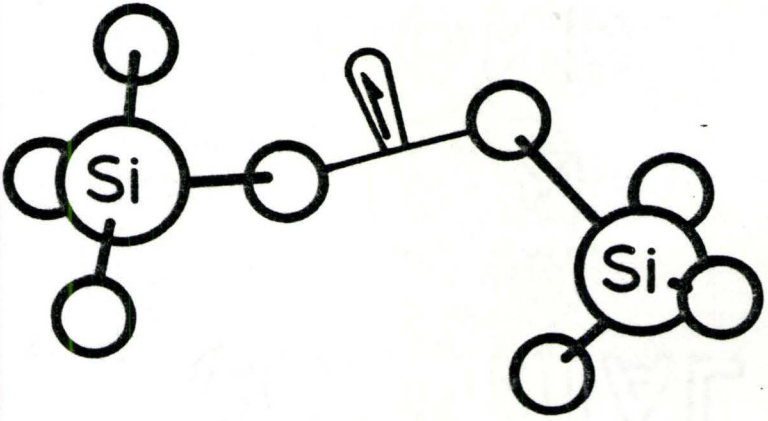
Si relaxation toward,

E_1' center



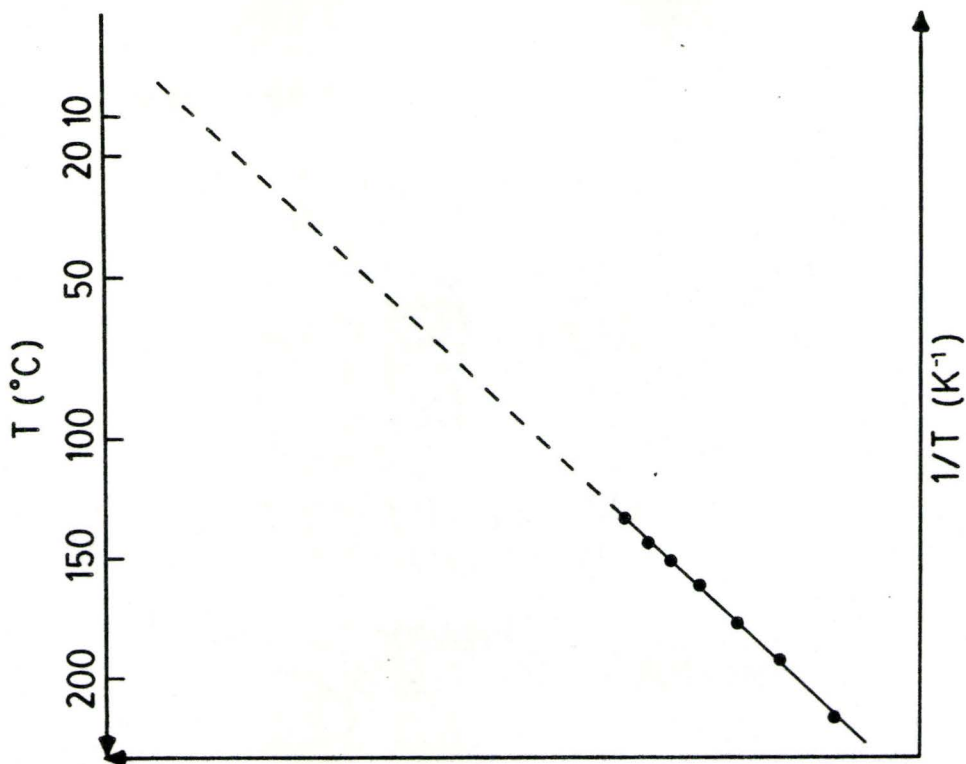
away from
Oxygen deficit

e



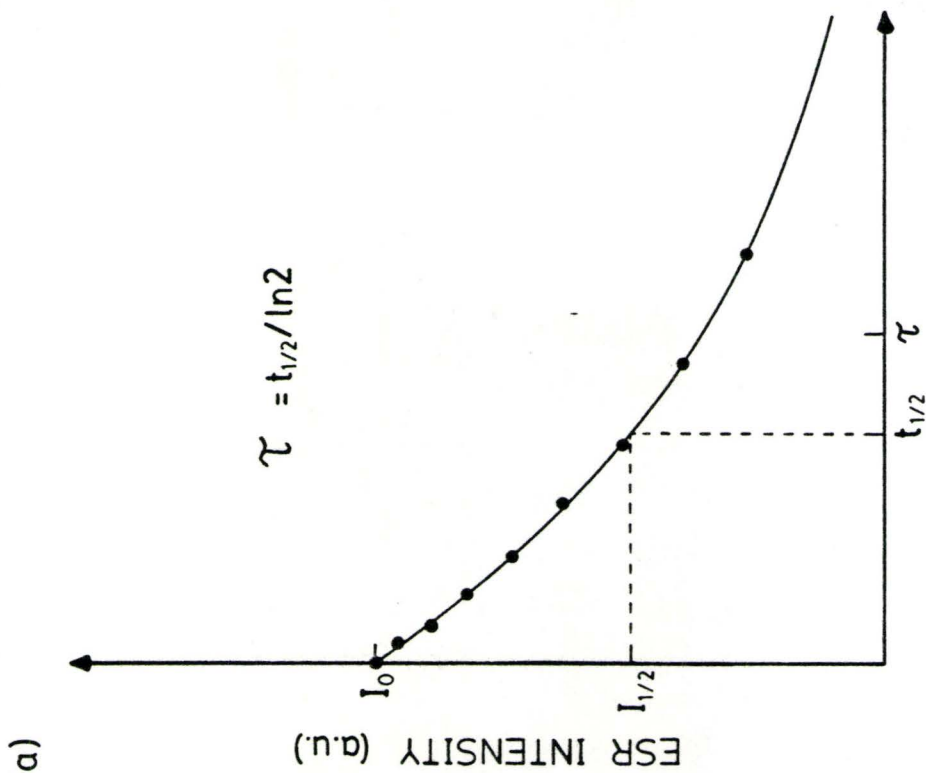
OH center

- Figure 4.4. a). Determination of mean-life (T) by isothermal annealing experiments.
- b). Arrhenius plot of the mean-life obtained for different temperatures. Extrapolation of the experimental mean-lives gives the estimated mean-life of the center at ambient temperatures.
- (after Zymela, 1985).



(s) 2 907

b)



a)

Chapter 5: Faulting

5.1 The Development of faults

Anderson (1942) first suggested that fault development proceeds as a mechanism where initially small fractures eventually develop into a large continuous fault. Aydin (1978) also showed how small deformation bands in sandstone may be important primary structures preceding the formation of larger faults. These deformation bands were on average 1 mm wide with the same mineralogical composition as the host rock, however the grains were smaller and the porosity had decreased significantly.

Successive deformation bands form subparallel to the initial band, and thus a development into zones of bands can be observed. Propagation to develop new bands, rather than new displacement along the initial deformation band, develops because decreasing porosity hardens the deformation zone. Also, there may be enough time between the deformation processes to allow a re-cementation of the band, which makes it stronger than the adjacent parent rock. The deformation is then shifted to the weaker parent rock and another band begins to develop, which defines a zone of deformation bands.

Aydin and Johnson (1978) noted that some zones along which large displacement has occurred were associated with slip surfaces. These slip surfaces exist at the margins of zones of deformation bands, and produced intense granulation of the grains located at these margins. The mechanism of large slip is not well understood, but may occur as a result of a reduction in strength at the marginal zones. The strain hardened bands in the zone should substantially add to the strength of the zone as a whole. This would set up an instability between the zone and the marginal parent rock, ultimately resulting in slip along their interface (Figure 5.1).

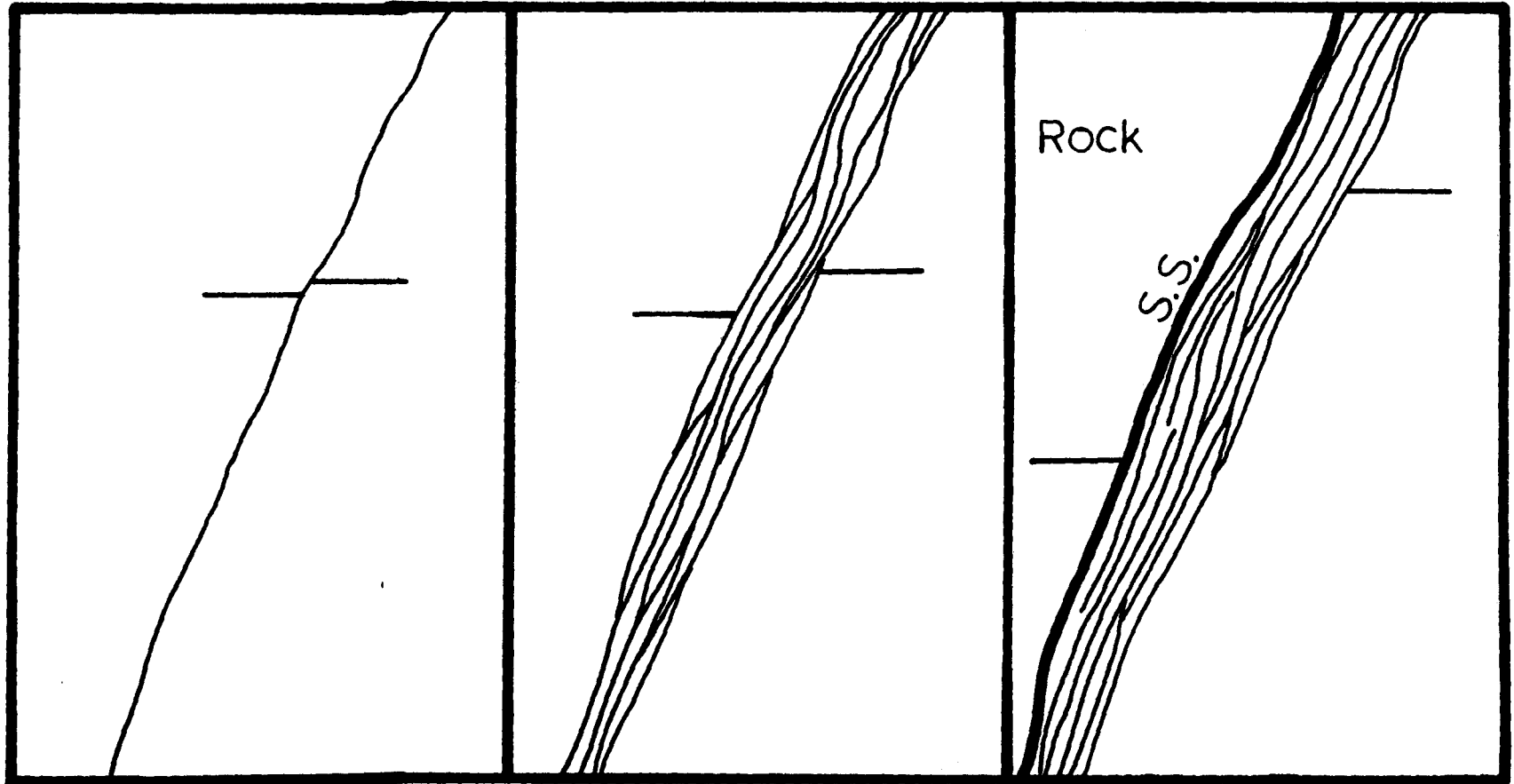
5.2 Faulting

The initial movement on a newly developed fault surface can be simulated when bare rock faces are placed together and subjected to increasing normal stress (triaxial loading experiments). Three stages of sliding behaviour (Brace and Byerlee, 1966; Scholz et al., 1972; Byerlee and Summers, 1976) occurred during these experiments:

Firstly, the specimen is deformed by stable sliding (uninterrupted continuous movement), followed by episodic stable sliding, and then finally stick-slip occurred (rock surfaces suddenly slide forward). If loading is initiated again, another stick-slip episode might occur (this type of

Figure 5.1. Chronological development of a slip surface from deformation bands.

Displacement increasing →



Deformation band

Zone of Deformation bands

Zone of Deformation bands with a slip surface

stick-slip cyclicity is known to occur on natural faults).

In triaxial loading experiments the stable sliding episode is accounted for by "asperity climb" (Reeves, 1985). At low normal stress the surfaces move relatively by riding over the interlocked asperities. At higher normal stress, however, the asperity contacts increase as the surfaces move closer to one another (the coefficient of static friction increases while the coefficient of sliding friction remains constant). This sets up a stick-slip instability and, eventually with increasing shear force over time, the strength of the asperities will be exceeded and brittle failure will occur. The initial onset of brittle failure accounts for episodic stable sliding which occurs just before the shear strength of the sliding surface is surpassed and major sliding occurs as the surfaces shear through the fracture's asperities.

With the breaking apart of asperities on the faulting surface, a layer of finely crushed material, gouge, is produced. As gouge is found on most mature fault surfaces, these triaxial loading experiments should represent a close approximation of the actual faulting mechanism.

In samples with a layer of fault gouge between the surfaces Engelder (1974) noted the same stable sliding to stick-slip transition. During stable sliding the rock specimen rode on a layer of gouge flowing internally by pervasive cataclasis. No sliding surface has been developed at this stage, the movement of the surfaces was facilitated by grains moving past one another and breaking up (many grains develop microfractures within them rather than break up during rigid body rotations, which form essentially as extension fractures parallel to σ_1 at some acute angle ($\approx 35-45^\circ$) to the shear direction).

Stick-slip occurred along the gouge/wall-rock interface when granulation and compaction of the gouge had reached a maximum. In some cases (Jackson and Dunn, 1974; Shimamoto and Logan, 1981), the gouge approached a state in which it behaved almost like an intact rock.

From the onset of stable sliding to the stick-slip episode which results in an earthquake, a great amount of energy is dissipated. Most of the energy in stable sliding is used for cataclastic break up of gouge, while the energy dissipated during stick-slip occurs in the form of frictional heat and acoustic emissions.

Chapter 6: ESR Dating of Faults

6.1 A Review of Previous Work

The ESR method of dating fault gouge was first attempted by Ikeya et al. (1982) and Miki and Ikeya (1982). While deriving ages from ESR signals (E') in quartz from natural fault gouge, it was noticed that AD values increased further away from the fault zone until a maximum AD value was obtained. They assumed that the paramagnetic centers in quartz are annihilated by some mechanism on the fault plane during fault movement. It was proposed that high shearing stress and temperature (two processes known to decrease a paramagnetic center) are responsible for the annihilation of these defects.

They did not, however, clarify the process of the frictional heating mechanism on the fault. It was only stated that since there are localized instances of melting on the fault plane, the temperatures required to zero ESR signals must be present. These localized evidences of melting do not necessarily prove that such high temperatures had radiated throughout the entire fault zone. Heat flux in a brecciated fault system would be enhanced, and therefore temperatures would decrease rapidly away from these hot spots of melting.

Their evidence of decreasing E' signal intensity with the increased degree of deformation of grains suggests a more likely mechanism for the zeroing process in quartz from fault gouge. They attribute mechanical zeroing to the movement of dislocations in crystals during fracturing and plastic deformation. Electrons trapped at the defects are released at dislocations and recombine with holes accompanying deformation luminescence.

Ikeya et al. (1983) used ESR dating on faults at Rokko and Atotsugawa Japan (two faults active in the Quaternary). The ESR ages obtained were consistent with estimates based on geological observations of sediment offsets in the area. To prepare samples for this dating attempt, it was necessary to crush the fault gouge by hand which will alter the ESR signals in the outer grain portions. Their solution was to etch the grains in HF to remove the outer portion of the grains that were altered during crushing. Although they reported a 10-20% variation in the signal intensity due to this procedure, they chose to ignore the effect which they claim does not significantly alter ESR ages for fault gouge. The fact is that etching does not preferentially remove only the outer portions of the grains. The HF will tunnel through cracks and depressions in the quartz grain, removing inner portions while leaving the outer, altered portion intact. This procedure probably resulted in an under-estimation of the ages they obtained.

The attempts to use ESR to date faults described thus far, served to introduce the technique as a new dating method for tectonic movement. What was subsequently needed was further study to develop a criterion that shows that the dates obtained actually represent fault movements at which time the signals were totally zeroed.

Zhuo-ran et al. (1985) found that the E' and Ge centers in quartz gave distinctively different AD results. The E' centers consistently gave larger AD values than the Ge centers. From these results it was concluded that zeroing of the Ge center occurred during recent fault movement whereas the zeroing of the E' center occurred during the fault initiation. If it were true that the E' center had not been affected by the later movement (which caused zeroing of the Ge center) the centers should have different sensitivities to stress. This was not discussed.

The same authors report that the Ge center is sensitive to light exposure and therefore they took precautions to shield the samples from light exposure. However, it is probable that the Ge signal was not shielded 100% from light exposure and may have been depleted slightly. They do not discuss this possibility.

Fukuchi et al. (1985) used multicenters in quartz (OH, Al, Ge, and E') to date faults in the South Fossa Magna Japan. The AD's of the centers are concordant, which indicated to them

complete resetting of all signals at the time of faulting. This was the first attempt to establish that ages obtained actually do represent an actual faulting event in which zeroing had occurred. They also showed that different centers are zeroed to different extent in samples that have discordant AD values. From their data, the OH and Ge intensities were less affected (more stable) than the Al and E' centers.

While the different stress sensitivities in ESR centers reported by Fukuchi et al. (1985) is probable, they did not proceed to confirm that the ordering of sensitivities for the different centers is present in other samples with discordant AD values. This may be the result of the different saturation limits of the ESR centers which had not been considered for any of the fault dating attempts in the above studies.

Toyokama et al. (1985) applied a saturation curve fit to the growth points for the E' center from the Rokko fault. These ESR ages obtained were reported to agree well with geological field evidence, but were slightly lower than the ages obtained by Ikeya et al. (1983) using extrapolation of only the linear portion of the growth curve.

Tanaka and Shidahara (1985) reported a higher stress sensitivity of the OH center over the E' center in experimentally crushed quartz (contrary to the stress sensitivities that were

reported by Fukuchi et al. (1985) for natural fault gouge). There was a grain size effect for the decrease of ESR intensities, such that the larger grain sizes were found to be more sensitive to stress than the smaller grain sizes. Tanaka and Shidahara (1985) did not, however, confirm that AD values followed the same decreasing trend in larger grains.

Ariyama (1985) used a rotating grinding apparatus (which simulated fault movement) in which was placed a mixture of quartz and kaolinite (wetted). This was an important experiment because it showed that ESR signals can be totally reset on a fault if the right conditions are present. The empirical values of at least 20 bar of confining stress and 50 cm of displacement for complete resetting should not be taken as literal boundary conditions of resetting as experimental conditions can not possibly define the true processes acting on a real fault.

Kosaka and Sawada (1985) obtained different ages for thin films of fault gouge collected at different locations in the Tsurukama fault zone. This study revealed that there are subzones of fault gouge that are affected to a different extent, and at different times during the history of activity in the fault zone. The different ages obtained from these samples led to a chronological interpretation of sequential build up of fault gouge outward from the fault surface.

Fukuchi et al. (1986) performed grinding experiments on quartz and determined that preferential resetting of intensity in centers proceeded in the order OH, Al, Ge to E' (E' being the most sensitive). In this study, in contrast to Tanaka and Shidahara (1985), it was found that smaller grain sizes are more sensitive to stress.

The preferential resetting of centers, again, was not confirmed for AD values which would have likely yielded different results because a decrease in ESR intensity is not strictly reflected in the change in the values of AD.

For all of the attempts to date fault gouge that were discussed above, secular equilibrium of the radioactive decay series was assumed. This, as discussed later, may not and is probably not the case.

Therefore, there are still many uncertainties for ESR dating of fault gouge that must be resolved in order to provide accurate estimates of fault movement ages. It is imperative, at this point, to determine whether zeroing on a fault has actually taken place because an age obtained for fault movement by ESR dating is of no value, unless it can be shown that this date represents total resetting at the time of fault activity.

A criterion for the determination of total resetting of a sample of fault gouge is proposed here.

6.2 Theory of ESR Dating of Fault Gouge

6.2.1 General Concept

ESR ages of quartz in fault gouge can be derived using the equation shown on page 9 once the AD in the sample and the DR received by the sample is known. However, accurate determination of these quantities from samples of fault gouge is not a simple procedure and has to be quantified before ages can be determined. First of all, the accumulation of trapped charge is non-uniform. Larger sized grains have more paramagnetic centers in their volume than do smaller grains. Therefore the same dose rate will produce more paramagnetic centers in larger grains and therefore the AD's will differ for different grain sizes. This effect is mostly due to the α - and β - radiation within the quartz grains. The α -particles will penetrate a larger volume of material and β -particles will be backscattered more in larger grains and thus induce more paramagnetic trapping centers in larger grains. Therefore the α and β contributions to the DR in the sample will be greater for larger grains. If the variation of AD and DR values are proportional for different grain sizes, then, it is possible to calculate concordant ages for the different sized grains if they were concordant in age originally. This grain size variation is accounted for in the α and β attenuation factors for the determination of DR in equation 2.1.

ESR dating of quartz fault gouge can only be performed for samples younger than the mean-life of the paramagnetic centers at ambient temperatures (25°C). This is the average residence time of a trapped charge for a particular center. Samples older than the residence time of the ESR centers will not give reliable ages as charges will begin to de-trap or fade, thus decreasing the true AD of the sample. The mean-life of trapping centers at ambient temperatures have been determined by various authors and are show on page 36. From the mean-life time shown it appears that samples up to 10^9 a could be dated. However, an estimation of the average AD required for saturation of the traps (2000Gy) to occur divided by the average DR in a fault zone ($4.0 \cdot 10^{-3}$ Gy/a) shows that the maximum obtainable age is approximately 500,000a for samples that have remained at approximately 25°C for their lifetime. Samples that have come from depth (where temperatures are greater) and subsequently been tectonically uplifted will have centers with a shorter lifetime. The maximum temperatures experienced by the gouge may be estimated by oxygen isotope compositions of authigenic clay and carbonate minerals (Longstaffe, 1986). Diagenetic minerals correspond to different crystallization temperatures from brackish water and therefore the types of diagenetic minerals present in the gouge should reveal the temperatures it experienced while still buried.

6.2.2 The Plateau Method for ESR Dating of Fault Gouge

For quartz in old, undisturbed rocks (such as granites, sedimentary wall rocks of a pre-fault surface, or inactive faults) there is the possibility that the ESR centers could be at or close to a steady state value such that the rate of trapping of charges is equal to the rate of recombination of holes and electrons; note that this steady state level increases as the ambient temperature decreases due to the increasing lifetime of trapped charges. Consider a series of analyses of varying grain size fractions of a particular sample (Figure 6.1a). ESR age calculations on such samples would yield a plateau of equal ages. This is the maximum age or steady-state age that will be obtained from the sample (Figure 6.1a).

As discussed above, when exposed to stress, the paramagnetic centers in quartz can be emptied, causing a decrease in ESR intensities and subsequent AD values derived from them. An increased sensitivity to stress for smaller grains (as discussed by Fukuchi et al., 1986), would lead to a theoretical minimum AD value for an ESR center for a sample exposed to sufficiently intense stress. This represents complete resetting or deletion of the traps (signals not totally destroyed, but decreased to an "effective minimum" which can not be discerned from the background noise in the spectra). This would therefore lead to the establishment of a "plateau" of equal AD/age values for

grains smaller than a particular size (critical radius r_c), if total resetting has indeed occurred (Figure 6.1b).

Therefore, the complete zeroing for a center would be evident in the establishment of an equal AD/age plateau of zero age below some critical grain size (r_c) (r_c is purely arbitrary and will depend on the magnitude of stress on a fault gouge system). Grain sizes above this r_c value do not have their ESR signals completely zeroed and will give an AD value that does not represent total zeroing (Figure 6.1b).

After fault movement has occurred, the paramagnetic charge in the quartz grains will increasingly accumulate, although not at the same rate since charge buildup per unit time is not uniform for different grain sizes. Therefore, there may not be a developed AD plateau for the range of grain sizes ($r < r_c$) that were totally zeroed at the time of faulting (larger grains will accumulate charge at a faster rate than smaller grains). This is however, accounted for in the ESR age calculation and therefore there will be an increase in age at a constant rate for the different sized quartz grains. On a plot of ESR age vs. grain size, the plateau will be translated upwards while preserving its original flat profile. Grains larger than r_c will continue to plot above the plateau (Figure 6.1c). The time of last movement should only be "read" from the plateau; any other grain sizes provide an upper limit to the age.

For different ESR centers with different stress sensitivities, there should be a convergence of the ages for the smallest grain sizes to the same plateau value (Figure 6.2). In this instance only, could congruent age values for various centers be said to represent a fault event in which total resetting had occurred.

Samples that do not show a plateau development are assumed not to have been zeroed within a few lifetimes of the trapped charges. Grain sizes that give AD values larger than an established AD plateau for the most stress sensitive center of a sample are also assumed to be non-zeroed and therefore should not be used for determining an age.

6.3 Experimental Goal

It is necessary to determine the most stress sensitive ESR center in quartz, which should show the occurrence, most often, of AD/Age plateau development in fault gouge and test whether plateau development occurs in real fault gouge.

- Figure 6.1. a). Before faulting occurs, the ages obtained for all grain sizes may give a maximum value approaching the saturation curve.
- b). immediately after fault activity ($t=0$) grains smaller than some critical size (r_c) will give an age representing total zeroing.
- c). AD should accumulate in the grains after faulting and the age plateau will persist for the totally zeroed grains.

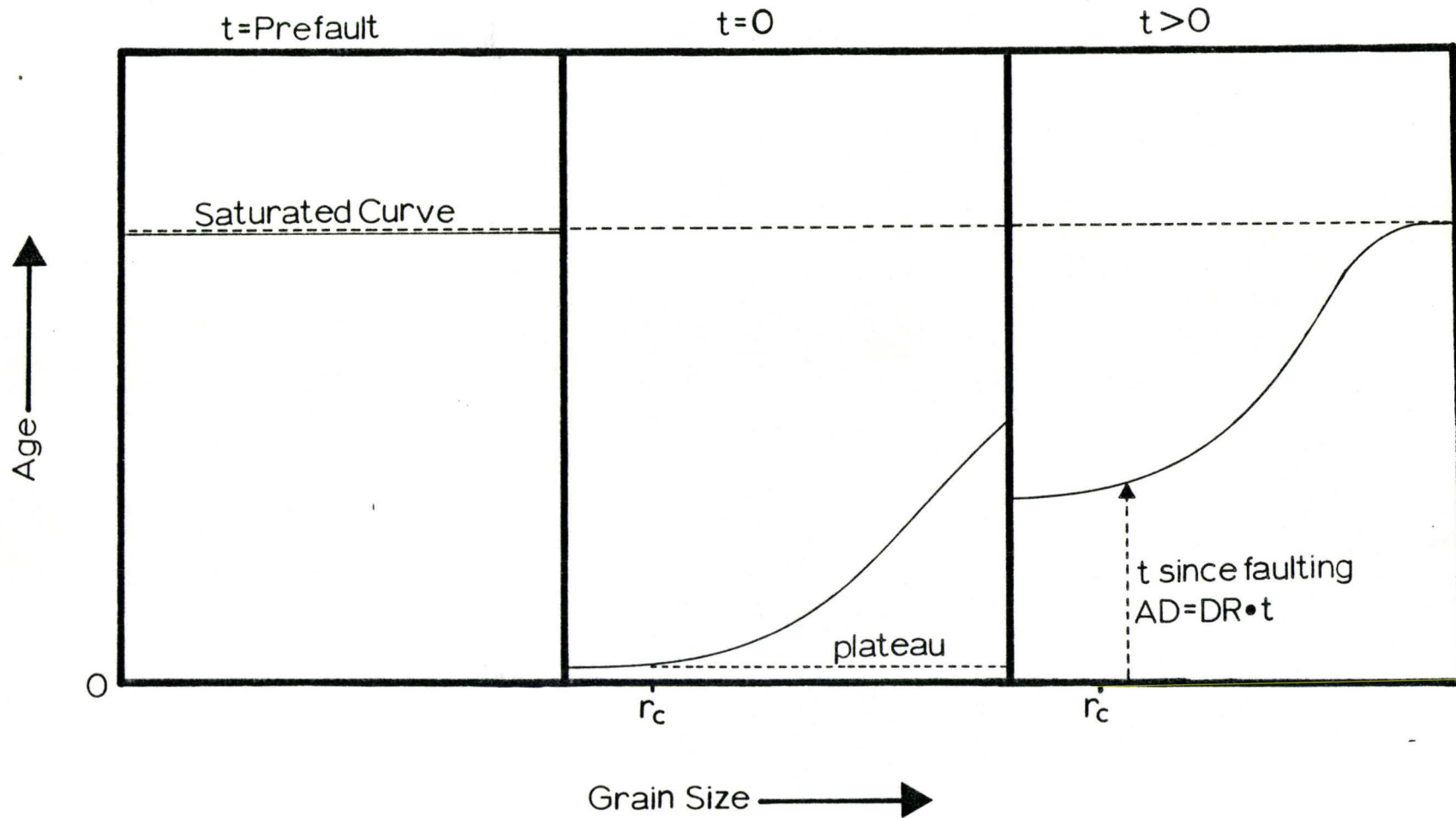
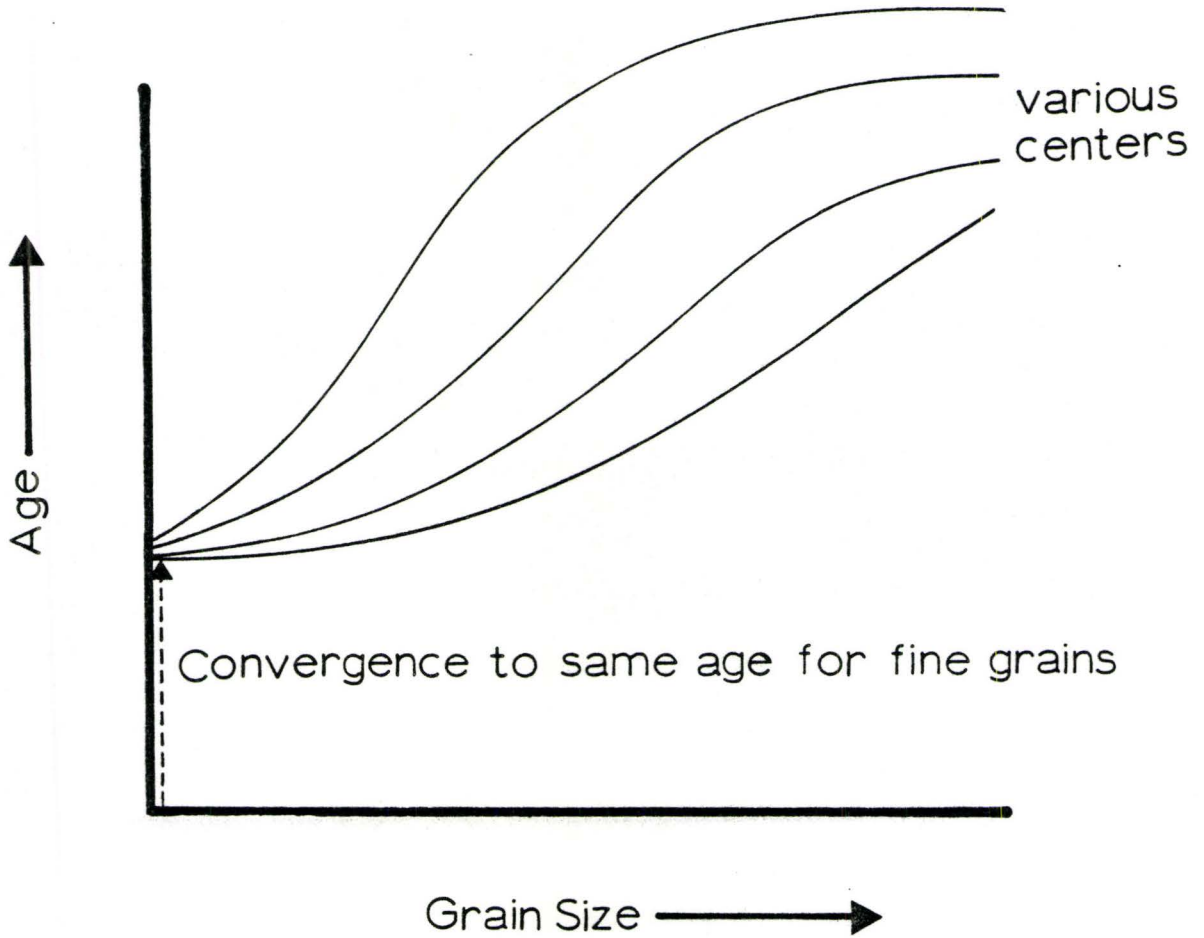


Figure 6.2. Convergence of ages for smallest grain sizes for centers with different stress sensitivities. Ages for centers with lower stress sensitivities will converge on a plateau of the center that has the highest sensitivity to stress.



Chapter 7: Experimental Methods

7.1 Sample Preparation

The majority of the samples used were obtained in a disaggregated form and therefore crushing was not needed. If crushing of the sample is necessary it should be done lightly by hand, using a mortar and pestle. After crushing the quartz must be washed in a concentrated hydrofluoric (HF) acid bath for approximately 1 hr to remove the surface defects created during crushing.

Disaggregated samples were washed in concentrated HCl (12 M) for one hour to dissolve any carbonate matrix. The residue was attacked with fluoboric acid (HBF_4 , 1 M) at 30°C for two hours in order to dissolve feldspar. After washing with distilled water and drying for 24 hours, the non-magnetic fraction of the sample (principally quartz) was separated using a Frantz isodynamic separator. Grains other than quartz were removed by handpicking under a binocular microscope.

The quartz samples were sieved to separate grain sizes between $80\text{-}190\mu\text{m}$. Grain sizes greater than $250\mu\text{m}$ should not be used because of anisotropy effects during ESR measurement (Regulla et al., 1985). For sizes less than $80\mu\text{m}$ the proportion of the grain penetrated by α - particles increases to an extent that accurate correction factors for the α - dose

become difficult to estimate.

Etching of the total sample in concentrated HF for approximately 30-60 minutes will effectively reduce to negligible the alpha-dosage to the quartz since α -rays only penetrate the outer grain layers (Fleming, 1970; Bell and Zimmerman, 1978). Removing 20 μm of the outer layer of quartz will reduce the α -dose by 95%. Although this procedure is effective for removing paramagnetic centers produced by α -particles, HF tends to attack the surface of grains inhomogeneously. Therefore, instead of etching, an α -attenuation correction factor is used in the age calculation. The correction factor is integrated over a spherical volume (quartz grains treated as spherical in shape) using the correction factors from Bell (1980).

7.2 Irradiation

Seven to eight aliquots (≈ 200 mg), of each grain size were weighed. It is important to have a uniform weight distribution within $\pm 8\%$ for all of the aliquots used to ensure minimal variation of intensity in the ESR spectrum. All but one aliquot (natural sample) were irradiated with a ^{60}Co -source located in a hot cell at the McMaster Nuclear Reactor. The samples were placed in a semi-circle around the source, held in a wooden sample holder at equal distances from the source. The dose rate received from the samples around the

source was approximately 5.028 Gy/min. Dose was controlled by exposure time rather than by distance from the source as it is an easier procedure to place the aliquots the same distance from the source and calculate the dose rate received by the aliquot of sample from the length of exposure. Using the varied distances from the source, it is difficult to place the aliquots of different samples in exactly the same positions as the other irradiation runs and therefore the dose rate must be measured at each aliquot distance from the source every time an irradiation run is performed. The fault gouge quartz samples were exposed to the source in 4mm diameter pyrex glass tubes with 0.9mm thick walls for times between 4 and 100 min. to give doses between 20-1000 \pm 10% Gy. The \pm 10% error in dose received (due to a slight variation in the mass of some of the ^{60}Co rods within the hot cell) is measured by a dosimeter at various positions around the sample holder.

7.3 Measurement of ESR Spectra

The ESR spectrometer used for this study is a Bruker ER100D spectrometer with a TE4101 cavity, located in the Chemistry Department at McMaster University.

The sample is placed in a quartz tube which is inserted into the resonant cavity and secured, ensuring that the quartz tube is positioned the same way for each sample. A 9mm outer diameter quartz tube with 1.9mm thick walls is used for room

temperature measurements to enhance the signal strength. For low temperature measurements the sample tube is placed into a low temperature quartz dewar with an inner diameter of 5mm. Therefore a quartz tube with a 4mm outer diameter and 0.4mm thick walls was used.

The OH, Ge, and E_1' signals (at g-values 2.010, 1.996, and 2.001, respectively) were obtained at room temperature (≈ 300 K). For these centers the best instrumental settings were found to be: magnetic field of 3420 Gauss (G); microwave power 2mW; modulation amplitude 1.0 Gpp; Sweep width 100G; sweep time 500s; time constant 200 ms. Since the E_1' -center begins to saturate even at low microwave power (see Figure 4.2, right, lower spectra) it was recorded at 0.6 mW. The procedure for measuring the intensities of these spectra is explained in Figure 7.1. Once the signal has been identified through its g-value, then a direct measurement of the signal amplitude using an arbitrary scale (millimeters for this study) is taken to represent the ESR intensity. The intensity measurements for each irradiated aliquot will therefore define the growth curve from which an AD can be determined.

The Al and Ti spectra (Figure 4.2, left) can only be recorded at lower temperatures. The lowest temperature obtainable on the ESR spectrometer at McMaster using the maximum flow of nitrogen vapour (boiling temperature of 77K)

varies between 102 and 107K (105K was the most frequent stabilizing temperature reached during low T measurements). At these temperatures the hyperfine and superhyperfine splittings of the Al and Ti spectra are readily visible. The resolution of splittings can be increased by using a liquid nitrogen dewar (where the sample tube is placed directly into liquid N₂) to lower the temperature even further, but increased noise incorporated into the ESR spectrum caused by bubble action in the liquid N₂ makes this a fruitless step (increased noise may obscure peak heights thus lowering the accuracy of intensity measurements).

Since both centers show hyperfine and superhyperfine splitting they are found spread out over a range of g-values (Al-center: $g=2.017$ to 1.985 ; Ti center: $g=1.984$ to 1.915). Figure 7.2 shows that measurements of the individual lines of the Al and Ti centers from San Andreas Fault gouge (1-14 for Al-center, and 1-6 for Ti-center see Figure 4.2) gave the same AD value, within the $\pm 10\%$ reproducibility, as measurement of the Al (from the top of line 1 to the bottom of line 14) and Ti (top of line 1 to the bottom of line 6) spectra as a whole (except for the no.10 line of the Al spectra which may be interfered with by a Fe³⁺ line; McMorris, 1971; see Figure 7.2). Yokoyama et al. (1985) suggested that line 12 (their line no.14) of the Al spectra may be disturbed by a Ge-line at $g=1.996$.

Figure 7.1. The procedure for ESR intensity measurement.

"I" shows the intensity measured for each spectrum.

OH

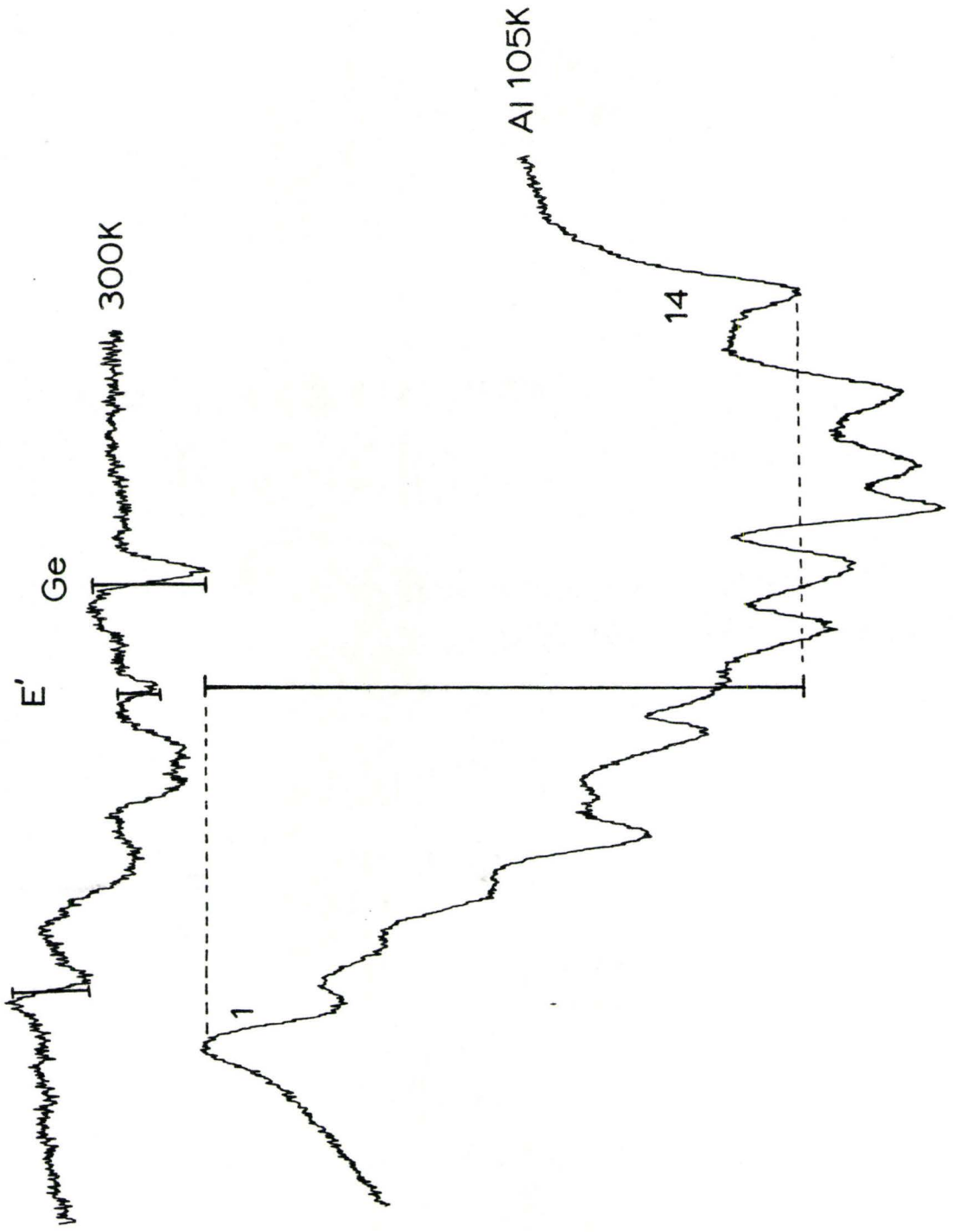
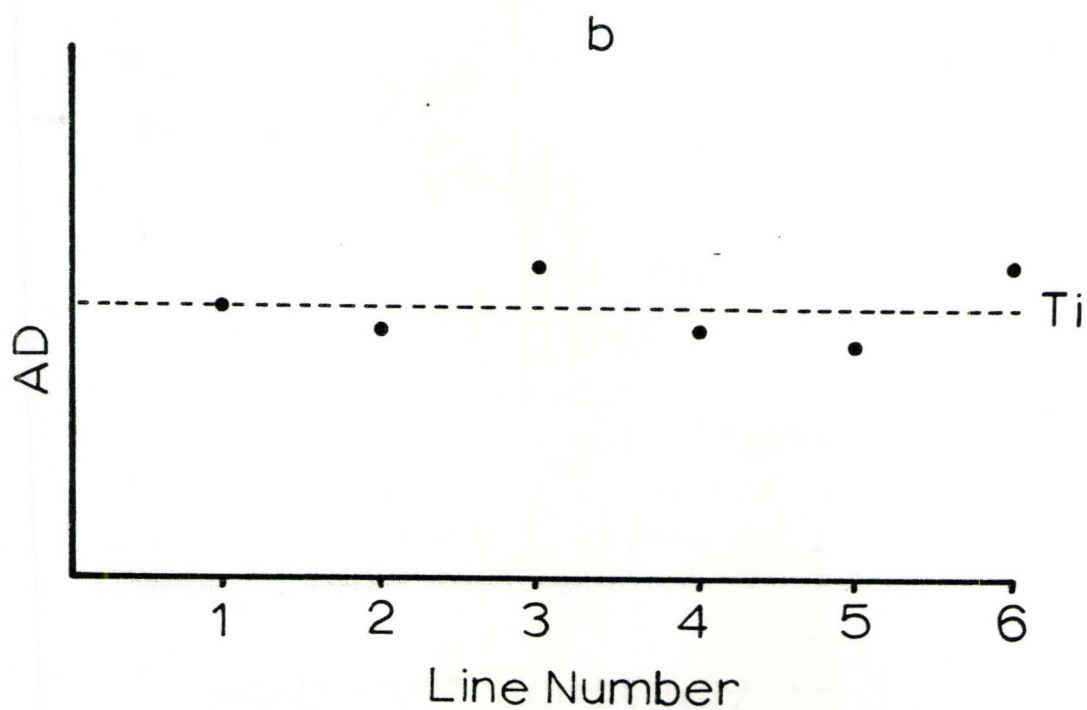
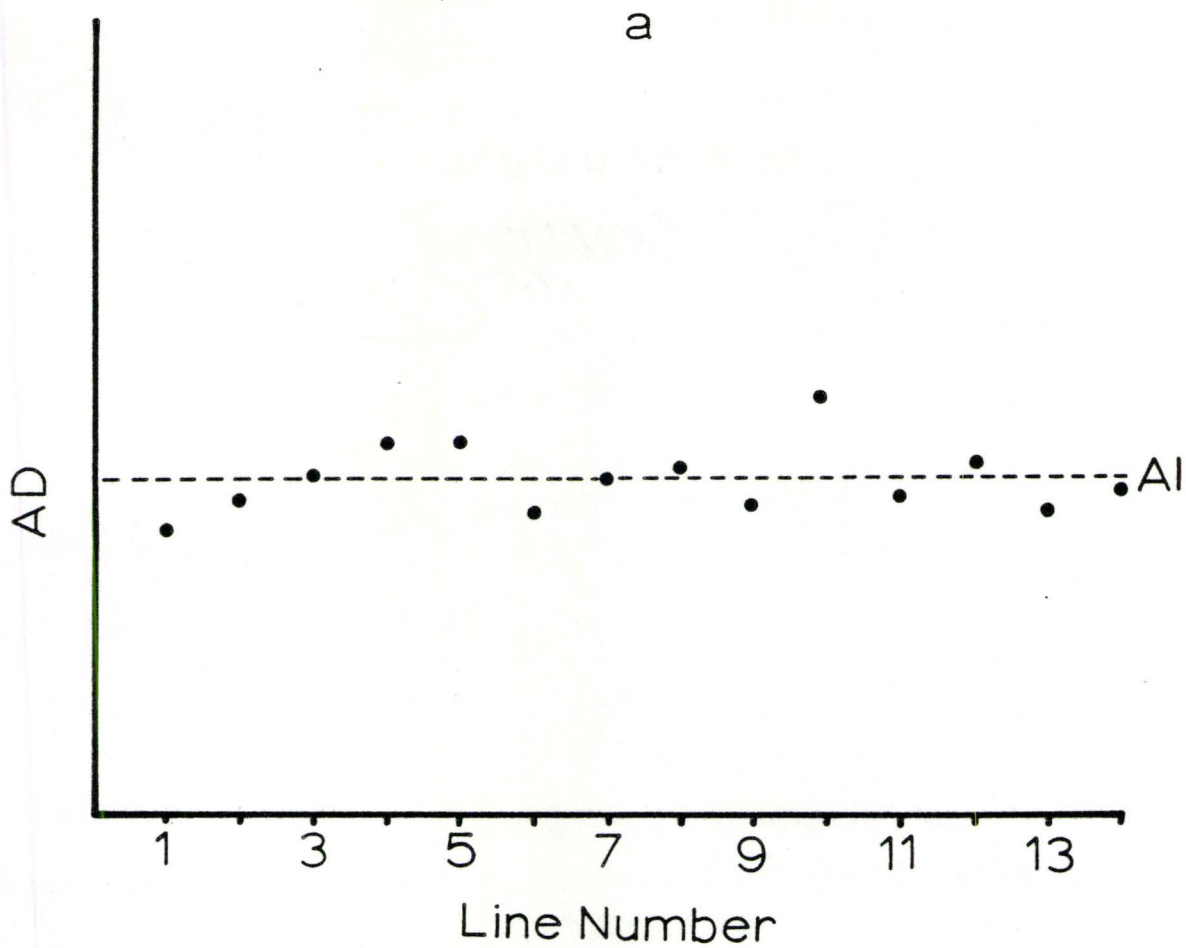


Figure 7.2. AD vs. The line number for the a) Al, and the b) Ti spectra. The dashed line indicates the AD value of the center measured as a whole.

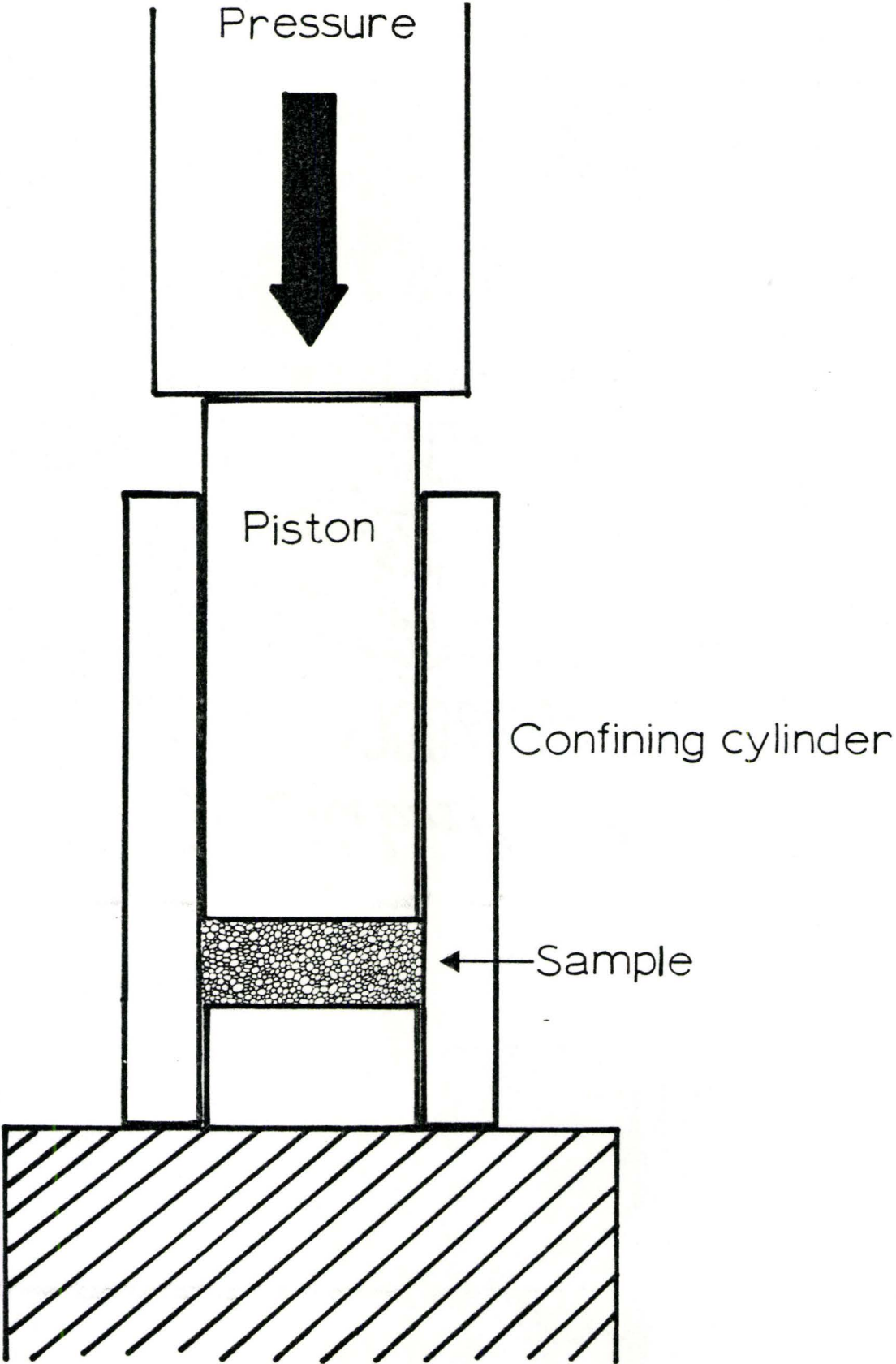


Although the AD value of line 12 did not deviate substantially from the other lines, it is recommended that line 12 not be used for intensity measurement. Measurement of the Al and Ti spectrum was as follows: Al intensity was measured from the highest point of line 1 to the lowest point of line 14; Ti intensity was measured from the highest point on line 1 to the lowest point on line 6 (see Figure 7.1). In some instances line 1 for the Ti center is not well defined and it is necessary to measure from line 2 to 6. Instrumental settings for the Al and Ti centers were the same as for the room temperature spectra except for the magnetic field of 3370 G for the Al center and 3470 for the Ti center. The sweep width used for the Ti center was 200 G.

7.4 Fault Simulation Experiment

The San Jacinto quartz grains with a size distribution between 60-300 μ m were split into three identical samples (\approx 40g each). Two of the samples were heated to 550°C for 23 hours, after which the ESR signals had been completely annealed. After exposure to a 500Gy γ -dose from a ^{60}Co source (5.028 Gy/min), the weights of individual grain sizes for both samples were measured in order that a comparison could be made of grain size distributions before and after deformation of the sample. The samples were then deformed under uniaxial compression using a Buehler specimen mount hydraulic piston

Figure 7.3. Hydraulic Press diagram



press (see figure 7.3) with load pressures of 29 and 60 MPa, respectively (applied pressure was determined by an external pressure gauge and constantly maintained for approximately 30 seconds). The sample of quartz grains was placed in a metal cylinder on top of a removable metal plug that fit snugly into the cylinder. Another metal piston was then placed into the metal cylinder over top of the sample of quartz grains. Then the confining cylinder holding the sample between metal plug and piston was placed into the hydraulic apparatus in such a way that direct pressure would be concentrated on the plug and piston with the sample between them, not on the surrounding cylinder. Once the cylinder was firmly secured in the apparatus, pressure was increased by manually pumping until the desired pressure was reached (see Figure 7.3).

The samples were dry sieved and the individual weights of each grain size of the samples that underwent uniaxial compression were then measured. The plot of cumulative weight percent vs. grain size for the samples before and after compression is shown in figure 8.3.

The third (non-compressed) sample was used to study the natural ESR signals in various size fractions of the gouge.

The three samples were then dry sieved to different grain sizes between 80-190 μm which were divided into aliquots for

irradiation (described in section 7.2). AD's were then determined for each grain size for each of the three samples using growth curves defined by the additive dose method (described in section 2.1).

7.5 Bleaching Experiment

Bleaching experiments were performed on sized quartz samples (San Jacinto samples) that had been given artificial doses of radiation; 1000 Gy (so that all aliquots start with the same center intensities), to test whether the ESR signals deplete in intensity when exposed to light during sample preparation. Bleaching of the ESR signals was tested for in natural and high intensity UV light:

- 1) samples were first exposed (up to 36 hours) to a Hg UV lamp radiating 50 mW/cm^2 focused on the cavity of the ESR spectrometer while the sample was held in a 9mm outer diameter quartz tube in the cavity; the sample was shielded from external light with aluminum foil and not disturbed during irradiation.

- 2) Also a thin layer of quartz, approximately 1 grain thick (0.5-0.7 grams spread as evenly as possible in a 10mm diameter plastic petri dish) was exposed to successive 60 minute intervals of the Hg UV lamp reflected at a 45° angle directly down on to the sample; the sample was placed in an aluminum covered cardboard box which shielded it from outside light; UV light entered through an aperture at one end of the

box and is reflected directly down onto the sample by an aluminum foil covered piece of cardboard at a 45° angle; transfer of the samples in and out of the UV box is performed in low intensity red light; ESR spectra were recorded after each successive 60 minute exposure.

3) Two other sets of samples in petri dishes were exposed to natural sunlight: for 16h in direct sunlight, and for 20h in diffuse sun light (clouded sky conditions) for successive 2 hour intervals, after which the samples were shielded from further exposure to sunlight by wrapping them in aluminum foil. Preparation for measurement of the ESR spectra was done using low intensity red light. Care must be taken not to expose the samples to undue light when transferring the samples from their holders to the quartz tube for ESR spectra recordings.

Chapter 8: Results of Experimental Studies

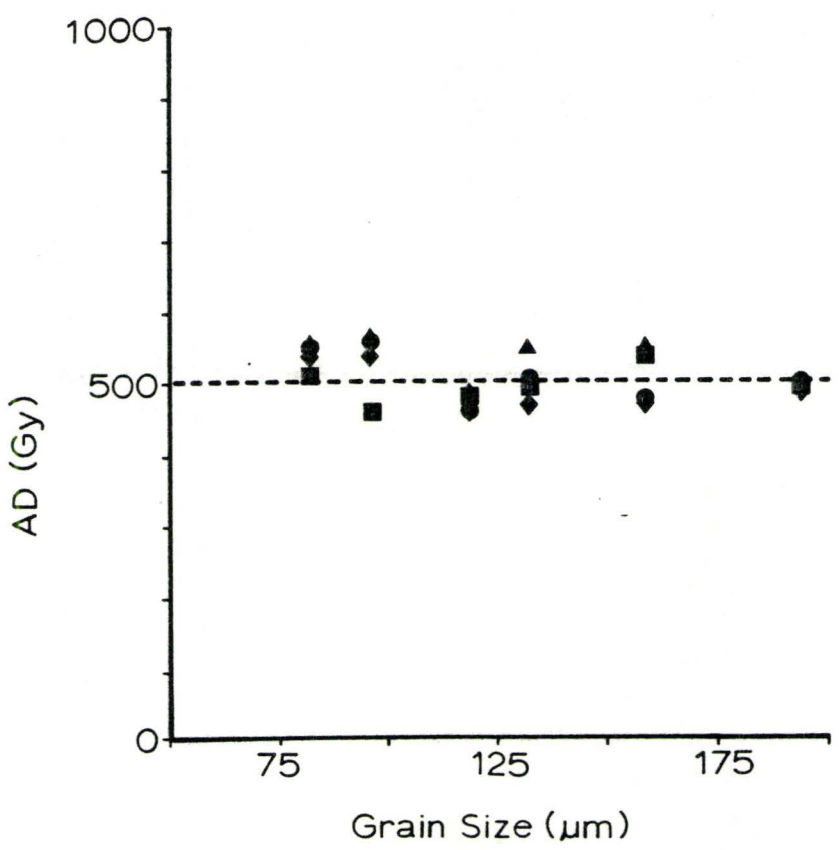
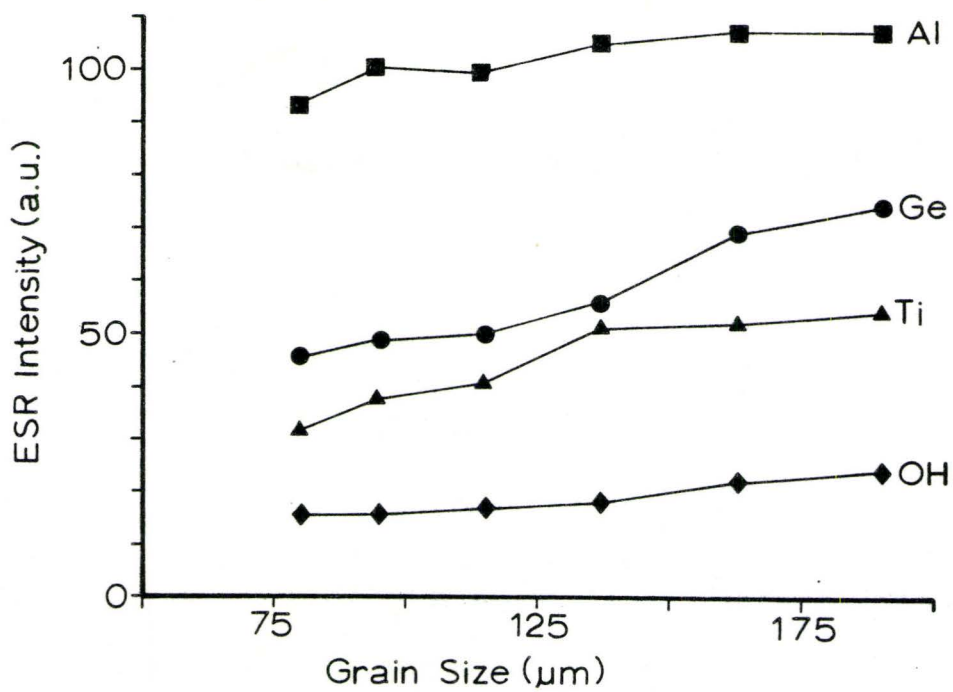
8.1 Effect of Grain Size on ESR Intensity and Dose

ESR intensities were found to vary with grain size of samples with the same AD which is due to different packing of the grains in the cavity (Figure 8.1). It could therefore be argued that the inherent decrease in ESR intensity after grinding experiments performed by Fukuchi et al. (1986) may not be totally a result of cataclasis. Figure 8.1 shows that the grain size effect for intensity decrease progresses in the order: (smallest decrease) OH (10% variance between 80-190 μm); Al (15% variance between 80-190 μm), and Ge (35% variance between 80-190 μm) centers. This is the same sequence for the magnitude of intensity decrease as a result of grinding as shown by Fukuchi et al. (1986). In order to prove that grinding does cause ESR intensity decrease, and overcome this intensity variance with grain size, AD determinations for individual grain sizes must be obtained. As will be shown below, the OH signal in fact shows the greatest grain-size dependence of AD.

Quartz which had been annealed, and then given a uniform 500 Gy dose, yields a highly reproducible AD (± 50 Gy maximum error) as measured by the additive dose method; note that this shows the precision of AD determination; the accuracy depends on the calibration of the gamma source. Therefore, AD's should

Figure 8.1. ESR intensity vs. grain size for the San Jacinto sample. The increase of ESR intensity with grain size is probably due to different packing of the grains in the cavity.

Figure 8.2. AD determination for a totally annealed bulk sample (San Jacinto) irradiated with 500 Gy. (Symbols are the same as on Figure 8.1)



■ Al ▲ Ti ● Ge ◆ OH

be determinable to a precision of $\pm 10\%$ (Figure 8.2).

8.2 Results of the Compression Experiment

Figure 8.3 shows the effects of mechanical deformation on particle size distribution. Deformation of the quartz samples by 29 MPa of pressure caused no cataclastic breaking of grains and the cumulative percent curve of grains is essentially unchanged after deformation (Figure 8.3a); 60 MPa pressure, however, caused significant cataclasis, as evidenced by the frequency curve being skewed more to finer grain sizes, and decreasing in the frequency of larger grain sizes (Figure 8.3b).

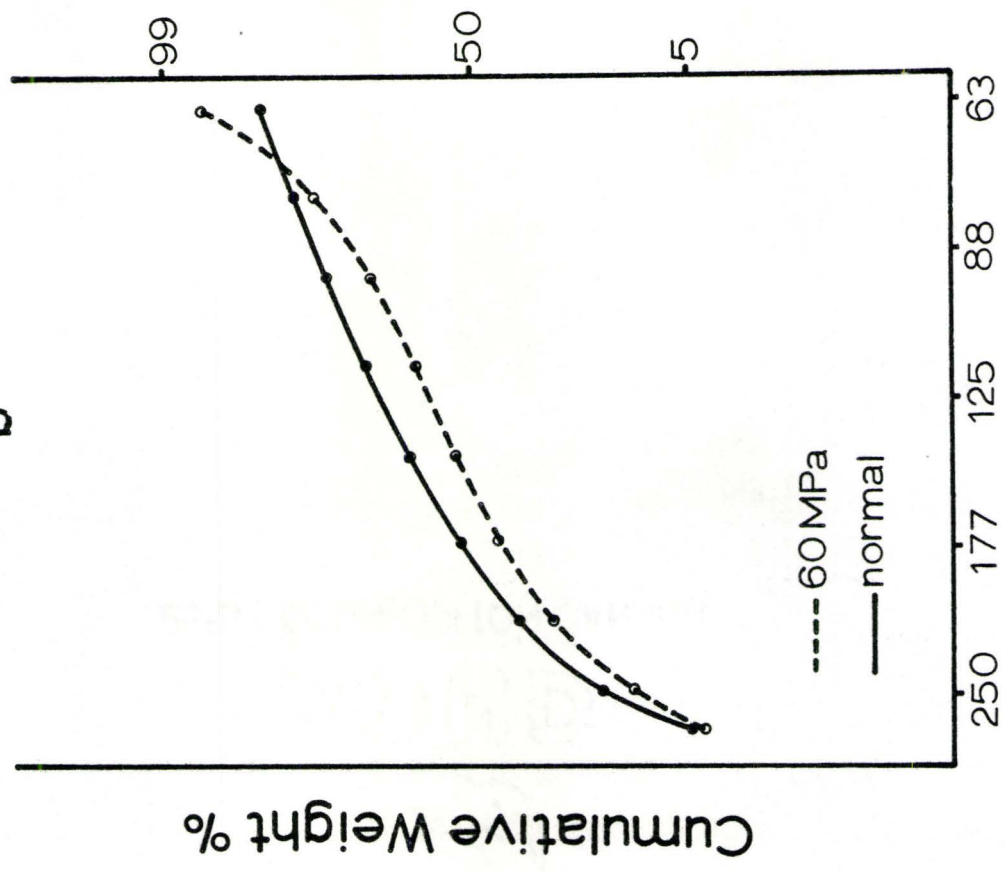
After compression, the AD values of all of the ESR centers in quartz changed significantly, however, not to the same extent (Figure 8.4). The OH center was reset most, followed by the Al and Ti centers, respectively. The AD of the Ge center actually increased after compression. The E'_1 center was not found in this sample. The degree of resetting increased with increasing stress, from 29 MPa (mostly elastic deformation), to 60 MPa (brittle deformation). The AD of the Ge center increased with increasing stress. A grain size trend for the degree of resetting is not intrinsically apparent in Figure 8.4 when error bar overlap for each data point is considered. Therefore a chi-square test was performed to

Figure 8.3. Cumulative weight % vs. grain size for an artificially crushed sample of San Jacinto fault gouge.

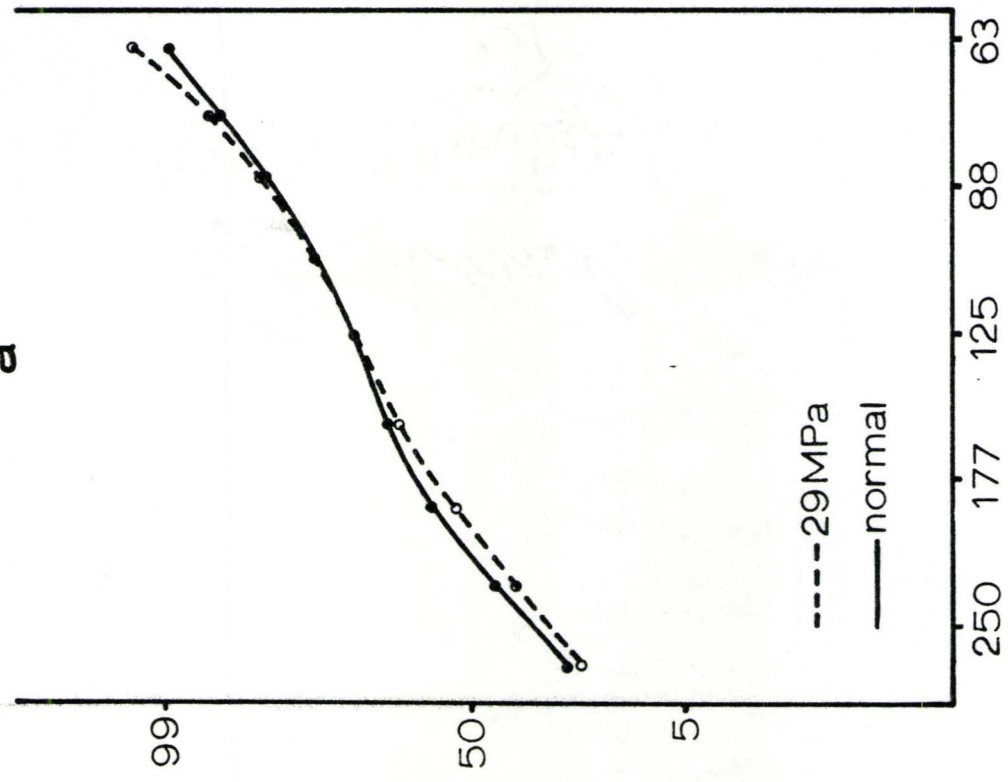
- a) Grain size distribution of the sample after 29 MPa hydrostatic pressure is virtually unchanged from the normal undeformed sample
- b) pressure of 60 MPa causes a depletion of larger grain sizes and an increase in finer grain sizes due to fracturing.

note: Normal = unstressed sample of fault gouge.

b



a



Grain Size (μm)-Log Scale

Figure 8.4. AD resetting by hydrostatic pressure (sample originally irradiated with 500 Gy)

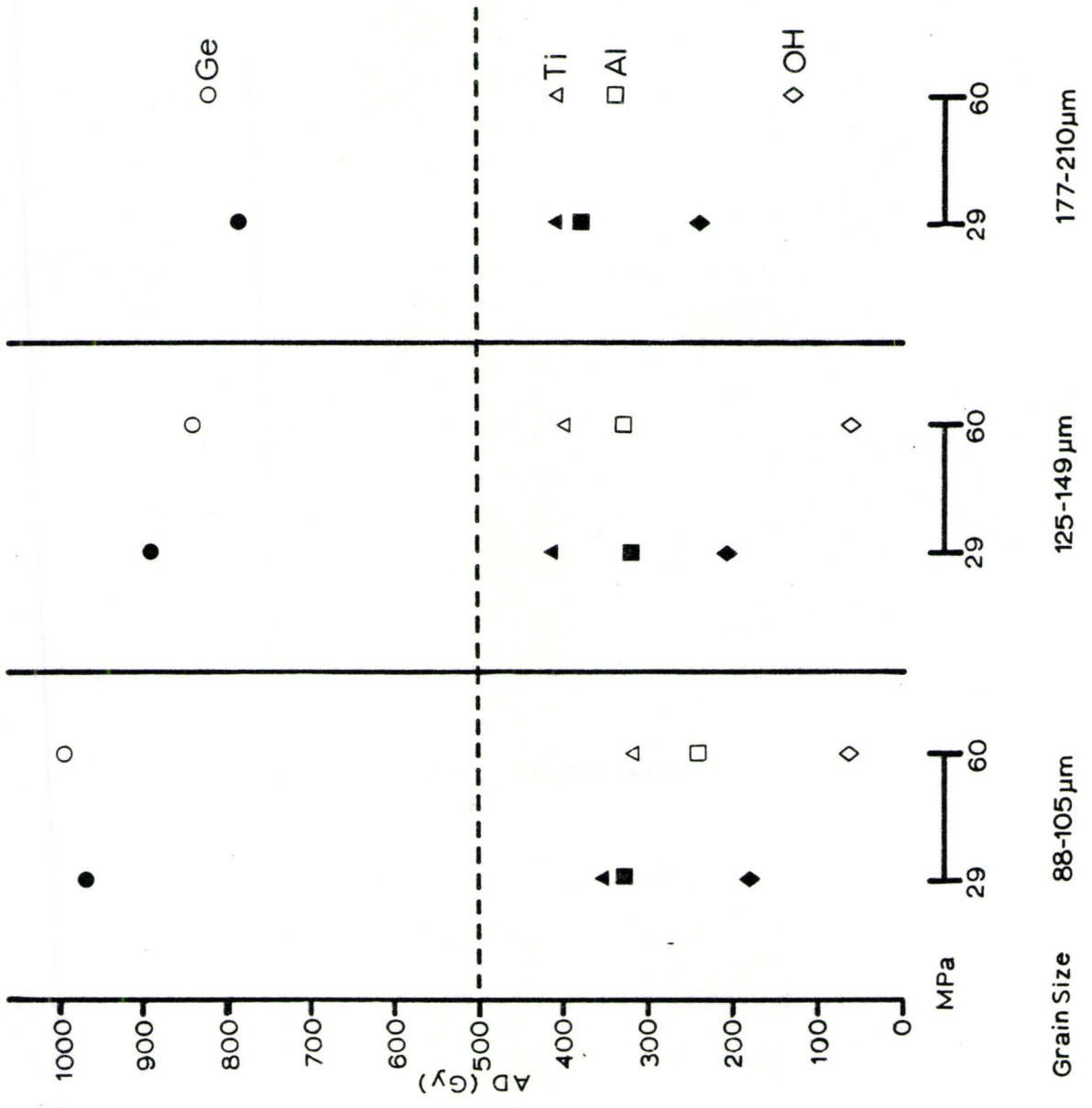
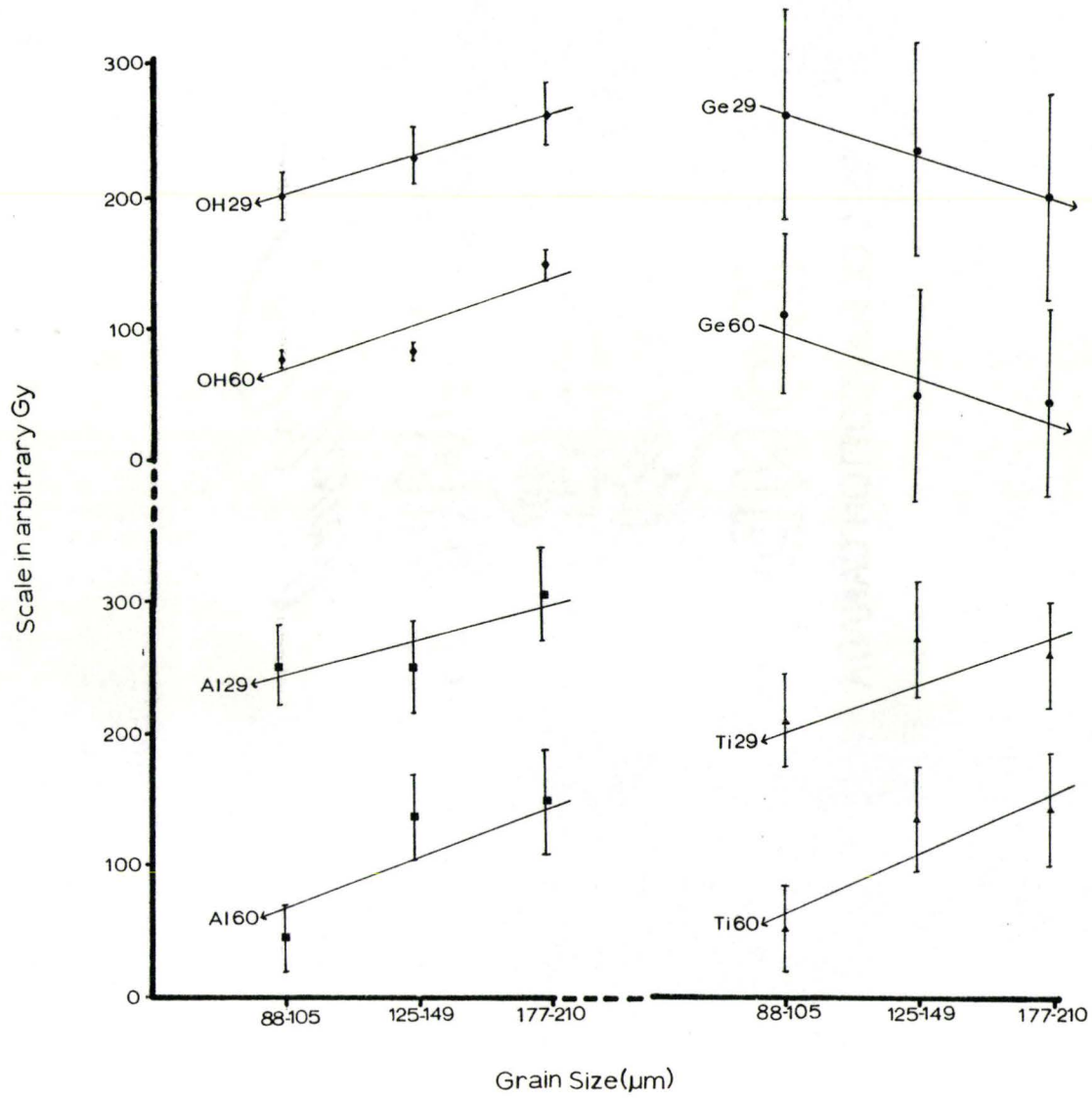


Figure 8.5. Chi-square determined trends for the compression experiment

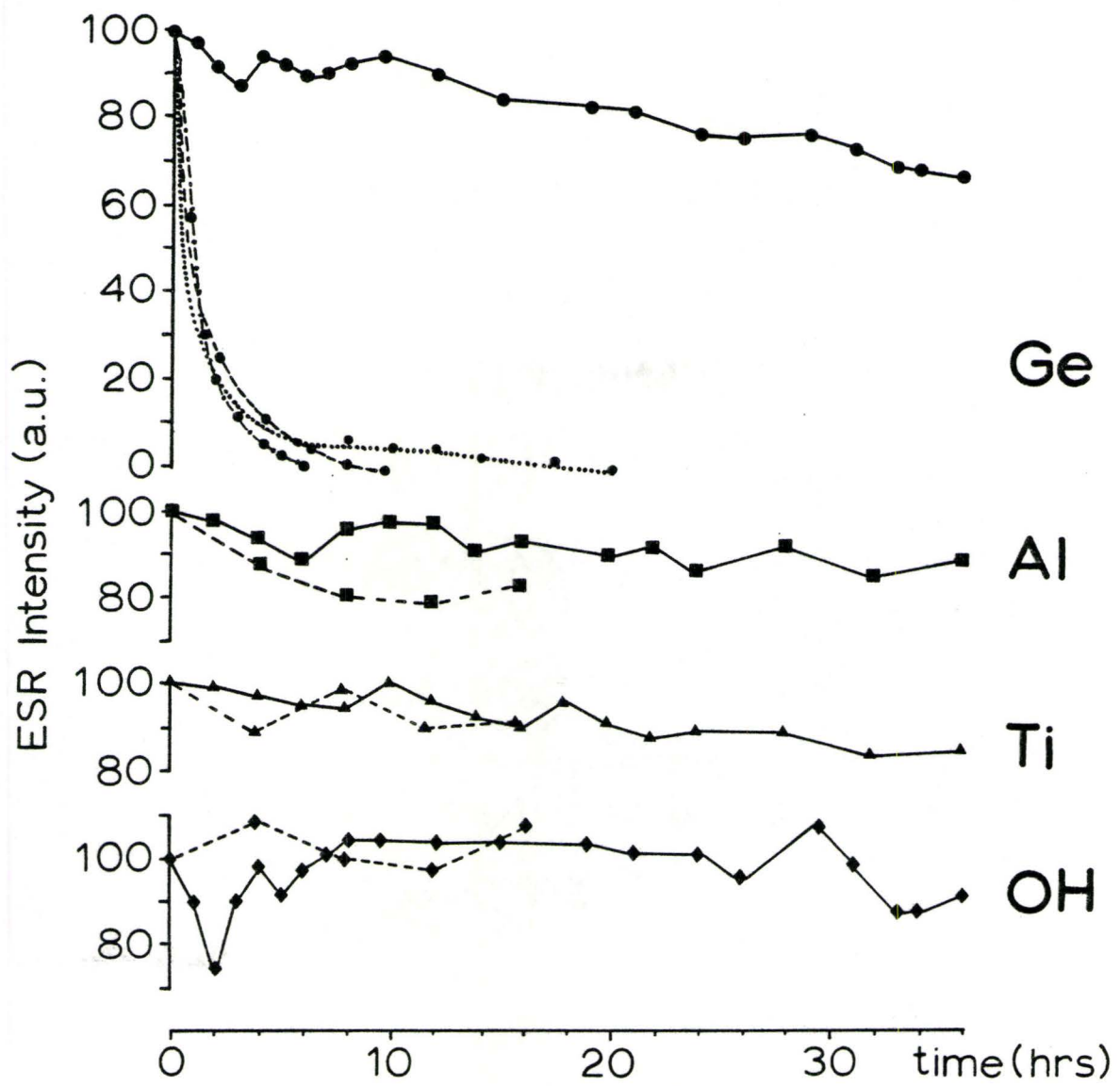


determine whether the data defines such a trend. The resulting trends are shown in Figure 8.5 and it appears that the AD's in smaller grain sizes were reset to a greater extent than larger sized grains for the OH, Al, and Ti centers and AD's from the Ge center increased more with stress in smaller grain sizes than in larger grain sizes.

8.3 Results of the Bleaching Experiment

Results of bleaching experiments are shown in Figure 8.6. The ESR intensity of OH, Al, and Ti centers are affected little after exposure to UV-light or natural sunlight. The intensity of the Ge signal, however, shows a slow but steady decrease when exposed to UV-light in the cavity while being held in a quartz tube, and would be totally bleached at 120 hours. When exposed to UV and natural light in a thin layer of grains, the Ge spectra was rapidly bleached (within 6 hours for UV light at 50 mW/cm²; within 10 hours for direct sunlight; within 20 hours for diffuse sunlight).

Figure 8.6. Bleaching of ESR intensity. Solid line: exposure to ultra violet in cavity, dashed and dotted line: exposure to UV in a thin layer, dashed line: exposure to sunlight in a thin layer, dotted line: exposure to diffuse sunlight in a thin plane.



Chapter 9: AD Measurements on Natural Fault Gouge

9.1 Geological Settings of Samples

Fault gouge was collected at three sample locations from the San Andreas Fault system in south central and southern California (Figure 9.1a.).

9.1.1 San Jacinto Fault, Anza

Fault gouge was collected from the San Jacinto fault near Anza in Southern California by T. Rockwell (San Diego State University). The fault transects Quaternary alluvial and nonmarine deposits as well as Cenozoic and Mesozoic granitic rocks (Figure 9.1b). Samples collected consist of mid-Quaternary alluvial fan deposits collected at a depth of 8 to 10m, from both the "active" and "inactive" trace of the fault. In both cases the gouge consisted mostly of loose grains together with with some extremely friable arregates of grains.

^{14}C dates on a nearby faulted sag pond demonstrate that the active strand has moved within the past several hundred years. The inactive strand is only 50m southeast of the active strand and is believed to have moved during the Holocene (based on tectonic geomorphic features such as stream deflections and scarps). The San Jacinto fault is the most active branch of the San Andreas fault system in Southern California, approaching annual strain accumulations found on the south central portion of the San Andreas fault proper.

9.1.2 The San Andreas Fault, Palmdale

Samples of fault gouge were collected from the San Andreas fault near Palmdale by D. Schwartz of the U.S. Geological Survey at Menlo Park. The fault transects mostly Quaternary alluvial deposits and Pleistocene nonmarine deposits in this area (Figure 9.1c). The fault zone is approximately 2.5 Km wide; two branches of the S.A.F. the Little Rock Fault and the Nadeau fault can be recognized as distinct breaks. The samples collected consist of masses of friable aggregates, 1 to 3cm in diameter. They were collected within 1 to 2 meters depth, in test pits cut into the main fault zone.

The samples were taken from the part of the San Andreas fault between Wallace Creek and Pallett Creek that last moved in 1857. The amount of displacement varied between 8-10m near Wallace Creek to 3-4m near Pallet Creek. The amount of displacement at the Palmdale section of the fault is estimated at 3m. The times of individual movements have been determined by ^{14}C to lie between 123 and 225 years (Raleigh et al. 1982). This section of the San Andreas fault has the highest annual strain rate accumulation of any section comprising the southern section of the fault, and it is therefore the most active section of the fault.

9.1.3 The San Gabriel Fault, at Big Tujunga Canyon

Samples were collected from the San Gabriel fault in the Big Tujunga Canyon by R. Biegel of the University of Southern California. The fault transects mostly Mesozoic granitic rocks in this area and ranges between 1 and 3m in thickness (Figure 9.1d). The gouge samples were collected within 2-4 meters of the present surface and consist friable lenses of granodiorite that can be broken apart by hand.

According to Slosson and Gray (1984) the San Gabriel fault has been recently active (in 1893) in the region from which the samples were collected. The most recent activity along the San Gabriel fault was in 1971 approximately 25 km northwest of the sample site. It is not certain whether the sampled part moved at this time. Other than this, the frequency of fault activity has not been well documented for the San Gabriel fault, although it may parallel that of the active south central section of the San Andreas, 25Km northwest.

Figure 9.1a. California index map showing the relative locations of the sample sites.

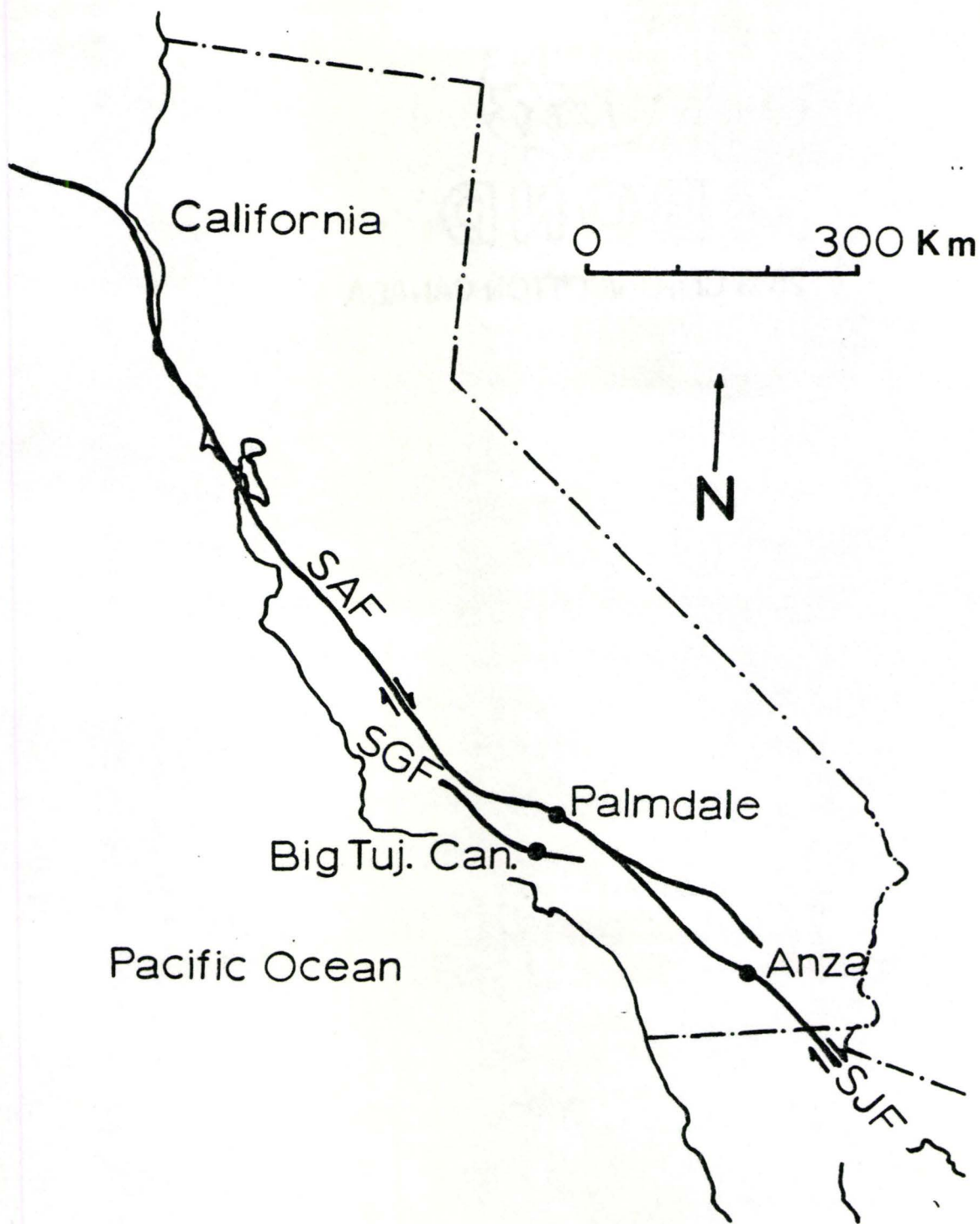
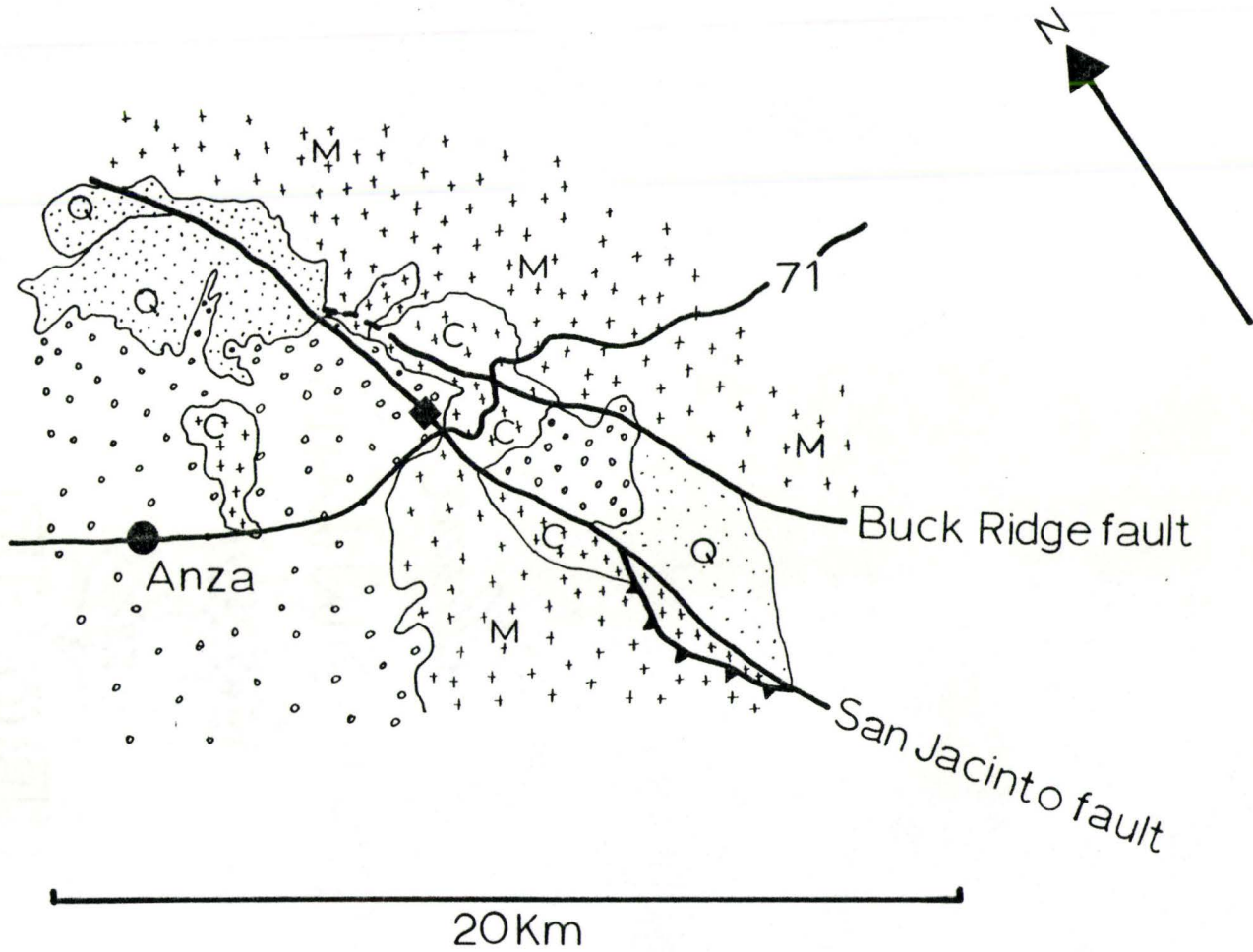


Figure 9.1b. A geological sketch map of the San Jacinto fault near Anza. The square region shows the approximate sample site. (from the geologic map of California; Los Angeles Sheet)

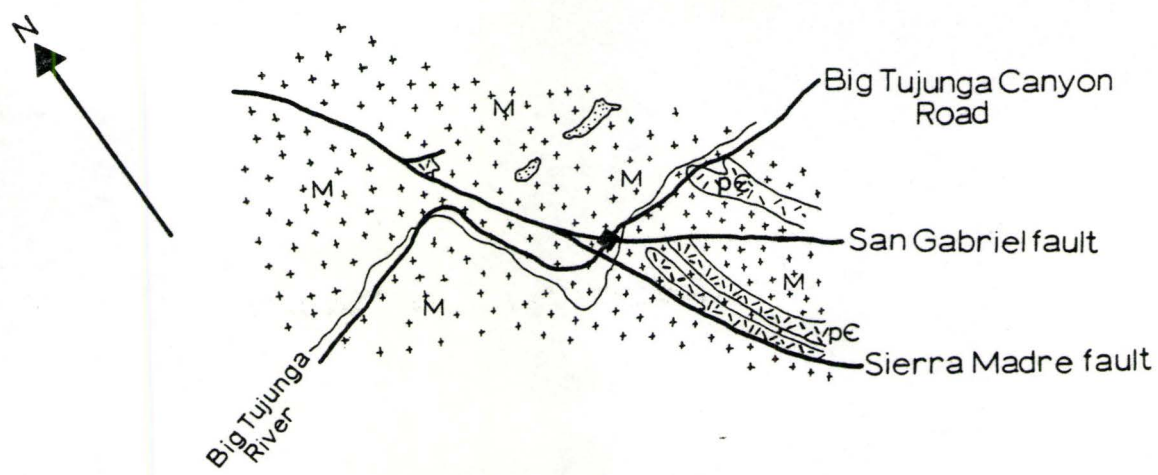
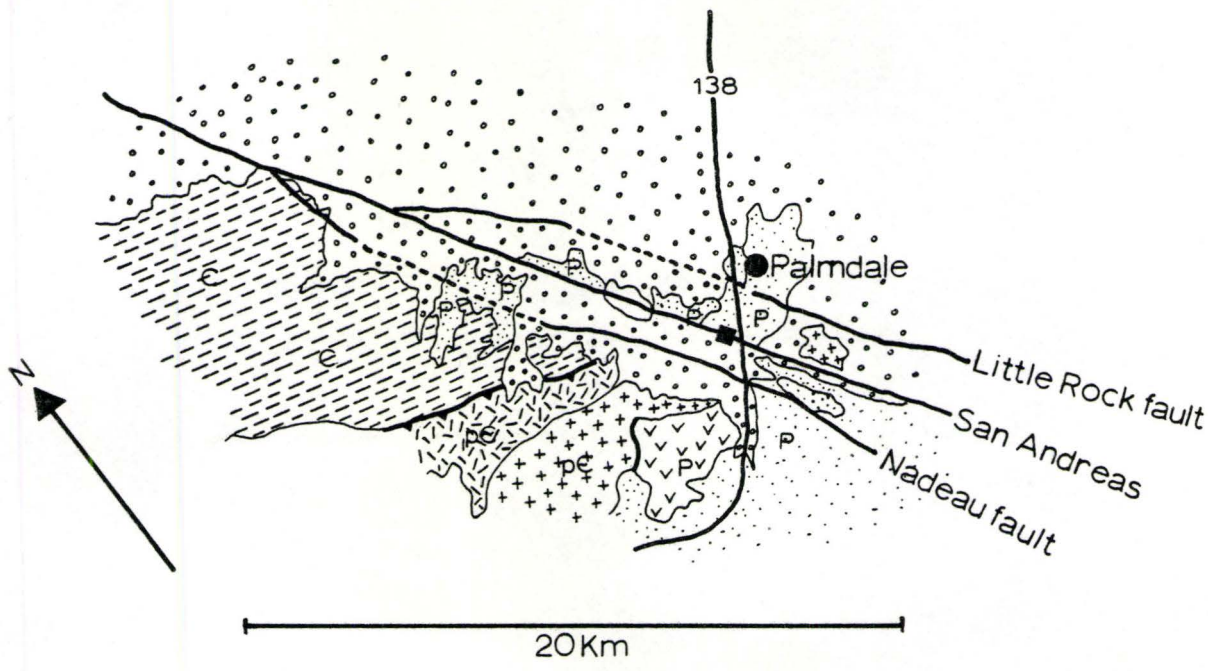


+ granitic
 ••• nonmarine deposits
 ◦◦◦ alluvial deposits

M-Mesozoic C-Cenozoic Q-Quaternary

Figure 9.1c. A geological sketch map of the San Andreas fault near Palmdale. The square region shows the approximate sample site. (from the geologic map of California; Santa Ana Sheet)

Figure 9.1d. A geological sketch map of the San Gabriel fault near the Big Tujunga Canyon. The square region shows the approximate sample site. (from the geologic map of California; Santa Ana Sheet)



++ granitic
 / / gneiss
 / / / / schist
 v v volcanic
.

pE - Precambrian
 M - Mesozoic
 C - Cretaceous
 P - Pleistocene

9.2 Age of Fault Movement for Natural Faults

9.2.1 Assumptions for the Age Calculation

9.2.1.1 Determination of U, Th, and K Dose Rates

Dose rates from the matrix were derived from analysis of U and Th by delayed neutron activation analysis (DNAA) and K by X-ray fluorescence (XRF). Internal dose rates in quartz were assumed to be negligible. Dose rates per ppm U, Th, 1% K, and 100 ppm Rb have been calculated by Nambi and Aitken (1986). The concentration in ppm and % along with the calculated dose rates per ppm of these radionuclides allow for the determination of total α -, β -, and γ - doses emitted in the matrix surrounding the quartz. The values used for the age calculations for the various faults are shown in Table 9.1.

9.2.1.2 Attenuation

Attenuation of radiation in matter occurs when part of the energy of the radiation is transferred to the material. The rate of this process is dictated by the stopping power of the material. Because the matrix is assumed to be infinite (compared to the range of γ and β radiation) the γ and β dose is assumed to be uniform everywhere and no attenuation of γ -rays needs to be considered. Only attenuation of α and β particles within the quartz must be taken into account.

As discussed previously the α -particle is attenuated more in quartz than β -particles and γ -rays. Alpha particles penetrate 5-40 μm in quartz while the beta particle has a penetration range of 2mm, and the γ rays can penetrate up to 30cm in rock.

9.2.1.3 Alpha Dose

The contribution of α -particles to the AD of the sample must be corrected for in the determination of the dose rate (DR) for the system. Since the α -particle penetrates between 5 and 40 μm in quartz, the overall α -dose contribution to the grain will be grain size dependent (larger grains will have proportionally less α -dose). The total α -dose contribution to the AD for a sample (of particular grain size) is calculated separately by integrating with respect to the volume that encompasses the penetration limit of the α -particle using a computer program designed by R. Grün (1987); an average α -particle penetration depth in quartz of 20 μm is used. This correction factor is then added to equation 2.1 in place of the $G_{\text{U,Th-}\alpha^{\text{D}}\alpha}$ terms which only corrected for α -attenuation in 2π geometry for layers.

9.2.1.4 Beta Dose

Beta particles have a penetration range of approximately 2mm in quartz. Beta particles, unlike α -particles do not

follow straight ionization paths in minerals but rather follow diffuse paths. This leads to a β -particle backscattering effect at the surface of a grain which can, in effect fill extra traps or decrease traps by knocking electrons out. An attenuation correction factor for β -particle scattering is defined by the following equation (Yokoyama et al., 1982):

$$G_{\beta} = 0.5(1 - \exp(-\mu d)) / (\mu d)$$

where $\mu = (3.3P)$ and d is the thickness of a layer (2π geometry) in cm.

P is the effective range of a β -particle with energy E (MeV) in a medium of density ρ .

$$P = 0.0825((1 + 22.4 E^2)^{-0.5} - 1) / \rho$$

As noted above this correction factor G_{β} is for a layer in 2π geometry. It is assumed that the correction factor calculated for the layer holds for a sphere with the diameter substituted for the layer thickness.

The correction factor G_{β} for each beta emitter in a decay chain (each emits a β -particle of different energies) is used to give a G_{β} for the whole decay chain. Therefore the global G_{β} for each decay chain $G_{\beta EC}$ is calculated in the Data-IV computer program designed by R. Grün (1986) using the following formula:

$$G_{\beta EC} = \frac{\sum_{b=1}^N G_{\beta EB}(b) \cdot f_b \cdot E_{av}(b)}{\sum_{b=1}^N E_{av}(b)}$$

E_{av} = average energy of emitted beta particles

N = total number of beta emitters

f_D = frequency of beta emission

$G_{\beta EB}$ = correction factor for each beta emitter in a decay chain:

$$G_{\beta EB} = \frac{\sum_{T=1}^n G_E(T) \cdot f_T \cdot E_{av}(T)}{\sum_{T=1}^n av(T)}$$

n = total number of transitions

f_T = transition frequency (each beta emitter may have several transitions).

These are listed with their respective radionuclide concentrations in Table 9.1.

Therefore the β -dose correction factor used for quartz grains was $G_{\beta EC} \cdot D_{\beta}$.

9.2.1.5 Gamma and Cosmic Ray Correction

Gamma rays follow straight paths and are not significantly attenuated in the size of quartz grains used. Therefore no attenuation correction factor for γ -particles was used.

Cosmic rays, for the most part, penetrate only the first few meters of the sediment (except for a small concentration of muons). Since the samples used in this study were collected at a depth between 1-6 meters and they were probably located much deeper during most of their history, and therefore a cosmic input to the AD is probably negligible.

9.2.1.6 Correction for Water in the Matrix

The absorption of radioactive particles is much higher in water than in soil and therefore a water correction factor must be incorporated into the age calculation for samples taken in a wet environment. A formula for determination of this correction factor for sediments has been given by Bowman (1976).

$$W_{\alpha, \beta, \gamma} = [1 + H_{\alpha, \beta, \gamma} (X/100 - X)]^{-1}$$

H = 1.49 for α , 1.25 for β , 1.14 for γ

X = water content in wt. % (wt. of wet sample - wt. of totally dry sample).

For this study a water correction factor was not determined (sample dried out before this effect was perceived).

9.2.1.7 k value (Alpha-Efficiency)

Due to the ability of alpha particles to saturate all available traps along their ionization path through a substance, alpha particles have a lower ionization efficiency

than beta and gamma particles and therefore their efficiency is lower (β and γ efficiencies = 1). The k value for an α -particle in a substance is determined by dividing the ESR intensity per Gy for α -particles (substance irradiated with a monoenergetic α source) by the ESR intensity per Gy of β particles of the same energy. The experimentally determined k value for quartz is 0.07.

9.3 Sample Age Calculation

Using equation 2.1 with the integrated alpha dose replacing the alpha dose attenuation factor to calculate ages for this study changes equation 2.1 to the form show below:

$$DR = C_U(SED) (G_{U-\beta} D_\beta + D_\gamma(U)) + C_{Th}(SED) (G_{Th-\beta} D_\beta + D_\beta(Th)) + C_K(SED) (G_{K-\beta} D_\beta + D_\gamma(K)) + D_\alpha + D_{cos} G_{cos} \quad 9.1$$

Where G_β = attenuation factors for α, β , and cosmic rays (note cosmic rays are neglected)

D = dose rate per concentration (D_{cos} = measured cosmic dose)

$C_{U, Th, K}$ = concentration of radioactive elements present

D_α = integrated alpha dose for the particles (from computer program)

(note: water attenuation is neglected at this point).

Using this equation a sample age calculation will be performed for the 95 μ m grain size fraction of the San Gabriel Fault at Anza.

The AD for this sample as determined by the additive dose extrapolation method is 340 Gy.

The DNAA and XRF determined radionuclide concentrations for the matrix are as follows: U = 4.0ppm, Th = 9.0ppm, K = 2.43%. The released dose rates per radionuclide are taken from Nambi and Aitken (1986); (note: γ attenuation in a solid is not taken into account here as it will have a negligible affect on the determination of DR in a fault gouge system) 1ppm U(238 and 235 chains): $\alpha = 2.78 \cdot 10^{-3}$ Gy/a, $\beta = 1.47 \cdot 10^{-4}$ Gy/a, $\gamma = 1.14 \cdot 10^{-4}$ Gy/a; 1ppm Th(232-206 chain): $\alpha = 7.38 \cdot 10^{-4}$ Gy/a, $\beta = 2.86 \cdot 10^{-5}$ Gy/a, $\gamma = 5.21 \cdot 10^{-5}$; 1% K (K-40 chain): $\beta = 8.14 \cdot 10^{-4}$, $\gamma = 2.42 \cdot 10^{-4}$ Gy/a.

The beta correction factors for the decay chains (as determined using the Data-IV computer program) in the 95 μ m grain size sample are as follows: U-decay chains = 0.9071, Th-232 decay chain = 0.8612, K-40 decay chain = 0.9663

The alpha dose contribution to the dose rate (as determined by the alpha-sphere computer program) = $2.88 \cdot 10^{-4}$ Gy/a

Therefore using equation 9.1 the DR is determined as follows:

$$\begin{aligned}
 DR = & 4.0\text{ppm}(0.9071(1.47 \cdot 10^{-4} \text{ Gy/a}) + 1.14 \cdot 10^{-4} \text{ Gy/a}) \\
 & + 9.0\text{ppm}(0.8612(2.86 \cdot 10^{-5} \text{ Gy/a}) + 5.21 \cdot 10^{-5} \text{ Gy/a}) \\
 & + 2.43\%(0.9663(8.12 \cdot 10^{-4} \text{ Gy/a}) + 2.42 \cdot 10^{-4} \text{ Gy/a}) \\
 & + 2.88 \cdot 10^{-4} \text{ Gy/a} = 4.467 \cdot 10^{-3} \text{ Gy/a} \quad (9.2)
 \end{aligned}$$

Therefore from equation 9.2 the age can be calculated with the known values of AD (340 Gy) and DR ($4.467 \cdot 10^{-3}$ Gy/a)

$$\text{where AD} = \int_0^t \text{DR}(t) \text{ dr}$$

$$\text{Therefore } t = \text{AD/DR} = 340 \text{ Gy} / 4.467 \cdot 10^{-3} \text{ Gy/a} = 76,100\text{a.}$$

It should be noted here that if the same calculation is performed for sediment with a 10 wt. % water content, the dose rates supplied to the quartz grains are decreased and the age calculated increases to 86,600a. This is a significant difference and it shows the importance of determining the % of water in the sample matrix as soon as possible after sample collection (or ensuring that little water is lost from the sample).

9.4 Disequilibrium

9.4.1 Uranium Disequilibrium

Uranium and thorium counts within the quartz structure are negligible and therefore internal disequilibrium for quartz is not considered.

Disequilibrium in the fault gouge matrix presents a problem when determining the dose rate (DR) received by the quartz over time. Increased solubility of some radionuclides in the uranium and thorium decay series may lead to secular disequilibrium among parent and daughter isotopes in some environments.

^{234}U is more soluble in water than ^{238}U because its +6 valence state makes it easily oxidized and taken up in anionic complexes such as $\text{UO}_2(\text{CO}_3)_3^{4-}$. This will lead to a deficiency of ^{234}U and ^{230}Th with respect to ^{238}U in the matrix which will have an effect on the dose rates received by the quartz over time.

Disequilibrium in fault gouge is dependent on the radionuclide equilibrium state in the gouge parent rock (wall rock) and the environmental state of the gouge (open or closed system) in the fault zone.

The felsic igneous and terrestrial clastic parent rocks through which most of the south central and southern sections of the California fault zones pass are assumed to be in secular equilibrium for the U decay series. Felsic igneous rocks have had sufficient time to establish equilibrium. Terrestrial clastics are mostly derived from eroded, weathered igneous rocks in the area (San Gabriel Mountains). This would

tend to deplete the clastics in the soluble radionuclides leaving a daughter deficiency in the sediment. Secondary cementation (e.g. calcite) would increase the deficient ^{234}U in the sediment although the amount of enrichment is not predictable (for ground water systems the activity ratio $^{234}\text{U}/^{238}\text{U}$ has been found to vary between 1.0 and 12.0). After cementation the clastic sediment can be assumed to be a closed system to water percolation internally. Ku (1975) found that $^{230}\text{Th}/^{234}\text{U}$ ages of calcite cement in clastic sediments were internally consistent. Zymela (1985) found the $^{234}\text{U}/^{238}\text{U}$ and $^{230}\text{Th}/^{234}\text{U}$ activity ratios = 1.0 for clastic subaerial sediments. The assumption that parent rock supplying fault gouge is in U series equilibrium is used for this study as parent rock samples were not available for verification.

Deep active fault zones have a considerably decreased porosity with respect to their parent (wall) rock. This would essentially preclude a large water percolation within the fault zone and therefore disequilibrium effects on the dose rate are not important. However, surface fault zones (within 300m of the surface) have a considerable amount of clay material (in different amounts) within them. During pre-faulting activity on faults these clays may swell and effectively decrease the critical shear stress on the fault. Upon fault movement most of the water in the clays would be expelled, and with it soluble daughter products. During

inactive times there would also be much ground water percolation through a near surface fault system which could also wash out soluble radionuclides. The excess ^{234}U would most likely be incorporated into the wall rock nearest the fault zone (it may be possible to use this excess daughter product in the wall rock for U-series dating of the fault). In such a case of deficit ^{234}U in the fault gouge the dose rate would be overestimated, giving an age that is too young.

Therefore, for near surface fault systems that have a high frequency of activity, such as faults found in Southern California, and containing a high proportion of secondary minerals (clay material), the ^{234}U isotope would be expected to be significantly depleted. Production of secondary clay minerals would be enhanced over cementation in the decreased porosity fault zone where most of the water taken up by swelling clays has been expelled.

At this point it can only be suggested that ^{234}U leaching be assumed for clay rich fault gouge although it is probable that there is a variation in the amount of ^{234}U leached out in fault gouge with different proportions of clays. There may be a relationship between the % of clay material in the fault gouge and the activity ratios $^{234}\text{U}/^{238}\text{U}$ and $^{230}\text{Th}/^{234}\text{U}$ (the variance from 1 of these ratios with respect to clay proportion). If the amount of ^{234}U leaching could be estimated

with a relationship as described above then a proportion of the dose rate for the ^{234}U decay sequence (per ppm U) could be added to the dose rate for the non-leachable radionuclides in the U-decay series to give a more accurate estimation of DR.

9.4.2 Determination of DR Assuming ^{234}U Leaching

The only decay-chain that is significantly affected by ^{234}U leaching is the ^{238}U decay-chain. Here it is assumed that the maximum leaching of ^{234}U is 10% ($^{234}\text{U}/^{238}\text{U} = 0.9$) in a fault zone. The percent of the ^{238}U dose rate lost with 10% ^{234}U leaching was determined from the dose rate tables in Nambi and Aitken (1986). The new dose rates determined are as follows: $U_{\beta} = 1.38 \cdot 10^{-4}$ Gy/a, $U_{\gamma} = 1.03 \cdot 10^{-4}$ Gy/a, $U_{\alpha} = 1.5 \cdot 10^{-4}$ Gy/a (Th_{α} same as above + $U_{\alpha}(10\% \text{ loss}) = 2.71 \cdot 10^{-4}$ Gy/a). Using eq. 9.1, the DR for 10% ^{234}U loss = $4.37 \cdot 10^{-3}$ Gy/a which gives an age of 77,820a (an increase of approximately 2% in age).

9.4.3 Radon Loss

Due to the high geochemical mobility of ^{226}Ra and the high diffusion rate of the noble gas ^{222}Rn , dose rates can be enhanced because of the disequilibria caused by these elements in the U and Th decay chains. In terms of dose rates, ^{226}Ra leaching can be treated the same as ^{222}Rn loss (the difference in the dose rate only arises from the emission of one additional alpha particle).

In a clastic system such as a fault zone, migration of ^{222}Rn out of the gouge and incorporation of ^{222}Rn into the gouge (from surrounding rocks) should be relatively steady state. In such a system it can be assumed that depletion of ^{222}Rn can exceed no more than 50% in a fault zone. Fukuchi et al. (1986) compared dose rates with no radon loss to dose rates with an assumed 50% ^{222}Rn loss. The ratios of dose rates with no loss to dose rates with 50% loss were 1.15 and 1.13, which did not change their sample ages significantly. However, a 50% radon loss may have more effect on the dose rate for younger samples as shown in the calculation below:

The effect of 50% Radon loss on the U and Th decay chains were determined from the tables of dose rates in Nambi and Aitken (1986). $U_{\beta} = 1.469 \cdot 10^{-4}$ Gy/a, $Th_{\beta} = 2.857 \cdot 10^{-5}$ Gy/a, $U_{\gamma} = 1.138 \cdot 10^{-5}$ Gy/a, $Th_{\gamma} = 5.199 \cdot 10^{-5}$, and $(U_{\alpha} = 1.21 \cdot 10^{-4}$ Gy/a + $Th_{\alpha} = 8.62 \cdot 10^{-5}$ Gy/a) = alpha dose = $2.08 \cdot 10^{-4}$ Gy/a. Calculation of DR using eq. 9.1 gives $DR = 4.38 \cdot 10^{-3}$ Gy/a, and therefore an age of 77,600a. (a variation of $\pm 2\%$). Therefore Radon loss is not significant in age calculations for faults active in the Pleistocene.

9.4.4 Determination of DR Assuming 50% Radon Loss and 10% ^{234}U Leaching

Both Radon loss and ^{234}U leaching would be expected for open fault systems. U-series dose rates would be most affected by ^{234}U leaching. Th-series dose rates are not significantly depleted by ^{234}U leaching, but are depleted somewhat by Radon loss. The values used for total dose rate calculation are as follows: $U_{\beta} = 1.37 \cdot 10^{-4}$ Gy/a, $U_{\gamma} = 1.02 \cdot 10^{-4}$ Gy/a, $U_{\alpha} = 1.16 \cdot 10^{-4}$ Gy/a, $Th_{\beta} = 2.857 \cdot 10^{-5}$ Gy/a, $Th_{\gamma} = 5.199 \cdot 10^{-5}$, $Th_{\alpha} = 8.62 \cdot 10^{-5}$ Gy/a (α -dose = $1.16 \cdot 10^{-4}$ Gy/a + $8.62 \cdot 10^{-5}$ Gy/a = $2.02 \cdot 10^{-4}$). Using eq. 9.1 $DR = 4.29 \cdot 10^{-3}$ Gy/a and the age is 79,200a. This is a variance of $\pm 4\%$ which must be considered as another source of error.

9.5 Error Determination

Error is determined for AD. The variation in the AD value was determined by additive dose back extrapolation with one point omitted for each separate AD determination. For the San Jacinto 95 μm sample this was found to be less than 1% variation in AD.

Artificial dose error must also be incorporated into the error calculation. This averages out to be $\pm 8\%$ variation in AD.

The error in ESR age for 100% uncertainty of water content in a sediment with 20 wt. % water is 7.6% (Zymela, 1985). The error in ESR age for U and Th series disequilibrium is ± 4 %.

It is not known at this point the extent of error for β - and α - attenuation in spherical grains and therefore an estimation of error in the DR determination has not been attempted.

The error is then determined as follows;

$$\text{Error} = \sqrt{n^2 + n^2 + \dots + n^2 - 1^2} = AD(\sqrt{1^2 + 8^2 + 7.6^2 + 4^2}) = \pm 41 \text{ Gy.}$$
 The 41 Gy error in AD give an error in age of approximately 11,000a. Therefore the age of the sample is 76,100a \pm 11,000.

9.6 Calculated Ages

9.6.1 The Results of AD Determinations on Real Faults

AD determinations were performed on fault gouge from the San Jacinto active strand to determine if total zeroing had actually taken place. AD's of fault gouge measured in the various particle sizes replicate to some extent the results of the compression experiment (Figure 9.2a). The lowest AD's are found for the OH center and are uniform in all particle sizes. As in the compression experiment, the AD's of the Al center

are much larger than those of the OH center. The AD of the Al center decreases with decreasing grain size, approaching that of the OH center for the finest particles. The Ti center of this sample shows no consistent trend in AD with grain size, and certainly does not approach the OH value (the Ti center underwent the least lowering in the compression experiment).

The signals from the San Andreas sample (SAF) shows the expected decrease in AD with decreasing grain size (Figure 9.3a). There is an approach to a plateau for the OH signal. The Al center does not converge on the OH plateau and therefore is not assumed to have been totally zeroed.

The E_1' and Al centers from the San Gabriel sample (SGF), show the decreasing grain size trend, but do not converge with the OH center values for that sample (Figure 9.4a). The OH signal does not, however, display a true plateau in this sample, and cannot therefore be assumed to have been zeroed at the time of last faulting.

The consistently lower AD's of the OH signal confirm the experimental evidence that this center is the most readily zeroed under stress.

9.6.2. Table 9.1

All the data used for calculation of ages are shown in table 9.1. The AD has been determined for individual ESR centers for each grain size (average grain size) of the natural fault gouge samples. The measured concentrations of $C_{U,Th,K}$ are given for the fault gouge samples. Using the grain sizes and the radionuclide concentrations, the α dose and β dose correction factors were calculated using the computer programs described above. From these the dose rate (DR) was determined and used along with the AD to calculate the ages for the ESR centers in different grain sizes for the fault gouge samples. Error determinations follow the same procedure as described in section 9.4.

9.6.3 Age vs. Grain Size

Figures 9.2b, 9.3b, and 9.4b show the apparent ages calculated from the AD's of each center of samples from the San Jacinto Fault, the San Andreas Fault, and the San Gabriel Fault respectively using equation 9.1. The trends of variation in AD with grain size, and the variations between various ESR centers are reproduced in the ages, although the ages are not strictly proportional to AD due to the non-uniform accumulation of dose discussed earlier.

At each site the OH center gave the lowest AD's and ages. The OH center of the San Jacinto fault sample showed the only well developed AD plateau development in any of the samples studied. The plateau yields an age of about $76,000 \pm 11,000$ years. The ages calculated from the lowest AD values obtained for the OH center for the San Andreas and the San Gabriel faults are $74,500 \pm 10,000$ years and $38,000 \pm 6,000$ years, respectively. The true ages of last movement are somewhat younger, still since the plateau has not yet been reached by these data.

Table 9.1. The presentation of measured and calculated data used in the determination of ages for the natural fault samples.

Table 9.1

Sample	Center	G. Size (μm)	AD(Gy)	CU(ppm)	CTh(ppm)	CK(%)	α -Dose (10^{-4} Gy/a)	β -Corrections U, Th, K	DR(10^{-3} Gy/a)	Age(a)	Error(a)
SJF	OH	96.5	340	4	9	2.43	2.85	.906,.860,.966	4.46	76,114	11,000
		137.5	350	4	9	2.43	2.02	.884,.831,.951	4.33	80,900	12,000
		275	340	4	9	2.43	1.02	.821,.760,.903	4.08	83,400	10,734
		460	335	4	9	2.43	0.61	.751,.693,.839	3.85	87,100	13,000
	Al	96.5	355	4	9	2.43	2.85	.906,.860,.966	4.46	79,600	9,200
		137.5	526	4	9	2.43	2.02	.884,.831,.951	4.33	122,000	17,080
		275	760	4	9	2.43	1.02	.821,.760,.903	4.08	186,000	25,000
		460	913	4	9	2.43	0.61	.751,.693,.839	3.85	237,000	23,000
	Ti	96.5	1200	4	9	2.43	2.85	.906,.860,.966	4.45	269,000	27,000
		137.5	1223	4	9	2.43	2.02	.884,.831,.951	4.33	283,000	38,000
		275	608	4	9	2.43	1.02	.821,.760,.903	4.08	149,000	19,800
		460	n.d.								
SAF	OH	96.5	420	3	26	2.45	4.76	.906,.860,.966	5.73	73,200	10,000
		137.5	430	3	26	2.45	3.37	.884,.831,.951	5.54	77,600	9,700
		275	650	3	26	2.45	1.69	.821,.760,.903	5.19	125,000	15,020
		460	850	3	26	2.45	1.02	.751,.693,.839	4.91	173,000	24,000
	Al	96.5	630	3	26	2.45	4.76	.906,.860,.966	5.73	110,000	19,000
		137.5	820	3	26	2.45	3.37	.884,.831,.951	5.54	150,000	21,000
		275	980	3	26	2.45	1.69	.821,.760,.903	5.19	189,000	24,000
		460	n.d.								
SGF	OH	80	150	0.6	19	1.8	3.33	.916,.873,.972	3.81	39,400	6,000
		96.5	165	0.6	19	1.8	2.79	.906,.860,.966	3.74	44,200	5,000
		115	220	0.6	19	1.8	2.35	.897,.846,.959	3.67	60,000	7,550
		137.5	310	0.6	19	1.8	1.98	.884,.831,.951	3.61	85,800	11,200
		196	420	0.6	19	1.8	1.39	.856,.796,.931	3.5	120,000	16,090
		96.5	240	0.6	19	1.8	2.79	.906,.860,.966	3.73	64,000	6,900
	Al	115	310	0.6	19	1.8	2.35	.897,.846,.959	3.67	84,400	8,000
		137.5	330	0.6	19	1.8	1.98	.884,.831,.951	3.61	91,300	10,000
		163	430	0.6	19	1.8	1.67	.872,.814,.943	3.56	121,000	17,000
		196	1010	0.6	19	1.8	1.39	.856,.797,.932	3.53	280,000	34,700
		80	380	0.6	19	1.8	3.33	.916,.873,.972	3.81	99,900	13,000
		96.5	490	0.6	19	1.8	2.79	.906,.860,.966	3.74	131,000	18,300
	E ₁	115	480	0.6	19	1.8	2.35	.897,.846,.959	3.73	128,000	16,500
		137.5	530	0.6	19	1.8	1.98	.884,.831,.951	3.61	147,000	18,000
		163	680	0.6	19	1.8	1.67	.872,.814,.943	3.56	191,000	23,400
		196	990	0.6	19	1.8	1.39	.856,.799,.932	3.52	278,000	32,800

*n.d. = not determined

Figure 9.2. a) AD vs. grain size for the OH, Al, and Ti centers from the San Jacinto Fault (SJF)
b) Age vs. grain size for the OH, Al, and Ti centers from the San Jacinto Fault.

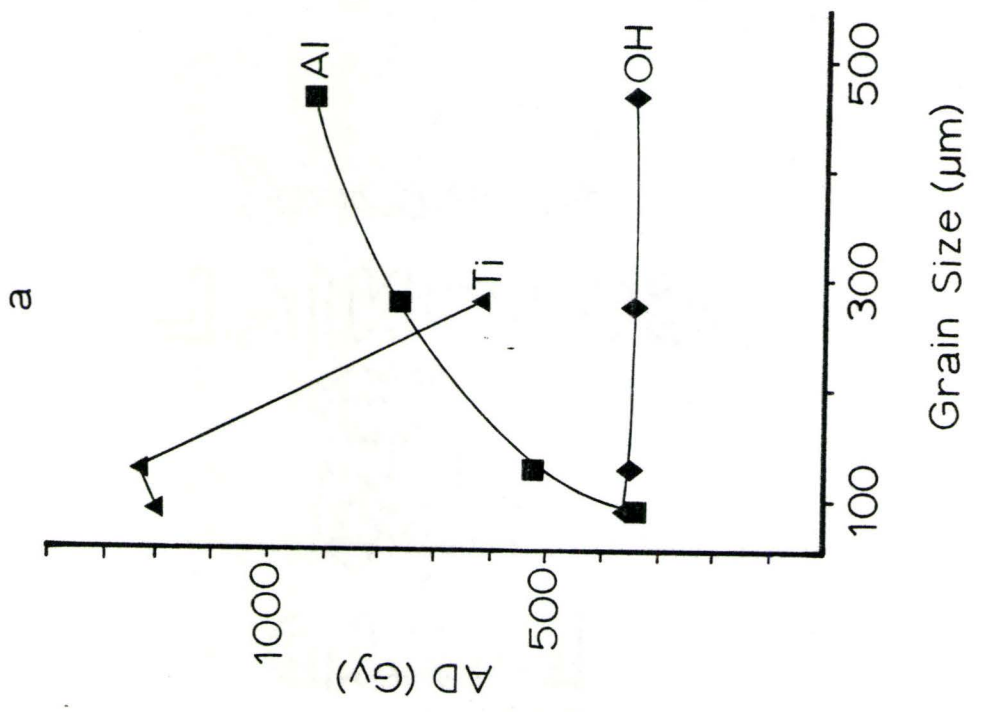
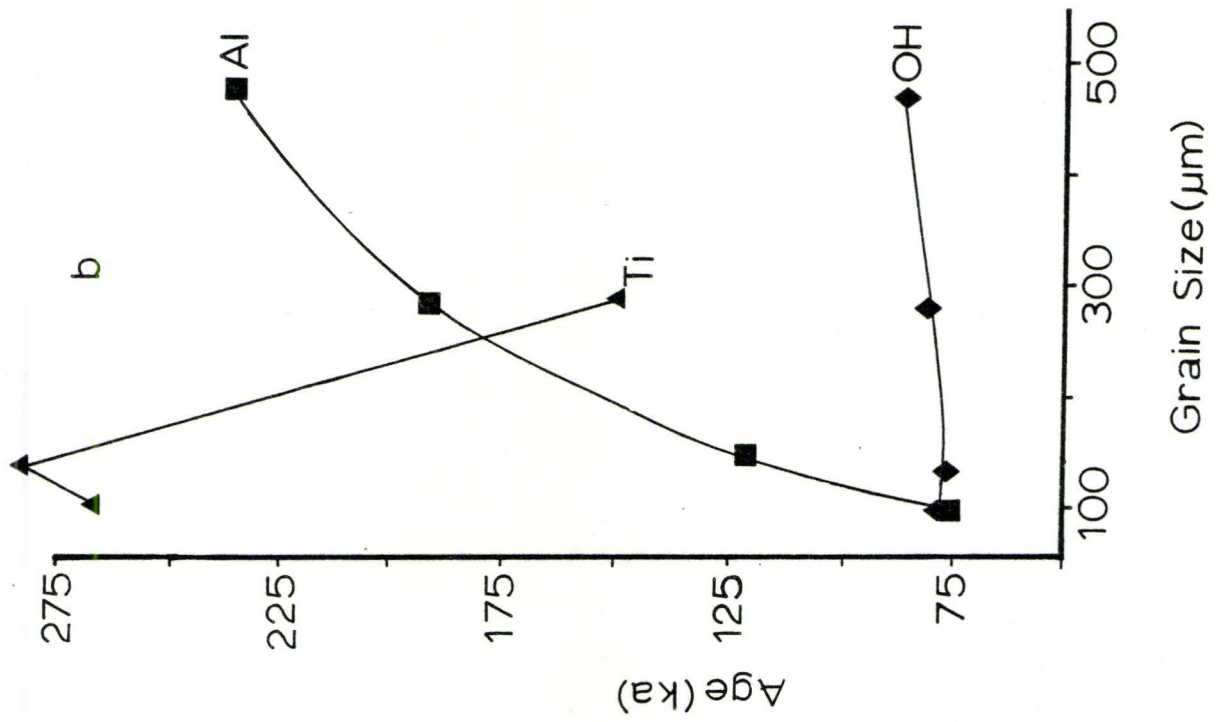
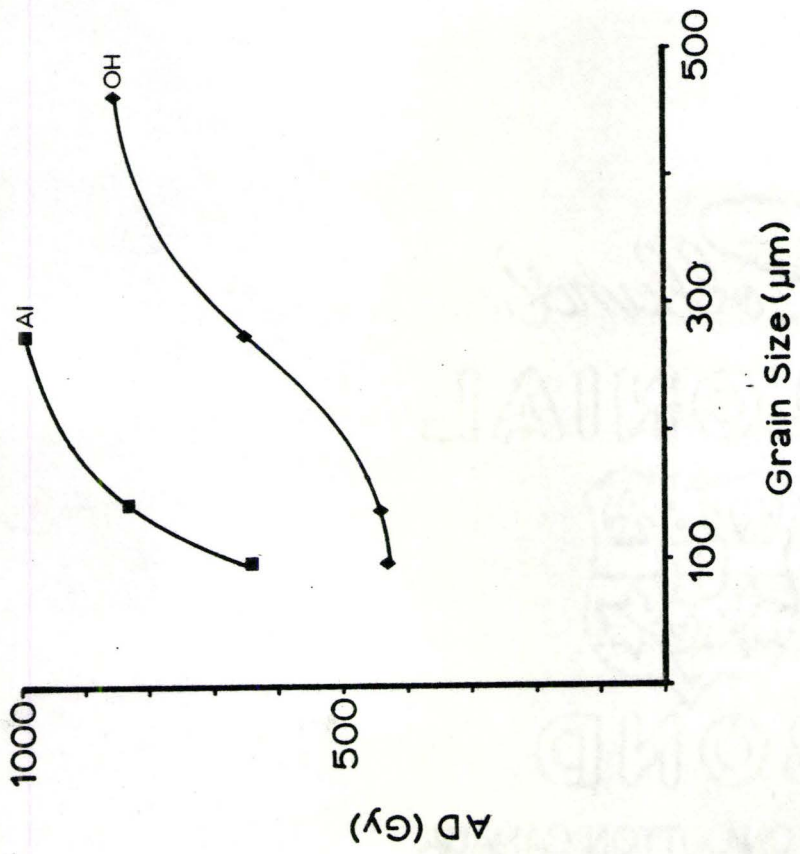
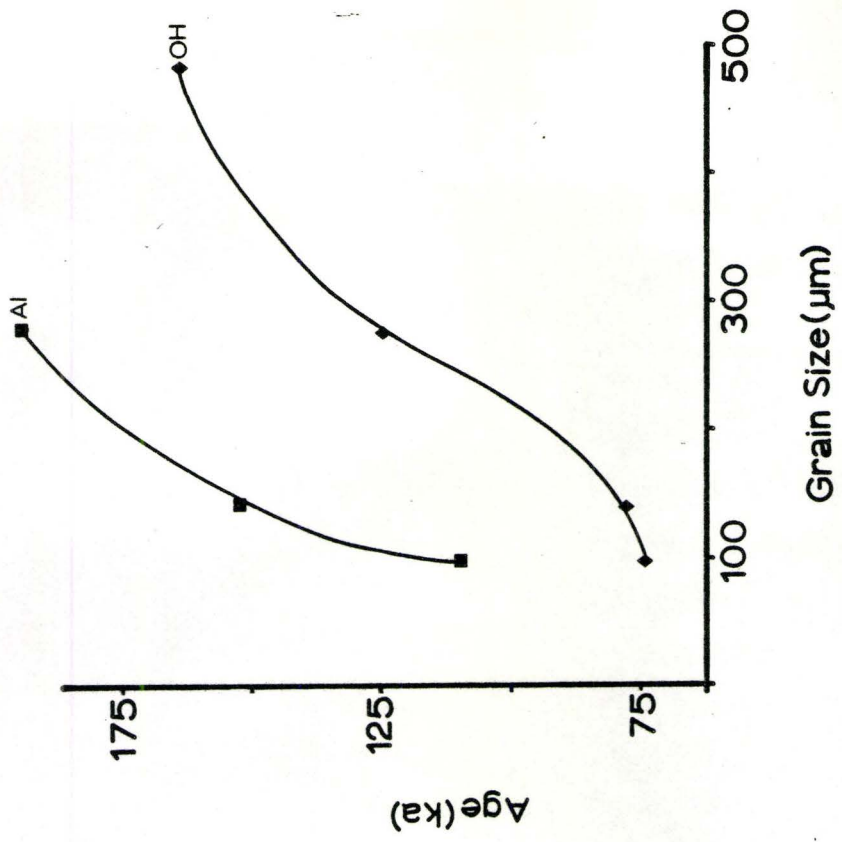
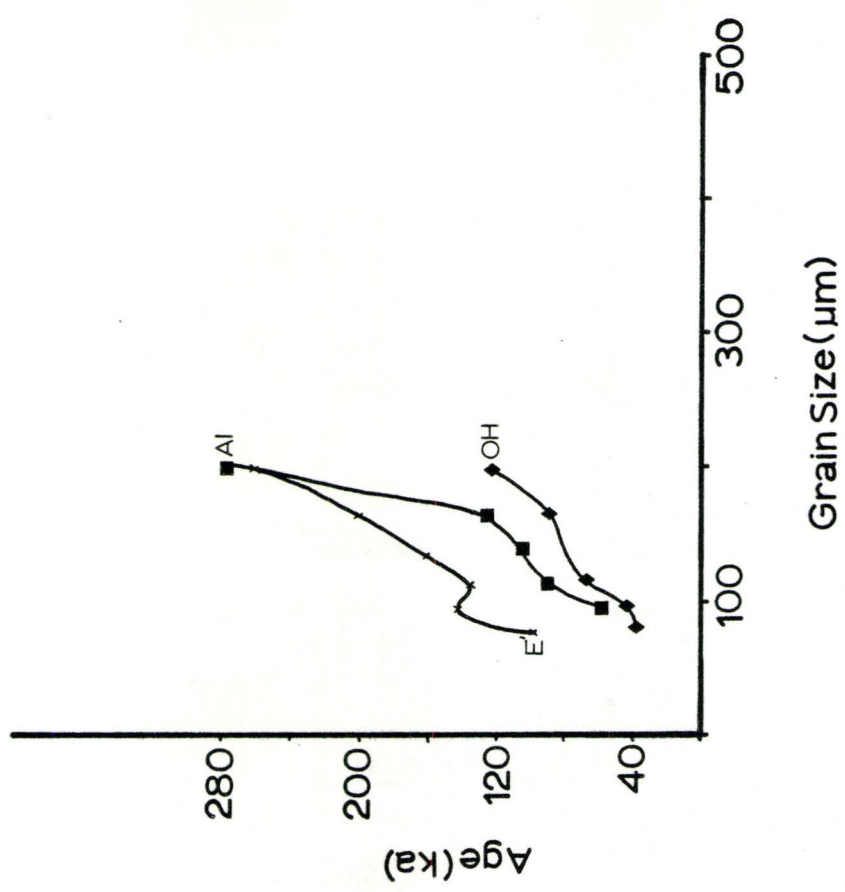
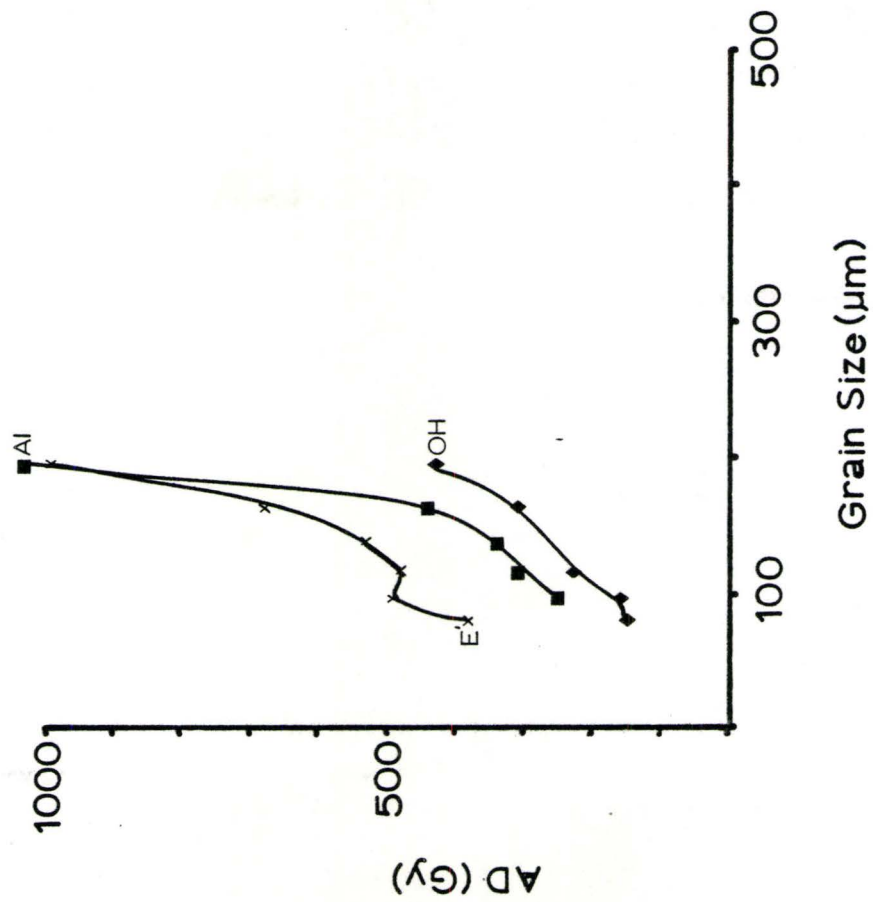


Figure 9.3 a). AD vs. grain size for the OH, and Al center
from the San Andreas Fault
b). Age vs. grain size for the OH, and Al center
from the San Andreas Fault.





Chapter 10: Discussion

10.1 Variation of AD and age with particle size

The experimental results are consistent with the model that the finest grains in fault gouge are more thoroughly reset during fault movement than larger ones. Intensive stress leads to:

1) total resetting of the most stress sensitive center (OH) in grain sizes less than some critical size, resulting in an AD/age plateau over a wide grain size range.

2) partial or total resetting of centers with lesser stress-sensitivities, demonstrated by convergence of AD-values in the finest grain sizes to those given by the OH-center.

Similar decrease in ESR intensity with decreasing grain size was also reported by Fukuchi et al., (1986) although they did not confirm that AD's also decreased.

The age obtained for the last movement on the San Jacinto fault ($76,000 \pm 11,000$ a), is consistent with the geological observation that this fault has been continuously active through the late Pleistocene. However, this segment of the San Jacinto fault is also believed to have moved within the last century. The particular sample of gouge which we analysed was apparently not reset during that movement. Ariyama, (1986) has shown that, in order for some ESR signals in quartz to be

reset, the rock must be subjected to a considerable confining pressure which would not be present at the surface.

Sampling criteria for fault gouge taken between different types of wall rocks were established by Ito and Sawada (1985). Their criteria are based on the observation that fault gouge had to be collected at different depths on different types of faults in order for the ESR age and the stratigraphically estimated age to coincide. Standard sampling depths are based on the 2 MPa minimum stress needed for resetting to occur in quartz as deduced by Ariyama (1985) and are as follows: between basement rocks, or basement and sedimentary rocks, the gouge should be collected at > 20m depth for a reverse fault, > 70m depth for a strike-slip fault, and > 100m for a normal fault. From their data there seems to be a positive correlation between the estimated age of faulting and the ESR determined age from fault gouge collected at the proposed sampling depths.

Therefore, samples collected at the surface may have been last subjected to such a pressure when they were still buried; the time elapsed since then is determined by the local rate of uplift of the fault zone, which may not be known. Therefore, samples of fault gouge that were zeroed by the latest fault movement may still be buried at substantial depth, while surface samples analysed represent some earlier fault

movement.

It should be noted that because of the two different processes that occur during faulting (stable-sliding and stick-slip), there should be an inherent inhomogeneity of stress, and therefore zeroing, associated with these processes, locally incorporated into the gouge. Internal pervasive cataclasis in the gouge during stable sliding may not totally reset the ESR signals and therefore these signals may record an apparent resetting event at some time earlier than the last fault movement. Given enough stress, newly created gouge (produced by the latest movement) at the gouge-wallrock interface should have been totally reset.

Since the samples from the San Gabriel and San Andreas Faults (see Figure 8.8) neither show well-defined plateaus for the OH-center nor congruent AD's for the OH and Al centers in the smallest grain size, it is unlikely that the ages calculated for them ($39,000 \pm 6,000$ and $73,000 \pm 10,000$ a respectively) pertain to the most recent fault activity.

10.2 Mechanism of zeroing of the ESR signal during faulting

10.2.1 Heating

Mechanical deformation and high temperatures are two processes that may be responsible for the resetting of ESR signals in quartz from fault gouge. Isothermal annealing experiments performed on quartz show that all signals become reset in the range of 300 to 400°C (one hour isochronal annealing; Shimokawa et al., (1987); Yokoyama et al., (1985)).

Many authors have reported evidence for very high temperatures being reached on experimental faulting tests. Welded clumps and plates of quartz glass were found in localized areas on fault surfaces by Friedman et al., (1974). Temperatures required to generate glass on the sliding surface (>1000°C), are reported by Teufel and Logan (1978), to occur only at asperity contacts while the average sliding surface temperature merely reaches 115-135°C. Theoretical calculations performed for real faulting situations, based on formulae from Engelder (1978), give average surface sliding temperatures between 150-200°C, well below the temperatures needed for total resetting of the ESR signals.

The generation of heat on the fault surface should produce a detectable heat flow anomaly which is greatest directly over the fault surface. Heat flow data collected on

the San Andreas fault are much lower than was calculated by the average stress (50 MPa) thought to account for movement on the fault (Brune et al., 1969; Kerr 1987). Water circulation has been hypothesized to be the mechanism that acts to distribute heat, as well as thermal conduction of the rock itself which dissipates much of the heat before high temperatures can be reached.

Even if the temperatures produced during faulting were higher than these values, it is clear from the experiments and analyses presented here (see also Fukuchi et al., 1986) that the amount of zeroing increases with decreasing grain size. No such trend would be expected if heating were the main cause of resetting of the ESR signal, since the difference in time needed for a heat pulse to pass through the grain size range analysed here is totally negligible. Therefore, it can be assumed that total resetting was not a result of frictional heating.

10.2.2 Elastic and non-Elastic Deformation

Stressed quartz grains can deform elastically and non-elastically (plastic and brittle deformation). Elastic deformation occurs at lower stress and results in straining the crystal lattice. The force exerted on a bond is the atomic equivalent of stress and the percent change in the bond length

is the equivalent of strain (Suppe 1985). When bonds are strained from their equilibrium separation there is an increase in the potential energy of the bond which is known as the "elastic strain energy". This energy is released when the stress on the crystal is discontinued and the atoms are allowed to return to their equilibrium or stress free positions.

Nonelastic deformation results from dislocations, such as shown in Figure 10.1, which propagate through the crystal lattice. Movement of a dislocation through the lattice results in a rearrangement of molecular energy levels, such that the electron density is removed between nearest neighbors and replaced in the region perpendicular to the direction of strain (between second nearest neighbors (Eberhart *et al.*, 1983)). The degree of deformation will dictate whether stretching of bonds (elastic) or permanent dislocations occur (nonelastic).

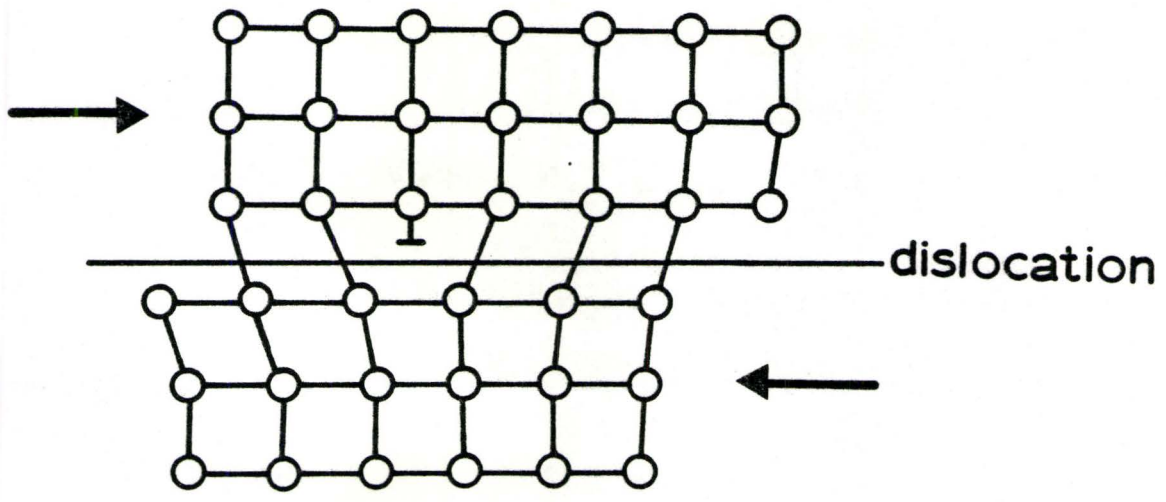
If the applied force is large enough fracturing occurs (60 MPa in Figure 8.3b), where the strength of molecular bonds is broken and new surface area is created. The energy used in creating new surface area is preserved in most cases with recombining of broken bonds with new neighbors. However, since breaking does not occur in a vacuum, stress corrosion from

substances in the air and water will combine with some of the new surface sites and reduce the amount of surface energy in proportion to the potential energy of the solid. The remaining energy is taken up in elastic (or plastic, if confining pressure is sufficient) deformation that precedes fracture in most instances.

Plastic deformation involves the same elastic strain energy on bonds but results in a permanent rearrangement of molecular energy levels perpendicular to the direction of strain. These dislocations usually occur in groups and hence, lines of dislocations form within the crystal. As these lines join up, the crystal distorts in shape.

The compression experiment performed in this study involved quartz gouge placed in the holding cylinder and strained for a short time at room temperature. Hydrostatic conditions in which the same amount of strain was felt by each quartz grain was not obtained and it is therefore likely that inhomogeneous shear strain was induced at grain-grain contacts. At lower stress conditions (29 MPa) the strain at grain contacts was apparently sufficient to induce bond breakages and therefore small scale fracturing. At higher stress (60 MPa) bond strengths were overcome and fracturing occurred on a large scale. This type of deformation (brittle

Figure 10.1. Breaking and recombination of bonds with new neighbours due to migration of a dislocation in a crystal responding to stress. (After Bloss, 1971).



failure) would be expected during the compression experiment. Lower strain rates at elevated temperatures and higher confining pressure are needed for plastic deformation to occur in crystals. However, in real faults where higher ambient temperatures occur due to depth of burial and strain rates persist for longer periods of time, plastic deformation of quartz therefore must be considered in the discussion of zeroing mechanisms.

Elastic deformation of quartz results in bonds being stretched but not broken. Trapped charges migrate to opposite ends of the C-axis in quartz resulting in a strong piezoelectric buildup. When strain is discontinued trapped charges migrate back to their original orientation and the piezoelectric effect subsides. Therefore the charges would not be expected to escape the traps and the AD's should not decrease significantly. Therefore elastic deformation fails to explain the results of the 29 MPa compression experiment. It is doubtful that the 29 MPa compression pressure was sufficient to induce the quartz to deform plastically at room temperature (plastic deformation would result at higher temperatures and prolonged strain conditions such as would be found on real fault surfaces). It is therefore probable that limited fracturing of grains did occur during the 29 MPa compression experiment but the sieving technique was not of

sufficient sensitivity to pick up these subtle changes in grain size distribution.

Both the non-elastic fracturing and plastic deformation methods involve permanent breaking of bonds through dislocations. When a bond dislocation or fracture occurs where a trapped hole or electron is being held, the traps are destroyed and the paramagnetic center is deleted. Again the subsequent formation of new bonds may lead to the creation of new, empty traps.

Higher strain meant more pronounced deformation resulting in brittle fracturing which is expected in grains exposed to higher stress where grain contacts increase in number and size until brittle failure eventually occurs (Figure 8.3b). Therefore there is the potential for more dislocations to sweep through the crystal undergoing a higher strain and to reset a larger proportion of paramagnetic centers.

Partial or total resetting should also occur due to pervasive cataclasis during stable sliding. When strike-slip motion occurs along the wall rock-gouge interface, new gouge will be created, which should also be zeroed by cataclastic breakage of asperities on the surface.

10.3 The Preferential Zeroing of Centers

The experimental data suggest a preference of extending and breaking bonds where OH center trapped holes are held compared with the Al hole centers. This effect is due to the siting of the OH centers in comparison to the Al center. In the vicinity of dislocations, two oxygen atoms that are normally separated from one another (by an Si ion) can be brought into close proximity to form a weakly bonded OH trap. The Al center is located at a bridging oxygen that is comparatively strongly bonded between a Si and Al ion. At the onset of deformation there would be a tendency for bond stretching and movement to occur along preexisting dislocations initially (the necessary strain is normally only reached at preexisting imperfections), and bonds near the dislocation would be preferentially extended and broken. An OH center would therefore be more sensitive than the Al center to detrapping of holes during deformation and more detrapping for the OH center would be observed.

The Ge and Ti centers were not affected significantly during mechanical deformation. This may be due to the trapped electrons for both of these centers being located principally on the central cation, where they would not be affected by bond extensions and breakages through fracturing and dislocations. The Ti center intensity does decrease slightly

after deformation indicating that some detrapping of electrons has occurred during deformation. The Ge center actually trapped more electrons as deformation increased. This may result from re-trapping of electrons and interstitial ions liberated from dislocations near Ge substituted tetrahedral sites.

As discussed above, the E_1' center occurs as a result of an oxygen vacancy. Although the behaviour of this center during deformation was not investigated it is assumed that a dislocation sweeping past an E_1' center would most likely delete the trap thereby lowering the ESR intensity. The E_1' center could thus be useful for dating fault movement. However, when the weak bond between the two Si ions is broken there would be a higher chance of new bonds being set up between the Si ions and O^{2-} ligands since the ratio of central cations to ligands is 1:4. Therefore in samples that are highly deformed through fault activity the concentration of E_1' centers may be negligible and thus an E_1' ESR signal is not detectible. This is the case for some of the samples of fault gouge used for this study.

10.4 Bleaching

Only the Ge center was affected by exposure to light. Complete bleaching takes place within 6.5 hours when a thin layer of sample (few grains thick) is exposed to UV light, within 10 hours for direct sunlight and within 20 hours for diffuse sunlight. It is most likely that energy is transferred from a photon of light to the electron, providing the exact activation energy needed for the electron to escape the trap. UV light seems to have the optimal photon frequency with the necessary activation energy to pop out electrons held by a Ge center. Most of the high intensity UV light from the sun is filtered out by the atmosphere and during cloudy conditions a portion of the UV light allowed through by the atmosphere is filtered out further. Thus, zeroing takes slightly longer for cloudy conditions than for clear skies. This raises the possibility of ESR dating on certain light zeroed sediments in which the Ge center in the top layer of the sediment would be zeroed within the first two days of deposition. The Ge center in quartz held in a standard quartz sample tube showed a slow but steady decrease in intensity when exposed to UV light as a result of zeroing of the Ge signals in the grains on the outside of the tube. This shows that even with the highest intensity light, only the top layer is significantly affected and therefore the time since deposition and sufficient burial (when the Ge signal starts to acquire charge) is short. It may

also be expected that the Ge signal will fade on exposure to light during sampling and laboratory preparation and therefore care must be taken when preparing the sample to ensure that no part of the signal is depleted by exposure to light.

10.5 The Plateau Criterion for Estimating Total Zeroing

Based on our experimental studies, the proposed plateau criterion for the determination of total resetting of a sample of fault gouge seems to be justified. Therefore in a sample that has been exposed to sufficiently intense stress, complete resetting of a paramagnetic center should lead to the establishment of a plateau of equal AD/Age values for particles smaller than a particular size (r_c). For centers with lesser stress sensitivities, where no plateau is observed, the smallest grain sizes should at least converge onto the age plateau for the most sensitive OH-center (there may not be a convergence onto the OH AD plateau for the other centers if there is a variation of the α -efficiencies for the different centers). Grain sizes that give AD values larger than the OH plateau are assumed to be non-zeroed and therefore should not be used for determining an age.

10.6 Age Calculations

As discussed earlier, determination of DR is complicated through uncertainty regarding disequilibrium of radioactive species in a fault system. These uncertainties were not incorporated into determinations of DR for the gouge samples, but rather incorporated in the error calculations.

It is suggested that in the future, $^{234}\text{U}/^{238}\text{U}$ and $^{230}\text{Th}/^{234}\text{U}$ activity ratios be measured to assess the true U-series dose rates. If this is not possible then approximately 10% ^{234}U leaching should be assumed. For radon it is much more difficult to estimate relative abundance in a fault zone. Therefore, 0% ^{222}Rn loss was assumed for the age calculations, but the effect of 50% loss was used in the error calculation.

Chapter 11: CONCLUSIONS

It is unlikely that sufficiently high temperatures for total zeroing of ESR signals in quartz are generated on a fault surface during fault activity. The main zeroing process is therefore accomplished through mechanical deformation of individual grains in the fault gouge. Experimental results confirmed that smaller grains are affected more by stress than larger grains, and that centers with electrons or holes trapped at sites that are easily affected by dislocations are preferentially reset (the OH center being the most sensitive). Therefore, intense stress should lead to the establishment of a plateau of equal AD/age for grains smaller than a particular size. This would indicate total resetting of the center. If no plateau is observed, resetting may be indicated by converging AD's for centers with different stress sensitivities. Grain sizes that give AD values larger than the plateau are assumed to have been incompletely zeroed and therefore should not be used for determining an age. For the samples used for this study the OH-center shows the plateau development, most clearly, as would be expected from experimental compression tests that show it to be the center most easily reset.

The highest probability of complete zeroing is encountered close to a major sliding surface such as the boundary between gouge and unbroken rock. There may be samples

that have only been partially reset due to an inhomogeneous stress field distributed throughout the gouge. While samples collected at the present-day erosional surface may display a plateau, there is no guarantee that the age given by this plateau corresponds to the latest fault movement. Core-drilling to some moderate depth (100m) in the fault zone may be necessary to obtain samples that were more recently reset.

For further investigation it is suggested that ages for material collected at the present day erosional surface cutting a fault known to have moved in recent times, be compared with ages obtained for material collected from core drilling through the fault zone at depths greater than 50m.

References

- Abragam, A. and Bleaney, B. (1986). Electron paramagnetic resonance of transition ions. 911 p., Dover, New York.
- Aitken, M.J.(1985). Thermoluminescence dating. 359 p., Academic Press, London.
- Anderson, E.M. (1942). The dynamics of faulting and dyke formation, with applications to Britain. 191p., Oliver and Boyd, Edinburgh.
- Anderson, J.H. and Weil, J.A. (1959). Paramagnetic resonance absorption of colour centers in germanium-doped quartz. *Journal of Chemical Physics*, 31, 427-434.
- Apers, D., Debuyst, R., DeCanniere, P., Dejehet, F. and Lombard, E.(1981). A criticism of the dating by electron paramagnetic resonance (ESR) of the stalagmitic floors of the Caune de l'Arago at Tautavel. *In: DeLumley, H. and Labeyrie, J. (eds): Absolute dating and isotope analysis in prehistory - methods and limits, Proceedings Pretirage*, pp. 533-550.
- Ariyama, T.(1985). Conditions of resetting the ESR clock during faulting. *In: Ikeya, M. and Miki, T. (eds): ESR Dating and Dosimetry*, pp. 249-256.
- Aydin, A. (1978). Small faults as deformation bands in sandstone. *Pure and Applied Geophysics*, 116, 913-929.
- Aydin, A. and Johnson, A.M. (1978). Development of faults as zones of deformation bands and as slip surfaces in sandstone. *Pure and Applied Geophysics*, 116, 931-942.
- Bar, M., Kolodny, Y. and Bentor, U.K. (1974). Dating of faults by fission track dating of epidotes-An attempt. *Earth and Planetary Science Letters*, 22, 157-166.
- Bell, W.T.(1980). Alpha dose attenuation in quartz grains for thermoluminescence dating. *Ancient TL*, 12, 4-8.
- Bell, W.T. and Zimmerman, D.W. (1978). The effect of HF etching on the morphology of quartz inclusions for thermoluminescence dating. *Archaeometry*, 20, no.1, 63.

- Bershov, L.V., Marfunin, A.S., and Speranskiy, A.V. (1978). A new stable radiation center in quartz. *International Geology Review*, 22, no.10, 1225-1233.
- Bloss, F.D. (1971). Crystallography and Crystal Chemistry: An Introduction. 545 p. Holt, Rinehart, and Winston, Inc.
- Bowman, S.G.E. (1976). Thermoluminescence dating: the evaluation of radiation dosage.- Unpublished PhD Thesis, University of Oxford, Oxford.
- Brace, W.F. and Byerlee, J.D. (1966). Stick-slip as a mechanism for earthquakes. *Science*, 153, 990-992.
- Brune, J.N., Henyey, T.L., and Roy, R.F. (1969). Heat flow, stress, and rate of slip along the San Andreas Fault, California. *Journal of Geophysical Research*, 74, no.15, 3821-3827.
- Byerlee, J. and Summers, R. (1976). A note on the effect of fault gouge thickness on fault stability. *International Journal of Rock Mechanics Mineralogical Sciences and Geomechanical Abstracts*, 13, 35-36.
- Cohen, A.J. and Smith, H.L. (1958). Anisotropic colour centers in alpha quartz, 2, Germanium-doped synthetic quartz. *Journal of Chemical Physics*, 28, 401-405.
- Colman, S.M. (1987). Dating Quaternary deposits using weathering rinds and related features. Unpublished workshop proceedings, Directions in paleoseismology, Quaternary dating techniques, US Geological Survey Albuquerque NM, 28-30.
- Damon, P.E. (1987). Radiocarbon dating techniques: Tams and Quantulus, Unpublished workshop proceedings, Directions in paleoseismology, Quaternary dating techniques, USGS, Al, NM, 6-7.
- Eberhart, M.E., Johnson, K.H., Messmer, R.P. and Briant, C.L. (1983). Molecular Orbitals and the Atomistics of Fracture. 1074p. Atomistics of Fracture Plenum Press, New York.
- Engelder J.T. (1974). Cataclasis and the generation of fault gouge. *Geological Society of America Bulletin*, 85, 1515-1522.
- Engelder, T. (1978). Aspects of asperity-surface interaction and surface damage of rocks during experimental frictional sliding. *Pure and Applied Geophysics*, 116, 705-716.

- Feigl, F.J. and Anderson, J.H. (1970). Defects in crystalline quartz: electron paramagnetic resonance of E' vacancy centers associated with germanium impurities. *Journal of the Physics and Chemistry of Solids*, 31, 575-596.
- Feigl, F.J., Fowler, W.B., and Yip, K.L. (1974). Oxygen vacancy model for the E' center in SiO₂. *Solid State Communications*, 14, 225.
- Fleming, S.J. (1970). Thermoluminescent dating: refinement of the quartz inclusion method. *Archaeometry*, 12, 135.
- Forman, S.L. (1987). The application of TL dating to paleoseismology, Unpublished workshop proceedings, Directions in paleoseismology, Quaternary dating techniques, USGS, Al, NM, 20-23.
- Friedman, M., Logan, J.M., and Rigert, J.A. (1974). Glass indurated quartz gouge in sliding friction experiments on sandstone. *Geological Society of America Bulletin*, 85, 937-942.
- Fukuchi, T., Imai, N. & Shimokawa, K. (1985). Dating of the fault movement by various ESR signals in quartz - Cases on the faults in the South Fossa Magna, Japan. In: Ikeya, M. & Miki, T. (eds), ESR Dating and Dosimetry, Ionics Press, Tokyo, 211-217.
- Fukuchi, T., Imai, N., and Shimokawa, K. (1986). ESR dating of fault movement using various defect centres in quartz; the case in the western South Fossa Magna, Japan. *Earth and Planetary Science Letters*, 78, 121-128.
- Griscom, D.L. (1978). Defects and impurities in alpha-quartz and fused silica. In: Pantelides, S.T. (ed): Proceedings of the International Topical Conference, Yorktown Heights, New York. Pergamon Press, 232-252.
- Grün, R. (1985). ESR-dating speleothem records: Limits of the method In: Ikeya, M. and Miki, T. (eds): ESR dating and Dosimetry, Ionics Press, Tokyo, 61-72.
- Grün, R. (1987). Electron spin resonance (ESR) dating. In: Rutter, N. and Brigham-Grette, J. (eds): Applied Aspects of Quaternary Geochronology (in press).
- Grün, R., Schwarcz, H.P., and Zymela, S. (1987). ESR dating of tooth enamel, *Canadian Journal of Earth Sciences*, 24, 1022-1037.

- Hennig, G.J. and Grün, R.(1983). ESR dating in Quaternary Geology. *Quaternary Science Reviews*, 2, 157-238.
- Hennig, G.J., Herr, W. and Weber, E.(1981). Electron spin resonance (ESR) dating on speleothems (notes on problems and progress). In: DeLumley, H. and Labeyrie, J. (eds): Absolute dating and isotope analysis in prehistory-methods and limits, Proceedings Pretirage, CNRS Paris.
- Ikeya, M.(1975). Dating a stalactite by electron paramagnetic resonance. *Nature*, 255, 48-50.
- Ikeya, M. (1977). Electron spin resonance dating and fission track detection of Petralona stalagmite. *Anthropos*, 4, 152-166.
- Ikeya, M. (1978). Electron spin resonance as a method of dating. *Archaeometry*, 20, 147-158.
- Ikeya, M. (1985). Electron Spin Resonance. In: Rutter, N.W. (ed): Dating Methods of Pleistocene Deposits and Their Problems, Geoscience Canada Reprint Series 2, 73-87.
- Ikeya, M., Miki, T., Tanaka, K. (1982). Dating of a fault by Electron Spin Resonance on intrafault materials, *Science*, 215, 1392-1393.
- Ikeya, M., Miki, T., Tanaka, K., Sakuramoto, Y. and Ohmura, K.(1983). ESR dating of faults at Rokko and Atotsugawa. *PACT* 9, 411-419.
- Ikeya, M. and Ohmura, K. (1981). Dating of fossil shells with electron spin resonance, *Journal of Geology*, 89, 247-251.
- Imai, N. & Shimokawa, K.(1985). Dating of volcanic ash by electron spin resonance using aluminum and titanium centers in plagioclase. In: Ikeya, M. and Miki, T. (eds): ESR Dating and Dosimetry, Ionics Press, Tokyo, 187-190.
- Imai, N. Shimokawa, K. and Hirota, M. (1985). ESR dating of volcanic ash, *Nature*, 314, 81-83.
- Isoya, J. and Weil, J.A. (1979). Uncompensated titanium (3^+) center in alpha-quartz. *Physical Status Solidi A*, 52, K193.
- Isoya, J., Weil, J.A. and Halliburton, L.E. (1981). EPR and ab initio SCFMO studies of the Si-H-Si system in the E_4' center of alpha quartz. *Journal of Chemical Physics*, 69, 4876-4884.

- Ito, T. & Sawada, S. (1985). Reliable criteria for the selection of sampling points for ESR fault dating. In: Ikeya, M. & Miki, T. (eds), ESR Dating and Dosimetry, Ionics Press, Tokyo, 229-237.
- Ivanovich, M., Vita-Finzi, C., and Hennig, G.J. (1983). Uranium-series dating of molluscs from uplifted Holocene beaches in the Persian Gulf. *Nature*, 302, 408-410.
- Jackson, R.E. and Dunn, D.E. (1974). Experimental sliding friction and cataclasis of foliated rocks. *International Journal of Rock Mechanics Mineralogical Sciences and Geomechanical Abstracts*, 11, 235-249.
- Jacoby, G.C. (1987). Application of dendrochronology to paleoseismology. Unpublished workshop proceedings, *Directions in paleoseismology, Quaternary dating techniques*, USGS Al. NM, 1-5.
- Kanaori, Y., Miyakoshi, K., Kakuta, T., and Satake, Y. (1980). Dating fault activity by surface textures of quartz grains from fault gouges. *Engineering Geology*, 16, 243-262.
- Kanaori, Y., Tanaka, K. and Miyakoshi, K. (1985). Further studies on the use of quartz grains from fault gouges to establish the age of faulting, *Engineering Geology*, 21, 175-194.
- Katzenberger, O. and Grün, R. (1985). ESR dating of circumarctic molluscs. *Nuclear Tracks*, 10, 885-890.
- Katzenberger, O., and Willems, N. (1987). Inferences encountered in the determination of AD of mollusc samples, Presentation held at: Fifth Specialist Seminar on TL and ESR dating, July 5-10 1987, Cambridge (abstract No. 98).
- Kerr, R.A. (1987). Is the San Andreas weak at heart? *Science*, 236, 388-389.
- Kosaka, K. & Sawada, S. (1985). Fault gouge analysis and ESR dating of the Tsurukawa fault, west of Tokyo: significance of minute sampling. In: Ikeya, M. & Miki, T. (eds), ESR Dating and Dosimetry, Ionics Press, Tokyo, 257-266.
- Kralik, M., Klima, K., and Riedmüller, G. (1987). Dating fault gouges. *Nature*, 327, 315-317.

- Ku, T.L. (1976). The uranium-series methods of age determination. Annual Review of Earth and Planetary Sciences, 4, 347-379.
- Linke, G., Katzenberger, O. and Grün, R. (1985). Description and ESR dating of the Holstein interglaciation. Quaternary Science Reviews 4, 319-331.
- Longstaffe, F.J. (1986). Oxygen isotope studies of diagenesis in the Basal Belly River Sandstone, Pembina I-Pool, Alberta. Journal of Sedimentary Petrology, 56, no.1, 78-88.
- Lyons, J.B. and Snellenburg, J. (1974). K-Ar dating of illite from intrafault material. Geological Society of America Bulletin, 85, 94-106.
- MacKey, J.H. (1963). EPR of impurity-related colour centers in Ge-doped quartz. Journal of Chemical Physics, 39, 74-83.
- Marfunin, A.S. (1979). Spectroscopy Luminescence and Radiation Centers in Minerals. 352p. Springer-Verlag, Berlin.
- McMorris, D.W. (1971). Impurity color centers in quartz and trapped electron dating: Electron spin resonance, thermoluminescence studies. Journal of Geophysical Research, 76, 7875-7887.
- Mejdahl, V. (1979). Thermoluminescence dating: beta-dose attenuation in quartz grains. Archaeometry, 21, 61-72.
- Mejdahl, V. (1987). Internal radioactivity in quartz and feldspar grains. Ancient TL, 5, no.2, 10-17.
- Miki, T. & Ikeya, M. (1982). Physical basis of fault dating with ESR. Naturwissenschaften, 69, 90-91.
- Moiseyev, B.M. and Rakov, L.T. (1976). Paleodosimetric properties of the E_1' centers in quartz. Doklady Akademii Nauk. SSSR, 233, no.4, 679-682.
- Nambi, K.S.V. (1985). Scope of ESR studies in thermally stimulated luminescence studies and chronological applications. Nuclear Tracks, 10, 113-131.
- Nambi, K.S.V. and Aitken, M.J. (1986). Annual dose conversion factors for TL and ESR dating. Archaeometry 28, 202-205.
- O'Brien, M.C.M. (1955). The structure of the colour centers in smoky quartz. Proceedings of the Royal Society of London, Series A, 231, 404-414.

- Prescott, J.R. and Stephan, L.G. (1982). The contribution of cosmic radiation to the environmental dose for thermoluminescence dating - latitude, altitude and depth dependencies. PACT, 6, 17-25.
- Radtke, U. (1987). Marine terraces in Chile (22°-32°S)-geomorphology, chronostratigraphy and neotectonics. The Quaternary of South America and Antarctica Peninsula, Quaternary Research, in press.
- Radtke, U., Grün, R. and Schwarcz, H.P. (1987). New results from ESR dating of Pleistocene coral reef tracts of Barbados (W.I.). Quaternary Research, in press.
- Radtke, U. and Grün, R. (1987). ESR dating of corals. Quaternary Science Reviews, (in press).
- Rakov, L.T., Milovidova, N.D., Kuvshinova, K.A. and Moiseyev, B.M. (1986). An ESR study of Ge centers in natural polycrystalline quartz. Geokhimiya, 9, 1339-1344. Translated in Geochemistry International (1986), 23, 3, 61-66.
- Raleigh, C.B., Sieh, K., Sykes, L.R. and Anderson, D.L. (1982). Forecasting southern California earthquakes. Science, 217, 1097-1104.
- Reeves, M.J. (1985). Rock surface roughness and frictional strength. International Journal of Rock Mechanics Mineralogical Sciences and Geomechanical Abstracts, 22, no.6 429-442.
- Regulla, D.F., Wiesner, A. and Göksu, H.Y. (1985). Effects of sample preparation on the ESR spectra of calcite, bone and volcanic material. Nuclear Tracks, 10, 825-830.
- Rinneberg, H. and Weil, J.A. (1972). EPR studies of $Ti^{3+} - H^{+}$ centers in X-irradiated α -quartz. Journal of Chemical Physics, 56, 2019-2023.
- Schnadt, R. and Räuber, A. (1971). Motional effects in the trapped-hole center in smoky quartz. Solid State Communications, 9, 159-161.
- Scholz, C., Molnar, P., and Johnson, T. (1972). Detailed studies of frictional sliding of granite and implications for the earthquake mechanism. Journal of Geophysical Research, 77, no.22, 6392-6406.

- Shimokawa, K. and Imai, N. (1987). Simultaneous determination of alteration and eruption ages of volcanic rocks by electron spin resonance. *Geochimica et Cosmochimica Acta*, 51, no.1, 115-119.
- Shimokawa, K., Imai, N. & Hirota, M. (1984). Dating of volcanic rock by electron spin resonance. *Isotope Geoscience*, 2, 365-373.
- Shimamoto, T. and Logan, J.M. (1981). Effects of simulated fault gouge on the sliding behaviour of Tennessee Sandstone: Non clay gouges. *Journal of Geophysical Research*, 86, B4, 2902-2914.
- Slosson, J.E. and Gray, C.H. (1984). Geology and man; San Bernardino-Cajon Pass region. *In*: Hester, R.L. and Hallinger, D.E. (eds): *San Andreas Fault - Cajon Pass to Wrightwood*, 97-120.
- Suppe, J. (1985). Principles of structural geology. 537p. Prentice-Hall Inc.
- Tanaka, T., Sawada, S. and Ito, T. (1985). ESR dating of late Pleistocene near-shore and terrace sands in southern Kanto, Japan. *In*: Ikeya, M. and Miki, T. (eds): ESR Dating and Dosimetry, Ionics Press, Tokyo, 275-280.
- Tanaka, K. & Shidahara, T. (1985). Fracturing, crushing and grinding effects on ESR signal of quartz. *In*: Ikeya, M. & Miki, T. (eds), ESR Dating and Dosimetry, Ionics Press, Tokyo, 239-247.
- Taylor, A.L. and Farnell, G.W. (1964). Spin-lattice interaction experiments on colour centers in quartz. *Canadian Journal of Physics*, 42, 595-607.
- Teufel, L.W. and Logan, J.M. (1978). Effect of displacement rate on the real area of contact and the temperatures generated during frictional sliding of Tennessee Sandstone. *Pure and Applied Geophysics*, 116, 840-865.
- Toyokura, I., Sakuramoto, Y., Ohmura, K., Iwasaki, E. & Ishiguchi, M. (1985). Determination of the age of fault movement - the Rokko fault. *In*: Ikeya, M. & Miki, T. (eds), ESR Dating and Dosimetry, Ionics Press, Tokyo, 219-228.
- Verosub, K.L. (1987). The application of paleomagnetism to the dating of Quaternary materials. Unpublished workshop proceedings, *Directions in paleoseismology, Quaternary dating techniques*, USGS, Al, NM, 48-50.

- Weeks, R.A. and Nelson, C.M. (1960). Trapped electrons in irradiated quartz and silica: 11, *Electron Spin Resonance. Journal of the American Ceramic Society*, 43, no.8, 399-404.
- Weil, J.A. (1971). Germanium-hydrogen-lithium center in alpha-quartz. *Journal of Chemical Physics*, 55, 4685-4698.
- Weil, J.A. (1984). A review of Electron Spin Spectroscopy and its application to the study of paramagnetic defects in crystalline quartz. *Physics and Chemistry of Minerals*, 10, 149-165.
- Yip, K.L. and Fowler, W.B. (1975). Electronic structures of E_1' centers in SiO_2 . *Physics Reviews B*, 11, 2327-2338.
- Yokoyama, Y., Falgueres, C. and Quaegebeur, J.P. (1985). ESR dating of quartz from Quaternary sediments first attempt. *Nuclear Tracks*, 10, 921-928.
- Yokoyama, Y., Nguyen, H.V., Quaegebeur, J.P. and Poupeau, G. (1982). Some problems encountered in the evaluation of annual dose rates in electron spin resonance dating of fossil bones. *PACT*, 6, 103-115.
- Zeller, E.J., Levy, P.W. and Mattern, P.L. (1967). Geologic dating by electron spin resonance. Symposium on Radioactive Dating and Low Level Counting (I.A.E.A., Wien) Proceedings, 531-540.
- Zhuo-ran, L., Mei-er, Y., Qi-chen, F., & Ikeya, M. (1985). ESR dating of the age of the fault movement at San-Jiang fault zone in West China. In: Ikeya, M. & Miki, T. (eds), ESR Dating and Dosimetry, Ionics Press, Tokyo, 205-210.
- Zymela, S. (1986). ESR dating of Pleistocene deposits. 118p., unpublished MSc-Thesis, McMaster University, Hamilton.
- Zymela, S., Schwarcz, H.P., Grün, R., Stalker, A.M., and Churcher, C.S. (1987). ESR dating of Pleistocene fossil teeth from Alberta and Saskatchewan, *Canadian Journal of Earth Sciences*, 24, in press.

Appendix A

A.1 The Physical Basis of ESR Spectroscopy

According to quantum mechanics, an electron defines a density cloud around a nucleus where the electron has a high probability of being found, depending on the shell and sub-orbital it occupies. Even though the uncertainty principle forbids the isolation of an electron as a particle entity, it is easiest to perceive the ESR principle if the electron is imagined as is a point charge that orbits the nucleus and spins within the orbit.

A charged electron moving in an orbit is equivalent to a circular electric current which in turn generates a magnetic dipole moment. The electron also has a spin magnetic moment associated with it generated by the charged electron rotating in the magnetic field provided by the orbiting motion of the electron. The magnetic moment is expressed by:

$$\mu_S = -g \frac{\mu_B}{h/2\pi} \vec{s} \quad (3)$$

where μ_B = Bohr magneton ($9.27314 \cdot 10^{-21}$ erg Gauss $^{-1}$)

μ_S = magnetic moment

g = Landé factor (g value = 2.0023 for a free electron)

h = Planck's constant ($6.62554 \cdot 10^{-27}$ erg sec $^{-1}$)

\vec{s} = spin quantum number

When placed in an external magnetic field H (in z direction) an electron can only have two orientations (s_z) with respect to the field; parallel or antiparallel which is referred to as "spin up" and "spin down" respectively. This defines the magnetic quantum number of spin (M_S) with its two possible values $M_S = \pm 1/2$ (Figure A1).

It follows that:

$$s_z = M_S h/2\pi = \pm 1/2 h/2\pi \quad (4)$$

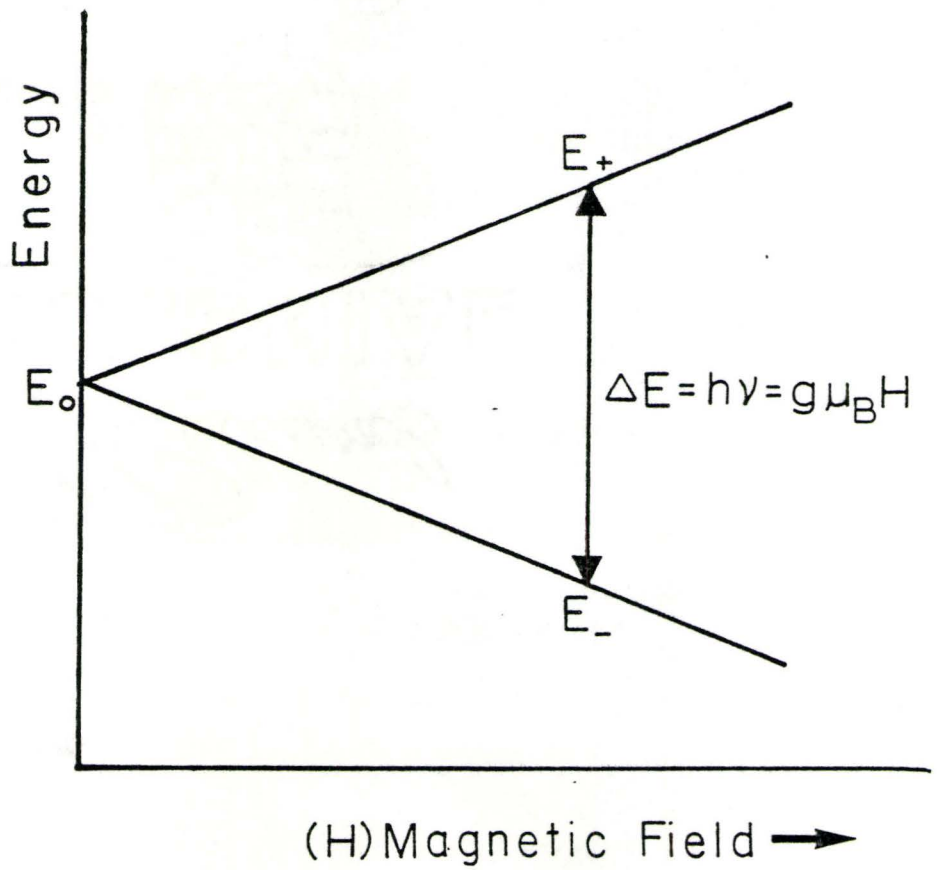
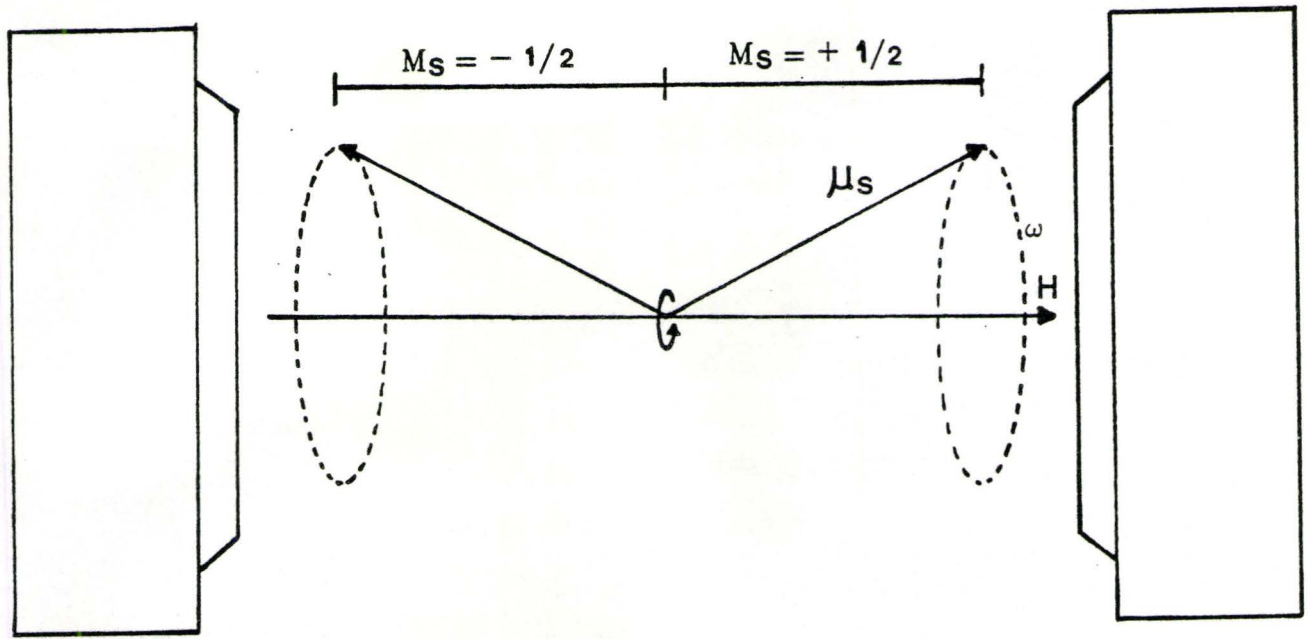
The magnetic moment of the spin can be expressed in terms of the orientation of its components in the external magnetic field:

$$\mu_z = \frac{g \mu_B}{h/2\pi} (\pm 1/2 h/2\pi) = \pm 1/2 g \mu_B \quad (5)$$

These two possible states of an electron in an external magnetic field are energetically different and therefore a splitting of the initial energy level E_0 into two discrete energy levels E_+ and E_- occurs. This is known as the Zeeman effect (Figure A2). The energy of the electron spin state in an external magnetic field is a function of the magnetic field strength (H). ΔE is the energy needed to transfer from the lower E_- to the higher E_+ energy level: $\Delta E = E_+ - E_-$ which is:

Figure A1. Two possible orientations of an electron in an external magnetic field.

Figure A2. Zeeman splitting into two energy levels E_+ and E_- .



$$\Delta E = g \mu_B H \quad (6)$$

where H is the external magnetic field strength (Gauss).

Electrons can be transferred from the lower energy level to the higher energy level by an external energy source, e.g., electromagnetic microwave radiation. Electromagnetic radiation transfers energy to the electron by a virtual particle with a discrete quantum of energy, $h\nu$ (ν = radiation frequency). If the following condition is met (7), resonance of the electron will occur: absorbing energy when going from the lower to higher energy state, and emitting energy of the same magnitude when transferring from the higher to lower state.

$$h\nu = g \mu_B H \quad (7)$$

Thus absorption of the microwaves is detected when $H = h\nu/g\mu_B$.

The ratio between electron populations in the two Zeeman energy levels as given by the Boltzmann distribution:

$$\frac{N_-}{N_+} = e^{\frac{E_+ - E_-}{k T}} = e^{\frac{h \nu}{k T}} = e^{(0.048 \nu^*/T)} \quad (8)$$

k = Boltzmann's constant ($1.385 \cdot 10^{-16}$ erg K^{-1})

T = temperature (K)

ν^* = frequency in GHz ($= 10^9$ sec $^{-1}$)

As can be deduced from equation (8), the ratio between the electron populations in the two Zeeman-levels (N_-/N_+) depends on the temperature of the system and the applied microwave frequency. In principle, after an initial absorption of microwave energy the two electron populations would equalize. Then, no further absorption would occur and, therefore, no ESR spectra could be observed. The fact that continuous electron transfer from lower to higher energy levels can be observed when electromagnetic radiation is applied can be explained by "spin-lattice-relaxation". When an electron transfers from higher to lower energy levels the energy is not released as microwave energy but rather transferred to the crystal lattice by phonons (Raman-process). The transfer is delayed with a characteristic "spin-relaxation-time". This is the time required to bring the radiation induced disturbance of the Boltzmann distribution to $1/e = 37\%$ of its original magnitude. If the spin-relaxation-time is short enough to ensure thermal equilibrium for the lattice then the absorbed energy is proportional to the applied microwave energy. After maximum energy transfer to the lattice is reached, additional microwave power tends to equalize the two electron populations which makes measurement of the ESR spectrum difficult.

Long spin-relaxation-times are to be expected when the g -value is close to the free spin value (2.0023), and short spin relaxation times when the g -value deviates from this value (Abragam and Bleaney, 1986). The degree of saturation is dependent on the length of the spin-relaxation-times. The relaxation times increase at lower temperatures and therefore some ESR spectra cannot be resolved at these lower temperatures (see Marfunin, 1979; and Abragam and Bleaney, 1986 for further discussion).